國 立 交 通 大 學

光電工程研究所

博 士 論 文

三五族半導體發光元件結構優化之研究

Study of Structure Optimization in III-V Semiconductor Light Emitting Devices

研 究 生: 張詒安　　Student: Yi-An Chang

指導教授: 郭浩中 教授　　Advisor: Dr. Hao-Chung Kuo

王興宗 教授　　Dr. Shing-Chung Wang

中 華 民 國 九 十 六 年 九 月

三五族半導體發光元件結構優化之研究

Study of Structure Optimization in III-V Semiconductor Light Emitting Devices

研 究 生：張詒安　　Student：Yi-An Chang

指導教授：郭浩中教授　　Advisor： Dr. Hao-Chung Kuo

王興宗教授　　Dr. Shing-Chung Wang

國 立 交 通 大 學　電機資訊學院

光電工程研究所

博 士 論 文

A dissertation

Submitted to Institute of Electro-Optical Engineering

College of Electrical Engineering and Computer Science

National Chiao Tung University

in partial Fulfillment of the Requirements

for the Degree of

Doctor of Philosophy

in

Electro-Optical Engineering

September 2007

Hsinchu, Taiwan, Republic of China

中華民國九十六年九月

三五族半導體發光元件結構優化之研究

研究生：張詒安　　指導教授：郭浩中教授

王興宗教授

國立交通大學光電工程研究所

摘要

本論文旨在探討三五族光電半導體元件包含紫外線發光二極體(ultraviolet light-emitting diode, LED)、紅光共振腔發光二極體(resonant-cavity LED)、850-nm面射型雷射(vertical-cavity surface-emitting laser)以及1.3-μm側射型雷射(edge-emitting laser)之操作性能改良相關研究。對於半導體發光元件而言要使其具有高輸出功率以及高穩定性的輸出性能，元件磊晶晶體品質(epitaxial crystal quality)以及元件磊晶結構設計上實屬於相當重要一環；其中要使發光元件能穩定地操作在高溫高輸入電流的情況下，磊晶結構的設計更扮演極重要的角色。本論文即以有機金屬液相沉積法(metalorganic chemical vapor deposition, MOCVD)成長以上四種元件，配合理論模擬方式進行結構設計上的改良來使電子能有效地被侷限於活性層量子井 (active region quantum well)裡，達到降低電子溢流(electron leakage)提升元件輸出性能的目的。

在紫外線發光二極體研究上，我們以四元氮化鋁鎵銦(AlGaInN)為活性層材料並製做出最大輸出功率達4 mW，外部量子效率(external quantum efficiency)為1.2%，波長為370 nm的發光二極體。而為使此一元件具有較高之輸出功率以及穩定的高溫高輸入電流特性，我們以理論模擬方式進行元件結構的改良設計，探討氮化鋁鎵銦量子井個數以及氮化鋁鎵電子阻礙層對元件輸出特性的影響。模擬結果顯示當氮化鋁鎵銦量子井個數為五至七個和氮化鋁鎵電子阻礙層中鋁組成為19%時，可以達到降低電子溢流作用並提供較佳之輸出特性。

在紅光共振腔發光二極體研究上，由於元件活性層量子井材料磷化鋁鎵銦

(AlGaInP)的導電帶能帶間隙值只有約300 meV，當電子注入量子井中很容易產生電子溢流現象進而降低元件於高溫操作下的輸出性能。藉由將傳統共振腔發光二極體共振腔長為一個波長增加為三個波長，我們發現在溫度範圍25–95ºC變化下，傳統結構在注入電流固定為20 mA的輸出功率變化為-2.1 dB，而共振腔長為三個波長的共振腔發光二極體卻只有-0.6 dB，且其遠場圖(far field pattern)隨注入電流變化相當穩定，適合做為塑膠光纖傳輸的光主動元件。理論模擬結果也證明，增加共振腔長至三個波長亦即增加量子井個數至三倍，確實有助於降低電子溢流達到侷限電子、穩定元件高溫、高電流特性的目的。

在850-nm面射型雷射研究上，首先針對具有不同壓縮應力之量子井結構進行理論分析，發現以具有較高壓縮應力值的砷化鋁鎵銦(AlGaInAs)做為量子井比起砷化銦鎵(InGaAs)可以具有較高之材料增益(material gain) ，較低透明載子密度(transparency carrier concentration)與透明自發輻射電流密度(transparency radiative current density)。接著我們選擇以$Al_{0.08}Ga_{0.77}In_{0.15}As$做為量子井實際成長並做成元件，我們得到在室溫操作下的850-nm面射型雷射，其臨界電流為1.47 mA，電光轉換效率(slope efficiency)為0.37 mW/mA，且隨操作溫度升高至95 ºC，臨界電流值增加至2.17 mA，電光轉換效率降為0.25 mW/mA。爲進一步改善雷射輸出性能，我們首次於活性層量子井中加入一電子阻礙層，發現於室溫操做的850-nm面射型雷射臨界電流降低至1.33 mA，電光轉換效率也達到0.53 mW/mA，且當溫度升高至95 ºC時臨界電流值只增加0.27 mA，電光轉換效率也仍有0.4 mW/mA的表現。同時我們也以數值模擬方式證明加入電子阻礙層確實可以有效阻擋電子溢流進而提升雷射輸出性能。

在1.3-μm InGaAsN/GaAsN側射型雷射研究上，由於實際成長氮砷化銦鎵磊晶結構時，於砷化鎵位障層(barrier)裡加入氮可以平衡InGaAsN量子井裡的高壓縮應力(compressive strain)並有助於避免量子井中氮原子的流失(out-diffusion)，然而卻會因導電帶能帶間隙值降低而產生電子溢流現象。因此首先針對氮砷化銦鎵($In_{0.4}Ga_{0.6}As_{0.986}N_{0.014}$)單量子井旁的氮砷化鎵位障層進行理論模擬分析，探討氮砷化鎵位障層中氮的成分對元件輸出性能的影響，我們提出以$GaAs_{0.995}N_{0.005}$做為位障層，不

僅可以符合實際磊晶考量，更可防止電子溢流現象發生。經由實際磊晶成長及製程大小為4×1000 μm^2的雷射元件後，在室溫操作下此一元件的臨界電流值為84 mA，電光轉換效率為9%；當操作溫度增加至105 ºC，臨界電流值增加至188 mA，特徵溫度(characteristic temperature, T_0)為118 K。為改善元件高溫高注入電流特性，我們更嘗試於活性層量子井中加入磷砷化鎵($GaAs_{0.9}P_{0.1}$)電子阻礙層，發現雖然於室溫下臨界電流值為99 mA，但當操作溫度為105 ºC時臨界電流值降低至172 mA，特徵溫度(characteristic temperature, T_0)為155 K。模擬結果亦證實加入磷砷化鎵做為電子阻礙層確實可以防止電子溢流，但卻也有電洞分布不均勻現象(hole inhomogeneity)產生而導致在低溫及低電流操作下元件之臨界電流值增加。而為防止電子溢流現象發生，我們更提出在磷砷化鎵電子阻礙層中增加磷成分至15–20%來得到較高特徵溫度值之雷射元件。

總而言之，在本論文中我們嘗試在半導體發光元件，包含紫外線發光二極體、紅光共振腔發光二極體、850-nm面射型雷射以及1.3-μm側射型雷射的磊晶結構上，設計最佳化結構來防止電子溢流現象發生進而提升元件的操作性能。祈望這些觀念與經驗未來能對元件磊晶者在結構設計上有所裨益。

Study of Structure Optimization in III-V Semiconductor Light Emitting Devices

Student : Yi-An Chang Advisor : Dr. Hao-Chung Kuo

Dr. Shing-Chung Wang

Institute of Electro-Optical Engineering

National Chiao Tung University

Abstract

In this dissertation, the improvement in operation performance of III-V optoelectronic semiconductor light emitting devices, which include ultraviolet (UV) light-emitting diode (LED), 660-nm red resonant-cavity LED, 850-nm vertical-cavity surface-emitting laser (VCSEL), and 1.3-μm edge-emitting laser (EEL), were studied. The key technologies for semiconductor light emitting devices to possess better output performance and high operation stabilities are the epitaxial crystal quality and the design of epitaxial structure. Noteworthily, the structure design is more important if we were to have a stable output performance in high temperature and high injection current operation. By using the epitaxial technology – metalorganic chemical vapor deposition (MOCVD) to grow the structures and advanced simulation programs to give theoretical analysis, the operation performances of semiconductor light emitting devices are investigated and improved. Mainly, we focus on confining the electrons effectively in the quantum well (QW) active region to reduce the electronic leakage current so as to improve the output performances.

In the research of UV LED, to emit an emission wavelength of 370 nm, quaternary AlGaInN is utilized as QW material during the epitaxy of UV LED. The device after standard process as 300×300 μm^2 size chip can provide a maximal output power of 4 mW and an external quantum efficiency of 1.2%. With an aim to enhance the output power of

UV LED, we then theoretically investigate the effect of the number of QWs and the aluminum content in AlGaN electron-blocking layer on the UV LED output performance. After fitting in with the experimentally demonstrated output performance of UV LED, we find that the UV LED can provide a better output performance when the aluminum content in AlGaN electron-blocking layer is in a range of 19–21% and the AlGaInN QW number is in a range of 5–7.

In the research of 650-nm RCLED, it is known that the conduction band offset value in AlGaInP material QW active region is approximately 300 meV. When the device is under high temperature operation, the electron leakage problem may become more serious and consequently leading to the degradation of output performance. By means of widening the resonant cavity to a thickness of three wavelength (3 λ), the degree of power variation between 25 and 95 ºC for the device biased at 20 mA is apparently reduced from -2.1 dB for the standard structure design (1-λ cavity) to -0.6 dB. The current dependent far field patterns also show that the emission always takes place perfectly in the normal direction, which is suitable for plastic fiber data transmission. To optimize the RCLED structure, we continue numerically studying the structure dependent output performance by using an advanced simulation program. After fitting in with the experimentally demonstrated output performances of RCLEDs, we analyze the percentage of electron leakage current of the two structures, and we find that the stable temperature dependent output performance of 3-λ-cavity RCLED is attributed to the reduction of electron leakage current.

In the research of 850-nm VCSEL, we first theoretically investigate the gain-carrier characteristics of $In_{0.02}Ga_{0.98}As$ and InAlGaAs QWs of variant In and Al compositions. More compressive strain, caused by higher In and Al compositions in InAlGaAs QW, is found to provide higher material gain, lower transparency carrier concentration and transparency radiative current density over a temperature range of 25−95 ºC. Then we choose $Al_{0.08}Ga_{0.77}In_{0.15}As$ as QW material in the epitaxy of 850-nm VCSEL structure.

After standard oxidation confinement process, this device can provide a threshold current of 1.47 mA with a slope efficiency of 0.37 mW/mA at 25 ºC, and the threshold current increases to 2.17 mA with a slope efficiency reduction of 32% when the device temperature is raised to 95 °C. To improve the operation performance of 850-nm VCSEL, a 10-nm-thick $Al_{0.75}Ga_{0.25}As$ electron-blocking layer is employed in the QW active region for the first time, and the threshold current at 25 ºC is found reducing to 1.33 mA with an increment of slope efficiency to 0.53 mW/mA. When the device temperature raises to 95 °C, the threshold current increases by only 0.27 mA and the slope efficiency drops by only 24.5%. Numerical simulation is also done to analyze the effect of the electron-blocking layer on the output performance of 850-nm VCSEL, and the results show that the output performance is improved by the reduction of electron leakage current.

In the research of 1.3-μm InGaAsN/GaAsN EEL, there has been several works investigating using strain GaAsN as direct barrier. Using GaAsN in the epitaxial growth can balance the highly compressive strain in InGaAsN QW and reduce the phenomenon of nitrogen out-diffusion from the well. However, it is a small bandgap material system, which indicates that the electron leakage may become more serious if adding more nitrogen into GaAsN barrier. Therefore, in the first instance, the temperature effects on the optical gain properties of single $In_{0.4}Ga_{0.6}As_{0.986}N_{0.014}$ QW with GaAsN barrier of different nitrogen compositions are studied for optimization. Theoretically, we suggest using $GaAs_{0.995}N_{0.005}$ as direct barrier can be a better choice with the considerations of epitaxial growth and electron confinement. Then we choose $In_{0.4}Ga_{0.6}As_{0.986}N_{0.014}/GaAs_{0.995}N_{0.005}$ as active region in the epitaxial growth of 1.3-μm EEL structure. After standard process as 4×100 μm^2 size chip, this device can provide a threshold current of 84 mA with a slope efficiency of 0.09 mW/mA. When the device temperature increases to 105 °C, the threshold current becomes 188 mA and a characteristic temperature value (T_0) of 118 K is obtained. To improve the operation performance of 1.3-μm

$In_{0.4}Ga_{0.6}As_{0.986}N_{0.014}/GaAs_{0.995}N_{0.005}$ EEL, we also try to insert a $GaAs_{0.9}P_{0.1}$ layer as electron blocking layer in the epitaxial growth of 1.3-μm EEL. The threshold current of the device at 25 °C becomes 99 mA and a slope efficiency of 0.11 mW/mA is obtained. The threshold current at 105 °C only increases to 172 mA with a T_0 value of 155 K and the reduction of slope efficiency becomes less. Numerical simulation is done to analyze the effect of the electron blocking layer on the output performance of 1.3-μm EEL. The results show that the electron leakage current is reduced with the use of a high-bandgap $GaAs_{0.9}P_{0.1}$ layer. Further theoretical simulation work of investigating the effect of increasing the phosphide composition in GaAsP electron-blocking layer on the T_0 value is also done. And, we find that increasing the phosphide composition in GaAsP to 15–20% can provide a better T_0 value.

In a summary, the III-V optoelectronic semiconductor light emitting devices, which include 370-nm UV LED, 660-nm RCLED, 850-nm VCSEL, and 1.3-μm EEL, are experimentally demonstrated and theoretically analyzed for a purpose of reducing the electron leakage current and thus improving the operation performance. We hope those all will turn into useful information in the design and epitaxy of optoelectronic semiconductor light emitting devices.

誌謝

博士論文的順利完成，首先要對辛苦指導我四年的郭浩中教授以及王興宗教授致上我最深忱的敬意，因為他們的耐心指導，讓我可以快速且有效率地進入專業領域並找到研究方向。在博士班求學過程中，不論是在專業的實務與經驗或學理上探討，他們也總是能提供諸多寶貴建議與指導，讓我不至於在研究的道路上產生迷思。也感謝交通大學光電所盧廷昌教授與張振雄教授、彰化師範大學物理系所郭艷光教授、台灣大學電機工程學系彭隆瀚教授、成功大學電機工程學系張守進教授以及光電所許進恭教授、提供的諸多寶貴建議與指導，讓論文內容可以更加完善。

感謝禧通科技施江霖博士、賴利弘博士與賴利溫博士，由於他們豪邁無私的個性首肯讓我以學生身分進入公司學習磊晶與製程技術，也讓我提早擁有社會市場上的實戰經驗以及教導我如何扮演好一個研發人員的角色，同時也要感謝禧通科技那群可愛的同事們，蔡睿彥博士、俊龍、怡宗、妙佳、佳勳、千慧、心馨、育德、意蓉、佳萍、僑宴、琇圓、正斌、乾森，以及海德威電子謝文昇副總、Joe、James、Lynn、Ricky，謝謝你們三年來的陪伴。在學校生活中，特別感謝黃根生博士以及余長治、賴芳儀、張亞衡、薛道鴻學長姐們在學業、學術研究上的幫助以及工作經驗上的分享，有他們的引導讓我更清楚明白未來道路的規劃。感謝博士班同學志強、泓文、榮堂在課業及研究上一路相互扶持奮鬥與努力，以及學弟妹們宗憲、德忠、裕鈞、傳煜、永龍、俊毅、國鋒、敏瑛、蕙婷、文燈、永昌在實驗量測上的協助。也感謝彰化師範大學物理與光電系所學弟妹們勝宏、俊榮、秀芬、尚衛在程式運算與理論模擬分析上的幫忙。謝謝實驗室助理淑致、麗君在行政上的幫忙，所辦黃小姐、許小姐、湯先生、劉小姐、崔小姐等在計畫及行政作業上的幫忙。並感謝所有曾經幫助過我的良師益友們。

最後最該感謝的是我的家人--爸爸、媽媽以及哥哥與姐姐，還有女朋友 Jessica 以及她的家人們。有你們精神上的支持、體諒與實質生活上的幫忙、照顧，讓我可以在沒有後顧之憂的情況下專心完成博士學業。謝謝你們！你們永遠是我的最愛。也謝謝曾經幫過我的人！謝謝你們！

詒安　于 96 年 9 月 5 日

交通大學光電工程研究所

Contents

List of figures

Chapter 1

Chapter 3

Chapter 4

Chapter 5

Chapter 6

List of tables

Chapter 1

Chapter 3

Chapter 1 Introduction

Since the first demonstration of high electroluminescence radiation from GaAs p-n junction in the early 1960s [1–5], compound semiconductors have functioned constantly in being promising materials in optoelectronic devices. So far, the optoelectronics has become an important part of our lives. Wherever converting current into optical signal or vice versa, the optoelectronic semiconductor devices all have a unique advantage, that is, they are tiny, and providing a high conversion efficiency that meets the steadily increasing mankind's requirements. Examples include light-emitting diodes (LEDs) in illumination and other applications, photo-detectors in remote control sensors, and laser diodes (LDs) for digital disk storage system. While considering using the optoelectronic devices as active light sources, it is indubitably that group III-V compounds are the most excellent candidate because of their physically direct bandgap property. The devices such as LEDs, resonant-cavity light-emitting diodes (RCLEDs), edge-emitting laser diodes (EELDs), and vertical-cavity surface-emitting lasers (VCSELs) have been commercialized for several decades. These emitters can be used in the application of solid-state lighting, outdoor displays, laser pointer, printer, DVD players, and fiber communication etc. While selecting a suitable material to be the active media, a wide emission wavelength range covering untraviolet–blue–green–red–infrared region of the spectrum can be obtained. As an illustration, the devices made by GaN-based material can provide high efficient illumination in ultraviolet to green wavelength range and white emission. For high efficient yellow–red emission, the choice of the active media material grown on GaAs substrate is InGaP/InGaAlP. As extending the emission wavelength to infrared, the active media material can be InGaAlAs, InGaAsP, and InGaAsN.

These semiconductor light emitting devices have indeed made our living

environment colorful and brilliant. The unmitigated research efforts worldwide have resulted in making these emitters having better output performances. However, with an aim to improve the emitting power and efficiency of the semiconductor light emitting devices, substantial works are still needed. In which, further experimental demonstrations and theoretical simulation are both intensively required. The experiments facilitate the growth of high quality films that reduce the internal loss caused by the defects. The theoretical simulation can provide a more detailed understanding of device physics and simultaneously give a qualitative analysis to optimize the existed device structures. As these efforts continue, it is expected to enhance the output performances of the optoelectronic semiconductor devices.

In this dissertation, the improvement in operation performance of III-V optoelectronic semiconductor light emitting devices, which included UV-LED, 650-nm red RCLED, 850-nm VCSEL, and 1.3-μm EELD, were studied. The respective devices were fabricated. As well, in order to better understanding the device physics so as to improve the output performances, three advanced simulation programs developed by Crosslight Software, Inc. (APSYS, LASTIP, PICS3D) [6] were employed. Specifically, the physical discussion of reducing electronic leakage current in the fabricated devices was focused to improve the high temperature and high current injection device output performances. The following subsections in this chapter were intended to give an investigation and historical review of the nitride based LED, RCLED, and semiconductor lasers including EELD and VCSEL devices. The physical models in the software, regarding band structure calculation, drift-diffusion model, spontaneous and stimulated emissions, heat flux equations, and etc. were described in Chapter 2. Characteristics of the fabricated devices and the theoretical analysis were described in Chapters 3 to 6, respectively. Finally, conclusions were given in Chapter 7.

1-1 Historical review of nitride based LEDs

In the history of III-nitride materials, GaN binary alloy was first synthesized by Juza and Hahn with passing ammonia over hot gallium, and produced small needles and platelets for the purpose of studying its crystal structure and lattice constant. In 1958, small crystals of GaN were produced with the same technique by Grimmeiss and Koelmans to measure their photoluminescence (PL) spectra. Ten years later, a large layer of GaN grown on sapphire (Al_2O_3) substrate by using chemical vapor deposition technique was demonstrated by Maruska and Tietjen [16]. As regarding the fabrication of GaN-based LED devices, the first demonstration was reported by Pankove *et al*. in 1971. However, the early works were eventually forsaken because of the lack of advanced epitaxial technique and especially encountering the fundamental material problems. As shown in Figure 1.1, the lattice constant of GaN is 3.189 Å with an energy bandgap of 3.39 eV. At present, sapphire has become the most commonly used substrate for the growth of III-nitride materials. This substrate has several advantages such as cheaper than SiC, high hardness, high heat-resistance, and particularly the free of absorption for green, blue, and ultraviolet photons. However, despite these advantages, there are still some disadvantages; e.g., the interface between GaN and sapphire substrate exists a large lattice mismatch of 15% [8], [9], resulting in a very high dislocation density. Besides, sapphire is a dielectric material, so that both n and p contacts shall be on top of the devices, and etching techniques are inevitably required. Even the sapphire can be the substrate for growing III-nitride materials, the noticeable lattice mismatch, which results in the poor crystal quality, obstructs the early development of III-nitride LEDs.

This high dislocation problem was not solved until 1983 when Dr. Yoshida improved the crystal quality of GaN films with the use of AlN-coated sapphire substrate

[11]. Later, high-quality optically flat surfaces of GaN thin films had been successfully grown by using AlN nucleation buffer layer with metal-organic chemical vapor deposition (MOCVD) technique by Prof. Akasaki *et al.* [12]. In 1991, S. Nakamura changed AlN thin films with low-temperature growing amorphous GaN thin films as nucleation layer, and mirror-flat GaN thin films were obtained under high-temperature growing [13].

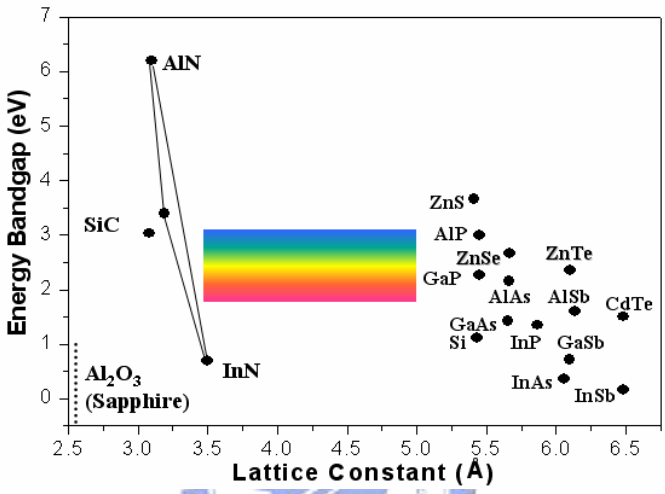

Figure 1.1 Lattice constant of semiconductor materials as a function of their bandgap energy.

Nevertheless, the high n-type background doping in intrinsic GaN film also causes another incapability in fabricating GaN p-n junction LEDs. As many conformation of semiconductor devices, a p-n junction is always required. For n-type GaN, it could be easily achieved with an n-doping level of 1×10^{17} ~ 2×10^{19} cm^{-3} by Si or Se dopant atoms. For forming p-type GaN layer, even various types of acceptor atoms including Mg and C were tried, it only led to compensated high resistivity material. This bottleneck was first broken through by Akasaki *et al.* [14] by low energy electron beam irradiation (LEEBI) treatment. A hole concentration of 1×10^{17} and a low resistivity of 12 Ω·cm were obtained, respectively. Three years later, the Mg-doped GaN with p-doping level of 3×10^{18} cm^{-3} and a resistivity of 0.2 Ω·cm was found more conductive by Nakamura with a treatment of thermal annealing in a N_2 ambient [15].

To achieve high-brightness GaN-based LED, another breakthrough of high-quality InGaN films came. In 1990s, a blue InGaN/GaN double-heterostructure LED was fabricated by Nakamura *et al*. for the first time. With the use of two-flow MOCVD technique, the substrate was heated to 1050 ºC in a stream of hydrogen. Then the temperature was lowered down to 510 ºC for the growth of GaN nucleation layer. Next, the substrate was reheated to 1020 ºC to grow 4-μm n-type GaN film, followed by the 20-nm-thick Si-doped InGaN active layer when the temperature was decreased to 800 ºC. The temperature was then increased to 1020 ºC to grow p-type Mg-doped GaN film. The total thickness was about 4.8 μm, and the surface of p-type GaN was partially etched until the n-type layer was exposed. Finally, a Ni–Au contact was evaporated onto the p-type GaN layer and a Ti–Al contact onto the n-type GaN layer. The peak wavelength was 440 nm with a full width at half maximum (FWHM) of 20 nm at forward current of 20 mA [16].

The first candela-class blue LEDs were fabricated with the use of Si and Zn codoped InGaN active layer. A relatively low indium composition in InGaN layer was used as a result of high-indium InGaN layer might cause the degradation of luminescence intensity. The thickness of InGaN active layer was 50 nm, and the active layer was sandwiched between two 150-nm-thick $Al_{0.15}Ga_{0.85}N$ cladding layers. The output power and external quantum efficiency at 20 mA were 1.5 mW and 2.7% [17]. Soon afterward, the InGaN/InGaN multiple-QW structures and several novel designs were employed in GaN-based LEDs, and the first commercial GaN-based LEDs were commercialized by Nichia Chemical Company in 1990s. To date, it is less than fifteen years that high-brightness GaN-based LEDs are used throughout the world, for example, in the applications of full-color displays, traffic signals, and other promising areas of high-definition DVD optical storage, chemical processes, and medical applications [18–20].

III-nitride and their alloys represent a very special class of material. They are indeed the best chosen for short wavelength emission due to their wide and direct energy bandgap. Unlike the arsine or phosphide materials, there is not a suitable substrate for their growth, and they are in the hexagonal (wurtzite) crystal system. Mostly, the polarization effect in GaN-based materials has been found much stronger than other III-V compounds [21]. Next, the material properties of wurtzite GaN and its relevant alloys are investigated.

1-1-1 Wurtzite GaN material property

Most III-V compound semiconductor materials are belonged to zinc-blende-type crystals. For GaN and its relevant alloys, they can be zinc-blende type; however, they are commonly grown as wurtzite crystal, which exhibits a hexagonal Bravais lattice, as depicted in Figure 1.2. In crystallography, the wurtzite structure is closely related to the zinc-blende structure, and in fact it is a member of hexagonal crystal system. For most epitaxial GaN growth film, the optic axis (*c*-axis) [0001] is typically oriented normal to the surface. The strain tensor components are evaluated by specifying five distinct, nonvanished elastic constants for wurtzite crystals: C_{11}, C_{12}, C_{13}, C_{33}, and C_{44}. The nondiagonal strain-tensor components vanish while $\varepsilon_{xx} = \varepsilon_{yy} = \frac{a_{GaN} - a_{lc}}{a_{lc}}$, $\varepsilon_{zz} = \frac{c_{sub} - c_{lc}}{c_{lc}} = -2\frac{C_{13}}{C_{33}}\varepsilon_{xx}$.

For the band structure of wurtzite GaN based materials, it is often characterized by the zone-center $k \cdot p$ method. The spin-degenerate conduction band is described by the anisotropic, parabolic form with wave functions comprised of the *s*-orbital (angular momentum $l = 0$) states:

$$H_c = E_c + \frac{\hbar^2 k_{//}^2}{2m_{//}^*} + \frac{\hbar^2 k_z^2}{2m_{\perp}^*} + a_1\varepsilon_{zz} + a_2(\varepsilon_{xx} + \varepsilon_{yy}) \qquad (1.1)$$

in which $k_{//}$, k_z are the wave vectors and $m_{//}^*$, $m_{\perp}^*$ are the effective masses along

the in-plane and *c*-axis directions. a_1 and a_2 are the conduction band deformation potentials. The valence band is described by a 6×6 Hamiltonian transfer matrix including heavy-hole (HH), light-hole (LH), and crystal-field split-off hole (CH) bands [22–24] as follows:

$$H_{6\times6} = \begin{bmatrix} H^U & 0 \\ 0 & H_L \end{bmatrix} \tag{1.2}$$

where

$$H^U = \begin{bmatrix} F & K_t & -iH_t \\ K_t & G & \Delta - iH_t \\ iH_t & \Delta + iH_t & \lambda \end{bmatrix}, \quad H^L = \begin{bmatrix} F & K_t & iH_t \\ K_t & G & \Delta + iH_t \\ -iH_t & \Delta - iH_t & \lambda \end{bmatrix} \tag{1.3}$$

The matrix elements are

$$\begin{aligned}
F &= \Delta_1 + \Delta_2 + \lambda + \theta \\
G &= \Delta_1 - \Delta_2 + \lambda + \theta \\
\lambda &= \frac{\hbar^2}{2m_0}(A_1 k_z^2 + A_2 k_t^2) + \lambda_\varepsilon \\
\lambda_\varepsilon &= D_1 \varepsilon_{zz} + D_2(\varepsilon_{xx} + \varepsilon_{yy}) \\
\theta &= \frac{\hbar^2}{2m_0}(A_3 k_z^2 + A_4 k_t^2) + \theta_\varepsilon \\
\theta_\varepsilon &= D_3 \varepsilon_{zz} + D_4(\varepsilon_{xx} + \varepsilon_{yy}) \\
K_t &= \frac{\hbar^2}{2m_0} A_5 k_t^2 \\
H_t &= \frac{\hbar^2}{2m_0} A_6 k_z k_t \\
\Delta &= \sqrt{2}\Delta_3 \\
k_t^2 &= k_x^2 + k_y^2
\end{aligned} \tag{1.4}$$

The A_i parameters are related to the hole effective masses. The crystal field splitting $\Delta_{cr} = \Delta_1$, and the spin-orbit splitting is $\Delta_{so} = 3\Delta_{21} = 3\Delta_3$. As shown in Figure 1.3, the band structure of wurtzite GaN near the top of valence band is schematically plotted. The bottom two pair bands are the CH splitting bands. The top four bands are split by the spin-orbit interaction into two pairs with heavy and light hole effective masses in the

plane.

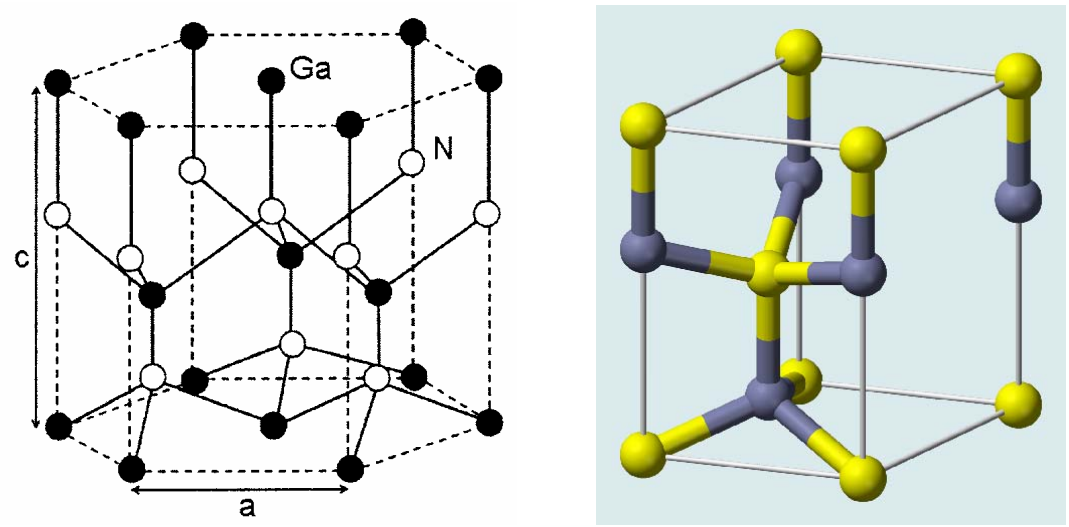

Figure 1.2 (a) Wurtzite crystal with lattice constants c and a. (b) The unit cell of wurtzite GaN crystal.

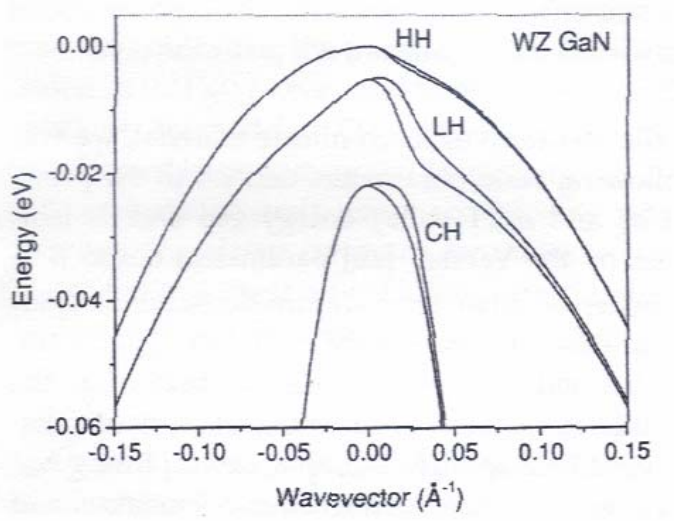

Figure 1.3 Valence-band structure of wurtzite GaN.

1-1-2 Band parameters

Binary alloy

Unlike III-V arsenide and phosphide semiconductor materials, the physics related to GaN based materials has not been well developed. The troubled growth technique and the potentials in GaN based materials are both very attractive that much effort is paid for realizing its material properties. For optoelectronic semiconductor devices, the

bandgap energy of each semiconductor material is undoubtedly one of the most important parameters. As expressed by the *Varshni* formula [25], the bandgap energy of III-V semiconductor material at temperature *T* can be:

$$\mathrm{E_g}(T) = E_g(0) - \frac{\alpha \cdot T^2}{T + \beta} \tag{1.5}$$

where $E_g(T)$ is the bandgap energy at temperature T, $E_g(0)$ is the bandgap energy at 0 K, α and β are material-related constants. The value of β is approximately equal to the Debye temperature at 0 K. Several kinds of measurements such as optical absorption, photoreflectance, photoluminescence are employed to determine these constants. In the GaN based materials, binary GaN, AlN, and InN can also be expressed by the *Varshni* formula accurately within a few meV.

Since the early 1970s, a bandgap energy of 3.5 eV for wurtzite GaN has been realized [26], [27]. To determine the bandgap energy more accurately, a luminescence measurement of the exciton lines is preferred. The research has shown that the actual gap is recovered by adding the estimated binding energy to the observed exciton transition energy. The free A exciton (E_A) transition energy, which can be determined quite precisely, is the most reliable indicator in relatively-pure GaN. A range of A-exciton transition energies at 0 K, 3.474–3.496 eV, has been indicated [28–30], while with A-exciton binding energies range from 18 to 28 meV [31–34]. These values have been critically reviewed by I. Vurgaftman [35], and a value of 3.510 eV for the zero-temperature energy gap is recommended. In the mean time, An average values of the *Varshni* parameters α=0.909 meV/K and β=830 K are given, while they believe that GaN device characteristics tend to be relatively insensitive to the precise values of the *Varshni* parameters owing to the small relative change in the energy bandgap (72 meV between 0 and 300 K).

Among the III-V semiconductor materials, AlN alloy has in fact the highest energy

bandgap. As well being a direct-bandgap material the AlN alloy tends to be technologically significant because of its high bandgap property in playing a role of the barrier or cladding layers in the GaN-based devices. The *Varshni* parameters for AlN, summarized by I. Vurgaftman, obtained with variant measurements such as cathodoluminescence (CL), spectroscopic ellipsometry, and photoreflectance have been obtained. The room temperature energy bandgap of AlN can be in a range of 6.11–6.2 eV. The *Varshni* parameters α=1.799 meV/K, β=1462 meV for wurtzite AlN are recommended.

As regards wurtzite InN, its bandgap energy determined by optical absorption was early determined to be in a range of 1.7–2.2 eV [36–40]. In stead of using an advanced growth technique to obtain high crystal quality, the thin InN film was sputtered, which in term results in an uncertainty. Before 2001, most has believed that the energy bandgaps of wurtzite InN at low temperature and room temperature are 1.997 and 1.97 eV, respectively. The *Varshni* parameters are α=0.245 meV/K, β=624 meV [41]. This InN energy bandgap value is repudiated in 2001 since single crystal InN film is successfully obtained. The re-evaluated wurtzite InN bandgap energy is in the 0.7–0.8 eV range [42], [43]. The *Varshni* parameters are regarded unchanged as prior. Other significant band parameters such as effective masses, splitting energies, and deformation potentials etc. for GaN, AlN, and InN binary alloys are listed in Table 1.1 [35].

Table 1.1 Band parameters of wurtzite binary GaN, AlN, and InN alloys.

Parameters	GaN	AlN	InN
a_{lc} (Å) at T=300 K	3.189	3.112	3.545
c_{lc} (Å) at T=300 K	5.185	4.982	5.703
E_g (eV)	3.51	6.25	0.78
α (meV/K)	0.909	1.799	0.245
β (K)	830	1462	624
Δ_{cr} (eV)	0.010	-0.169	0.040

Δ_{so} (eV)	0.017	0.019	0.005
$m_e^{//}$	0.2	0.32	0.07
$m_e^{\perp}$	0.2	0.30	0.07
A_1	-7.21	-3.86	-8.21
A_2	-0.44	-0.25	-0.68
A_3	6.68	3.58	7.57
A_4	-3.46	-1.32	-5.23
A_5	-3.40	-1.47	-5.11
A_6	-4.9	-1.64	-5.96
A_7 (eV Å)	0.0937	0	0
a_1 (eV)	-4.9	-3.4	-3.5
a_2 (eV)	-11.3	-11.8	-3.5
D_1 (eV)	-3.7	-17.1	-3.7
D_2 (eV)	4.5	7.9	4.5
D_3 (eV)	8.2	8.8	8.2
D_4 (eV)	-4.1	-3.9	-4.1
D_5 (eV)	-4.0	-3.4	-4.0
D_6 (eV)	-5.5	-3.4	-5.5
c_{11} (GPa)	390	396	223
c_{12} (GPa)	145	137	115
c_{13} (GPa)	106	108	92
c_{33} (GPa)	398	373	224
c_{44} (GPa)	105	116	48
d_{13} (pm/V)	-1.6	-2.1	-3.5
d_{33} (pm/V)	3.1	5.4	7.6
d_{15} (pm/V)	3.1	3.6	5.5

Ternary InGaN and AlGaN alloys

For nitride based ternary alloys, due to the smaller bandgap energy of InGaN material than that of GaN, InGaN ternary alloy can be used as a promising active heterostructrue or QW material to emit in the violet and blue region of the spectrum with a carrier confinement layer of AlGaN. The In and Al content in each respective layer is commonly less than 20% when consider having a high quality film. In 1990, there has been significant process in the growth and characterization of the InGaN material [44–46]. The bandgap energy of InGaN measured by Osamura *et al.* [47]

across the entire compositional range has a smooth variation with some bowing by

$$E_g^v(InGaN) = v \cdot E_g(InN) + (1-v) \cdot E_g(GaN) - b_{InGaN} \cdot v \cdot (1-v) \quad (1.6)$$

. The bandgap energy of the ternary alloy is assumed with linear combination of two binary alloys with a second-order correction. The b value is so-called bowing parameter which is accounted for the deviation from the linear interpolation between the two binary alloys. A bowing parameter value of 1.0 eV for InGaN is early found either by experimentally fit to the PL data or numerical calculations [48–52]. A large bowing value in a range of 2.4–3.5 eV is also proposed, while I. Vurgaftman recommends that a bowing parameter value of 1.4 eV for InGaN [35], which bases on several prior works and the consideration of recent growth of high-quality high In content epitaxial film.

For AlGaN ternary alloys, Yoshida *et al.* observed that the band gap energy of AlGaN deviates upwards with increase in AlN composition [53]. Hagen *et al.* and Koide *et al.* observed that the bandgap energy of AlGaN deviated downward with the increase of AlN composition [54], [55]. They all believed that the bandgap energy could be described with linear combination of AlN and GaN binary alloys with a second-order correction by

$$E_g^w(AlGaN) = w \cdot E_g(AlN) + (1-w) \cdot E_g(GaN) - b_{AlGaN} \cdot w \cdot (1-w) \quad (1.7)$$

Even a large number of bowing parameter values is proposed, most researchers believes that the bowing parameter for AlGaN is positive, corresponding to be in a range of 0.353–1.38 eV [56–60]. A bowing parameter value of 0.7 eV for AlGaN, based on the consistent finding of the relatively small bowing parameter by the theories and experiments, is recommended by I. Vurgaftman [35].

Despite of the bandgap energy of ternary alloy can be expressed in linear combination of binary alloys with a bowing, other band parameters such as effective masses, splitting energies, and deformation potentials etc. for ternary alloy can be

calculated from the linear interpolation between the two binary alloys but with zero bowing parameter.

Quaternary InGaAlN alloy

While considering an optoelectronic light emitting device emitting in ultraviolet wavelength region, quaternary InGaAlN is preferred to be the active region material due to the lattice constant of InGaAlN can be tuned match, either tensile or compressive to GaN. That the design in QW active region can be more optimized therefore obtaining better output characteristics. Prior studies have found that the lattice mismatch is reduced by the incorporation of In with an In/Al ratio close to 1/5 and match to GaN [61]. Mostly, the band parameters of quaternary alloys can be expressed in linear interpolation formula as

$$P(In_xGa_{1-x-y}Al_yN) = x \cdot P(InN) + (1-x-y) \cdot P(GaN) + y \cdot P(AlN) \tag{1.8}$$

For the energy bandgap of InGaAlN, some has reported with rather small In fraction. M Asif Khan found that the energy bandgap of InGaAlN reduced almost linearly when In <2% [61]. A relationship for the calculation of composition dependent parameters by a weighted sum of ternary alloys has also been permitted, for instance, the bandgap energy of InGaAlN can be [62]

$$E_g(InGaAlN) = \frac{xy \cdot E_g^u(AlInN) + yz \cdot E_g^v(InGaN) + zx \cdot E_g^w(AlGaN)}{xy + yz + zx} \tag{1.9}$$

with

$$E_g^u(AlInN) = u \cdot E_g(InN) + (1-u) \cdot E_g(AlN) - b_{AlInN} \cdot u \cdot (1-u) \tag{1.10}$$

$$u = \frac{1-x+y}{2} \quad v = \frac{1-y+z}{2} \quad w = \frac{1-x+z}{2} \tag{1.11}$$

where x, y, and $z = 1-x-y$ represent the compositions of Al, In, and Ga in the InGaAlN alloy. The bandgap energy of ternary InGaN and AlGaN are depicted in expressions (1.6) and (1.7).

1-1-3 Spontaneous and piezoelectric polarizations

Built-in electric fields in semiconductors can be caused by spontaneous polarization P_{sp} and by strain-induced polarization P_{piezo} . In *c*-face nitride-based materials, these polarization effects were found much stronger when compared to other semiconductor materials [21]. In this situation, electrons and holes are separated in the quantum well, as indicated in Figure 1.4, the transition energy is reduced by the built-in field, leading to a red-shift of the emission wavelength. The wider the quantum well thickness, the more separated electrons and holes, and the less overlap of electron and hole carrier density distributions, which leads to a smaller optical gain and less spontaneous emission.

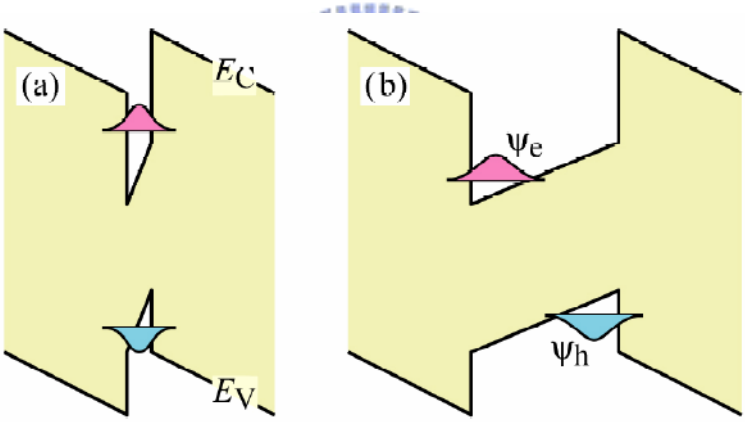

Figure 1.4 Band edges of conduction and valence bands

Fiorentini *et al*. has developed a way to estimate the interface charge density [63]. The spontaneous polarization of ternary nitride alloys can be expressed by

$$\begin{aligned} P_{sp}(Al_xGa_{1-x}N) &= -0.09\cdot x - 0.034\cdot(1-x) + 0.019\cdot x\cdot(1-x) \\ P_{sp}(In_xGa_{1-x}N) &= -0.042\cdot x - 0.034\cdot(1-x) + 0.038\cdot x\cdot(1-x) \\ P_{sp}(Al_xIn_{1-x}N) &= -0.090\cdot x - 0.042\cdot(1-x) + 0.071\cdot x\cdot(1-x) \end{aligned} \qquad (1.12)$$

As yet, there is no investigation on polarization properties focusing on the quaternary InGaAlN alloy. Only a similar way to that shown in expression 1.9 can be used for the calculation. The piezo-electric polarization can be calculated by

$$
\begin{aligned}
&P_{pz}(AlN) = -1.808 \cdot \varepsilon + 5.624 \cdot \varepsilon^2 \qquad for \qquad \varepsilon < 0 \\
&P_{pz}(AlN) = -1.808 \cdot \varepsilon - 7.888 \cdot \varepsilon^2 \qquad for \qquad \varepsilon > 0 \\
&P_{pz}(GaN) = -0.918 \cdot \varepsilon + 9.541 \cdot \varepsilon^2 \\
&P_{pz}(InN) = -1.373 \cdot \varepsilon + 7.559 \cdot \varepsilon^2
\end{aligned}
\tag{1.13}
$$

where ε is the basal strain of the binary compound considered. Linear interpolation formula is used for the calculation of ternary and quaternary nitride alloys. The total built-in polarization is the sum of spontaneous and piezo-electric polarizations.

1-1-4 Band alignment discontinuity

The value of band-offset is quite significant for the design of heterostructure devices. This value also plays a very important role in the analysis of energy band diagram. It is obvious that when two different materials are grown next to each other, both the conduction and the valence bands of the two materials will possess discontinuities at the interface. Quality and even feasibility of heterojunction device concepts often depend crucially on values of these band offsets. Several researchers determined the band-offset values of II-VI and III-V heterostructures experimentally by growth techniques such as MBE and MOCVD. Theoretical calculation indicated that the electronic structure in each layer of a heterojunction became nearly bulklike even a single atomic layer away from the interface, lending credence to the idealized notion of an abrupt band edge discontinuity. To determine band-offset values of semiconductor materials, X-ray photoelectron spectroscopy (XPS) and ultraviolet photoelectron spectroscopy (UPS) are primarily used by means of electron core level energies. Optical techniques, such as excitation PL and reflectivity, also present a more accurate tool to determine band-offset values. However, the devotion of the determination of the band-offset values in semiconductor heterojunction from experimental measurements and theoretical calculations exist large discrepancies, which may be related to the

difficulty of obtaining high quality epitaxial films.

Various types of band alignments can arise in semiconductor interfaces depending on the relative adjustment of energy bands with respect to each other. For semiconductor heterojunctions, there are two most common types of alignments. Type I alignment shows that the bandgap of one semiconductor lies completely within the bandgap of the other. This type is the most useful one for optoelectronic devices because the carriers are well confined in the smaller bandgap region. Type II alignment is the bandgaps of two materials overlap but not completely covering the other. For nitride-based materials, they all belongs to type I, and six different kinds of heterojunction combination, such as AlN/GaN, InN/GaN, GaN/AlN, InN/AlN, AlN/InN, and GaN/InN (A/B represents that A thin film is grown on top of B material) list. Table 1.2 lists some band-offset values of wurtzite nitride binary alloys reported by Martin *et al.* InN/GaN–GaN/InN and InN/AlN–AlN/InN heterojunctions show a significant forward-backward asymmetry. AlN/GaN–GaN/AlN heterojunctions give almost identical values. The asymmetric nature may be provided by strain induced piezoelectric fields [64] due to that the lattice constant of InN alloy is much larger than those of AlN and GaN, and the lattice mismatch between AlN and GaN is relative smaller than that between GaN and InN.

Table 1.2 Valence band-offset values of wurtzite nitride binary alloys (Unit: eV).

Reference	AlN/GaN	InN/GaN	GaN/AlN	InN/AlN	AlN/InN	GaN/InN
[65]	0.8±0.3	~	0.8±0.3	~	~	~
[66]	0.57±0.22	0.93±0.25	0.60±0.24	1.71±0.20	1.32±0.14	0.59±0.24
[67]	~	~	0.5±0.5	~	~	~
[68]	1.36±0.07	~	~	~	~	~
[69]	0.81	0.48	0.81	1.25	1.25	0.48
[70]	0.84	0.26	0.84	1.04	1.04	0.26

1-2 Historical review of RCLEDs

Novel concept of RCLED is first proposed and demonstrated by Schubert *et al*. in 1992 [71]. The active region of the device is placed in a resonant optical cavity, and the cavity is defined by a highly reflective (99%) and a moderately reflective mirror. As shown in Figure 1.5, the optical cavity mode can be in resonance with spontaneous emission of the active region. As a typical design of the optical cavity, it often has a thickness of 1/2- or 1-λ of the light emitted by the active region. The optical mode density can be strongly enhanced for on-resonance wavelengths. As a consequence, on-resonance transitions of the RCLEDs are enhanced. With the help of bottom highly reflective mirror, emission of light through the top side is enhanced, typically by a factor of two.

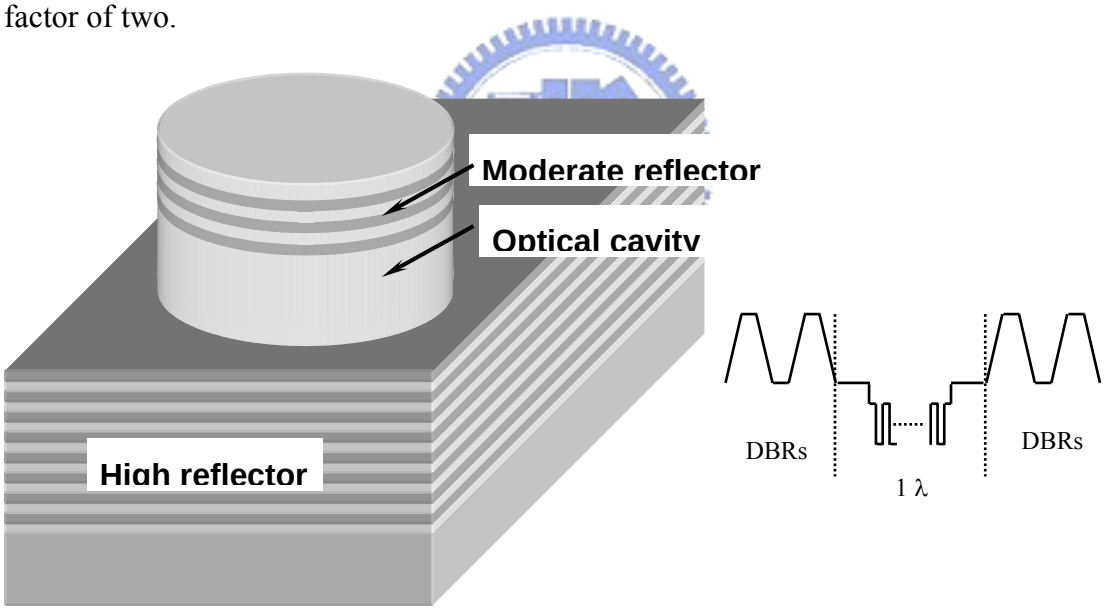

Figure 1.5 A schematic layer consequence of the RCLED device.

The placement of an active region inside a resonant cavity results in several improvements of the device characteristics. In comparison to typical LEDs, RCLEDs enjoy improved spectral purity, highly directional light output, less chromatic dispersion and improved modulation bandwidth. The spectral emission linewidth of a typical LED is determined by the thermal energy *k*T. However, the emission linewidth in RCLED is

determined by the quality factor *(Q factor*), which is defined as

$$Q = \frac{\nu}{\Delta\nu} = \frac{2n_c \cdot L_{cavity}}{\lambda} \cdot \frac{\pi\sqrt[4]{R_1 R_2}}{1-\sqrt{R_1 R_2}} \approx \frac{2n_c \cdot L_{cavity}}{\lambda} \cdot \frac{\pi}{1-\sqrt{R_1 R_2}} \tag{1.14}$$

where L_c is the cavity length, $\Delta\nu$ and ν are the linewidth and frequency of the Febry-Pérot resonance mode. R is the respective top and bottom reflectivity. As a result, the spectral linewidth of the RCLED can be a factor of 2–5 narrower to typical LED. Moreover, the emission wavelength shit with temperature is determined by the temperature coefficient ($d\lambda_{cavity} / dT$) of the optical cavity, not by the energy gap of the active region. This results in a higher temperature stability of the RCLED emission wavelength compared with typical LEDs. As compared with vertical-cavity lasers, the epitaxial complexity of RCLED structure is reduced since the reflectivity of upper distributed Bragg reflectors (DBRs) has to be less than 90%, and thus the RCLEDs provide thresholdless operation and better fabrication reliability.

1-2-1 RCLED design rules

A fundamental structure of an RCLED is plotted in Figure 1.6. Two mirrors with reflectivity R_1 and R_2 comprise a cavity and the active region is embedded. The reflectivity of the two mirrors is chose to be unequal so that the light exits the cavity predominantly through one of the mirrors. The active region shall be located preferably at the antinode location of the optical standing wave of the cavity. The active region has a thickness of L_{active} and an absorption coefficient of α. The cavity shows a one-wavelength cavity with a length of L_{cavity}. Owing to the light extraction, a fundamental design criterion for RCLED is that the light-exit reflector, R_1, should be lower than the reflectivity of the bottom reflector, which to make sure that the light can

emit in one direction. This is important for the light coupling into the small-core fiber, and in the application of display RCLED, where light should be emitted towards the observer.

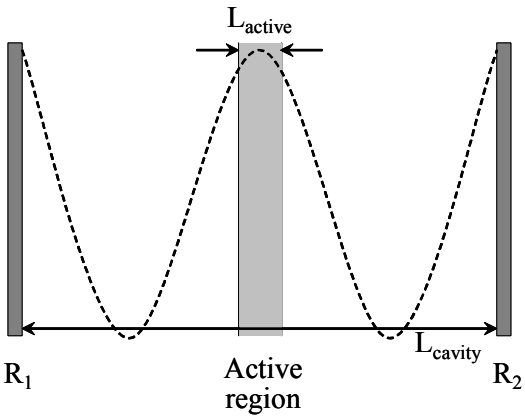

Figure 1.6 Schematic illustration of a resonant cavity consisting of two mirrors with reflectivity R_1 and R_2.

Secondly, the criterion arises from the design of the cavity length, L_{cavity}, which shall be as shorter as possible. As an expression of the integrated enhancement ratio, also called suppression ratio, given by

$$G_{\text{int}} = \frac{\pi}{2} \cdot G_e \cdot \Delta\lambda \cdot \frac{1}{\sigma\sqrt{2\pi}} \tag{1.15}$$

where it is assumed that the emission spectrum is in *Gaussian* distribution with a peak value of $(\sigma(2\pi)^{1/2})^{-1}$ and a linewidth of $\Delta\lambda_n = 2\sigma(2\ln 2)^{1/2}$. G_e is an enhancement factor at the resonance wavelength given by the ratio of the optical mode densities with and without a cavity as

$$G_e = \frac{\text{maximal optical mode density}}{\text{minimal optical mode density}} = \frac{\xi}{2} \cdot \frac{2}{\pi} \cdot \frac{\pi(R_1R_2)^{1/4}(1-R_1)}{(1-\sqrt{R_1R_2})^2} \cdot \frac{\tau_{cavity}}{\tau_0} \tag{1.16}$$

where the enhancement factor ξ has a value of 2 if the active region is located exactly at an antinode of the standing wave inside the cavity, and equals to 1 if the active region is smeared out over many periods of the standing wave. When the active region is located at a node, $\xi = 0$. τ_{cavity} and τ_0 represent the spontaneous emission lifetime with and with cavity, while the ratio ensures that the enhancement decreases if the

cavity lifetime is reduced as a result of the cavity. $\Delta\lambda$ is the cavity resonance bandwidth.

Finally, the integrated enhancement ratio can be

$$G_{\text{int}} = \frac{\xi}{2} \cdot \frac{\pi}{2} \cdot \frac{1-R_1}{1-\sqrt{R_1 R_2}} \cdot \sqrt{\pi \ln 2} \cdot \frac{\lambda}{\Delta\lambda_n} \cdot \frac{\lambda_{cavity}}{L_{cavity}} \cdot \frac{\tau_{cavity}}{\tau_0} \tag{1.17}$$

where λ and λ_{cavity} are the active region emission wavelength in vacuum and inside the cavity. One can easily observe that the light intensity can be enhanced by the minimization of the cavity length. The importance of a short cavity length is elucidated in Figure 1.7. The respective optical mode densities of two different cavities are shown in Figure 1.7(a) and (b). The natural emission spectrum of the active region is shown in Figure 1.7(c). A good overlap between the resonant optical mode and the active region emission spectrum is obtained for the shortest cavity. In the end, it means that a largest enhancement can be achieved if the fundamental cavity mode is in resonance with the active region emission.

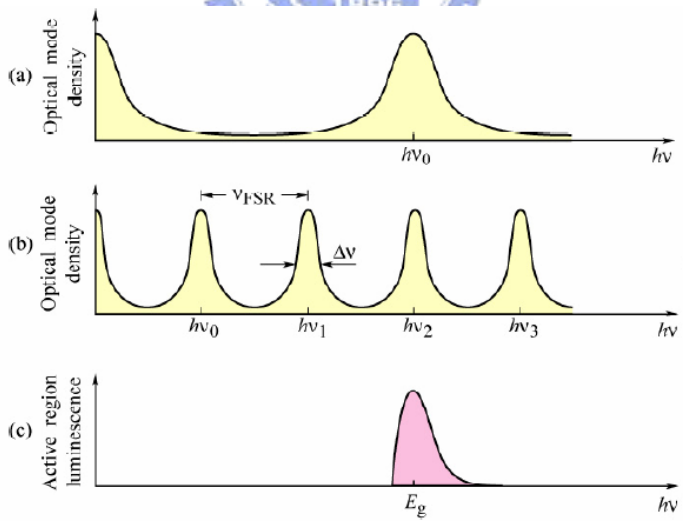

Figure 1.7 Optical mode density for (a) a short and (b) a long cavity. (c) Spontaneous emission spectrum of an LED active region.

While the emission from the active region resonates in the cavity, the phenomenon of self-absorption in the active region comes. It is in criterion that the re-absorption probability of photons emitted from the active region into the cavity mode shall be

much smaller than the extraction probability of photons, which can be written as

$$2 \cdot \xi \cdot \alpha \cdot L_{active} < (1 - R_1 R_2) \quad (1.18)$$

As an example of 650-nm RCLED with InGaP/InGaAlP active region, the reflectivity of two mirrors are design as $R_1 \sim 70\%$ and $R_2 \sim 100\%$, and the active region is assumed to be located well in the antinode of the optical standing wave with $\xi = 2$. The absorption coefficient for InGaP at 650 nm is assumed 10000 cm^{-1}. This criterion can be fulfilled if the active region thickness is less than 75 nm. That means the period of QWs in the active region is limited. If the criterion of expression 1.17 can not be fulfilled, photons will be re-absorbed by the active region, which in turn results in the re-emission along the lateral direction, not into the cavity mode or a possibility of non-radiation from the generated electron-hole pairs [72].

1-2-2 RCLED applications

The characteristics of RCLED shown above are desirable for local-area medium bit rate optical communication systems. In short-distance communication systems, polymethyl methacrylate plastic optical fibers (POFs) are increasing used as it provides a relatively low cost. Figure 1.8 shows the attenuation loss as a function of the wavelength in PMMA core fiber. At 650 nm, the preferred communication wavelength for POFs exists a relatively minimal attenuation loss of 0.15 dB/m [73]. Recently, the application of POFs has been extended to the automotive industry, such as media oriented systems transport (MOST), which needs to carrier 50–250 Mbps of data over POFs. MOST is a networking standard intended for interconnecting multimedia components in automobiles and other vehicles. It differs from existing vehicle bus technologies in that it's intended to be carried largely on an optical fiber bearer, thus providing a bus-based networking system at bit-rates far higher than available on

previous vehicle-bus technologies. MOST technology provides an environment where hardware is no longer the limiting factor to new multimedia application development. By approaching the network from a full system standpoint, all layers required for application development and system management have been defined and standardized.

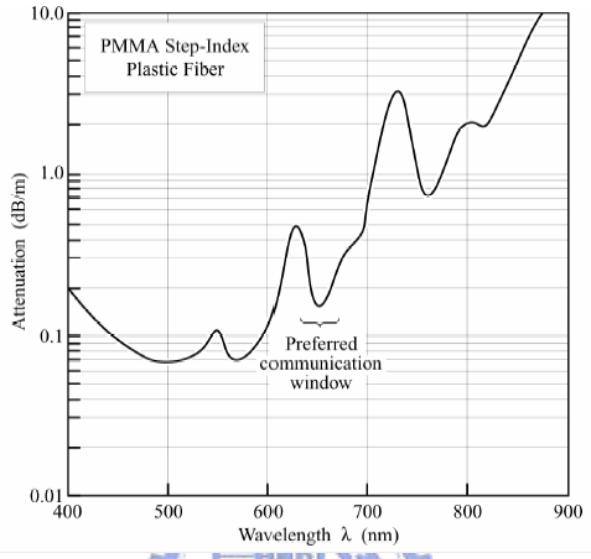

Figure 1.8 Attenuation of a PMMA step-index POF.

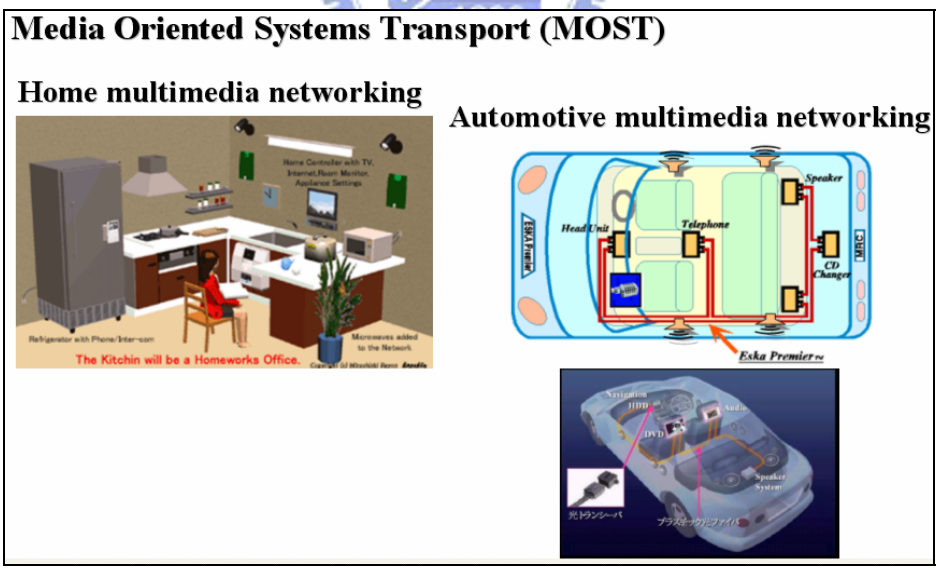

Figure 1.9 MOST technique concepts in home and automotive multimedia networking.

As depicted in Figure 1.9, entertainment functions can be distributed around the system with MOST. For example, a DVD player sends audio and video around the network for playback at several locations simultaneously. Intelligent but very low cost

audio devices can be strategically placed around a house or a vehicle, allowing the user to issue voice commands and control the system without having to be at a specific control terminal. Dynamic equalization and active noise cancellation on all audio signals flowing around a car is possible because digital data is available to all devices on the network in high quality.

1-3 Historical review of semiconductor lasers

Abbreviating “Light Amplification by the Stimulated Emission of Radiation” to a word, LASER, can be physically illustrated as photon multiplication when a single photon generated from the active region, traveling through a semiconductor, generates an identical second photon by stimulating the recombination of an electron-hole pair. The second photon exists the same wavelength and the same phase as the first photon, doubling the amplitude of their monochromatic wave. Such process repeats subsequently and leads to light amplification in the long run. However, the competing process is the absorption of photons by the generation of new electron-hole pairs. As a criterion of laser action, the population inversion shall be satisfied, that is, stimulated emission prevails when more electrons are present in the conduction band than in the valence band. As shown in Figure 1.10, the population inversion can be achieved by providing electrons from the n-doped side in the conduction band and holes from the p-doped side in the valence band. Continuous current injection or optical pump into the device leads to a continuous stimulated emission process but only if enough photons are unceasingly generated in the cavity oft the device. Because of this, a resonant cavity for optical feedback and two facet mirrors for providing a suitable reflectivity are required.

Laser action in semiconductors is initially demonstrated in 1962 by several groups. A forward-biased gallium arsenide (GaAs) p-n junction is performed and the optical gain is provided by the recombination of electrons and holes in the depletion region of

the p-n junction. The polished facets perpendicular to the junction plane forming a resonant cavity provide the optical feedback. A schematic p-n junction (homostructure) semiconductor laser in early stage is shown in Figure 1.11(a). This device exhibits a very high threshold current density ($J_{th} \geq 50$ kA/cm^2) due to a very poor confinement of carriers. To reduce the threshold current density, the p-n junction semiconductor laser is converted into heterostructure lasers, which consist of a layer of one material sandwiched between two cladding layers of another wider bandgap material. Heterostructure lasers can be further categorized as single-heterostructure or double-heterostructure devices, depending on whether the active region is surrounded on one or both sides by a higher bandgap cladding layer.

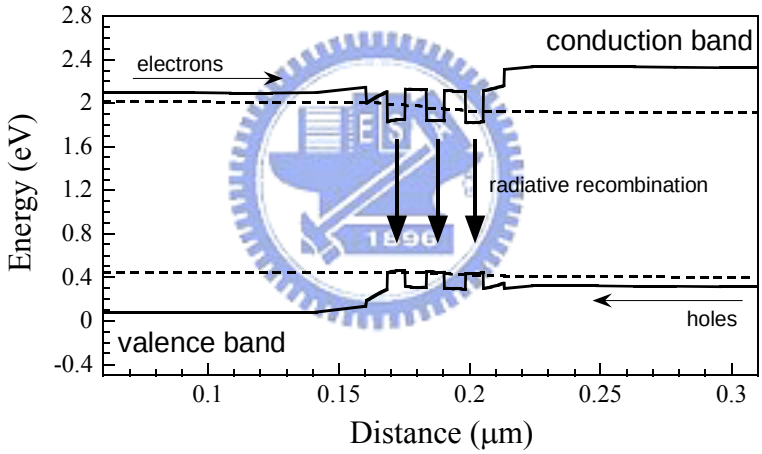

Figure 1.10 Band diagram of a p-n junction LD with triple-QWs illustrating carrier transport process

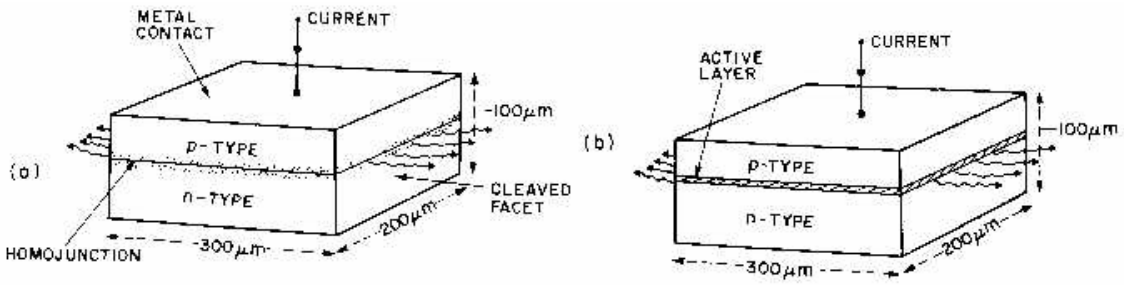

Figure 1.11 Schematic illustration of (a) p-n junction, and (b) heterostructure lasers with their typical physical dimensions.

A schematic heterostructure laser is shown in Figure 1.11(b). The first

room-temperature operation of a heterostructure laser ($GaAs/Al_xGa_{1-x}As$) is demonstrated by Kressel [74], Hayashi [75], and Alferov [76], etc. with the technique of liquid-phase epitaxy (LPE) in 1969. These lasers can only operate in pulse mode with a restriction of device heating. By 1975 the threshold current density is reduced when using a 0.1 μm thin active layer to two orders of magnitude over the first-made simple homostructure lasers in 1962. These efforts make the semiconductor laser to become a useful, practical, compact, coherent light source; however, the emission of early GaAs lasers usually operates in the wavelength range of 0.8–0.9 μm.

As shown in Figure 1.12, several direct-bandgap materials are also used to obtain semiconductor lasers for the purpose of obtaining various emission wavelengths. Early development of semiconductor lasers is done as well to another promising application in optical fiber communication. Long wavelength semiconductor lasers operating at the wavelengths of 1.31 and 1.55 μm are especially fascinating due to the relative low attenuation loss windows, as can be found in Figure 1.13, in silica fiber. In 1980s, quaternary indium gallium arsenide phosphide (InGaAsP) alloys turns out to be the more suitable material on the basis of lattice matching to InP substrate, and room-temperature operation InGaAsP semiconductor lasers for the requirement of commercialization are demonstrated [77–80].

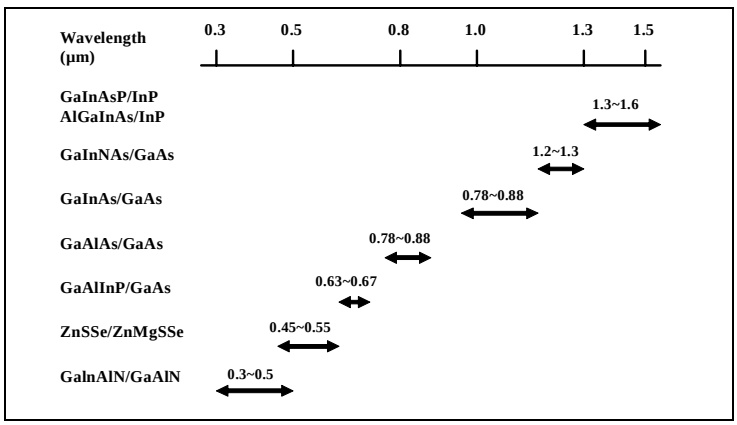

Figure 1.12 Various choice of the active region material for different range of emission wavelength.

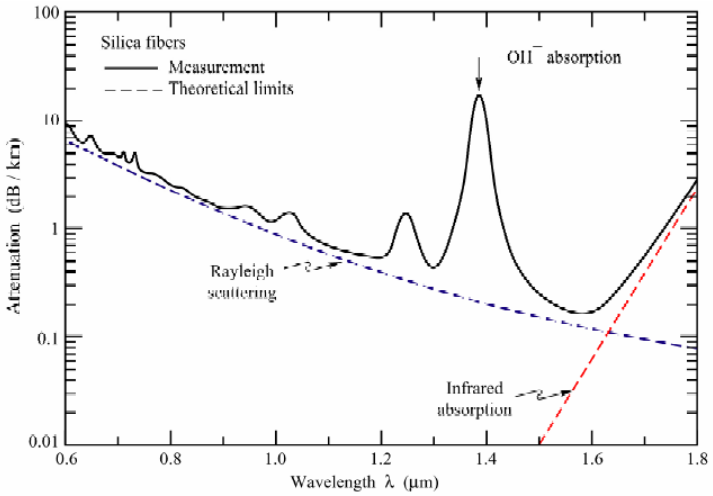

Figure 1.13 Attenuation in silica fibers (solid line) and theoretical limits (dash lines) given by Rayleigh scattering and molecular vibration (infrared absorption).

The semiconductor laser with visible red emission, using InGaP/ImGaAlP material, can be traced in 1980s. The InGaP/ImGaAlP material attracts much attention because the shortest emission wavelength of AlGaAs material can only be achieved to 680 nm while one would like to obtain a shorter red room temperature continuous-wave operation semiconductor laser. Also, the InGaP/InGaAlP material is developed because it can be grown onto the GaAs substrate with a lattice match condition of the indium composition in InGaAlP equaling to 50%, i.e., $In_{0.5}(Ga_{1-x}Al_x)P$. In 1982, the pioneering red InGaP/InGaAlP semiconductor laser is demonstrated under low temperature photoluminescence excitation [81]. One year later, Hino, Ashai, Kawamaru, *et al*. [82–84] successfully demonstrate a room temperature pulse current injection $Al_{0.5}In_{0.5}P/Ga_{0.5}In_{0.5}P/Al_{0.5}In_{0.5}P$ double heterostructure semiconductor lasers. Room temperature continuous-wave operation red InGaP/InGaAlP semiconductor laser is then developed in 1985 by MOCVD technique [85–87]. The structure is schematically plotted in Figure 1.14(a), and Figure 1.14(b) shows the temperature dependent light output versus current (L-I-V) characteristics. The lasing wavelength is 679 nm and the threshold current at room temperature is 109 mA.

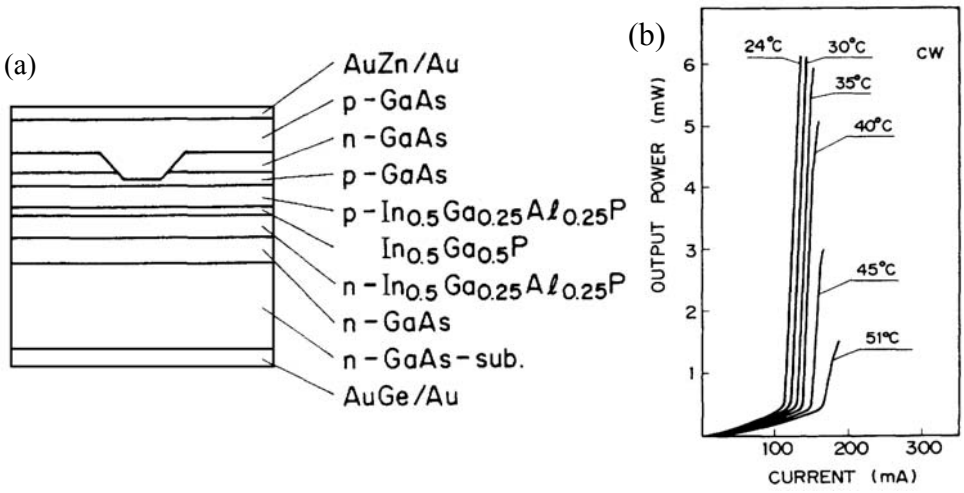

Figure 1.14 (a) A schematic plot of the first room-temperature continuous-wave operation red InGaP/InGaAlP semiconductor laser. (b) is the lasing characteristic.

Semiconductor laser with an emission wavelength less than 632.8 nm (He-Ne laser) in InGaP/InGaAlP system can be achieved by adding aluminum into InGaP active region, by using the misoriented GaAs substrate (001) with an off angle towards (111), or embedding quantum wells into the active region to degenerate the quantum-confined states that increases the transition energy. Even the first way is not preferred because adding aluminum into the active region during the crystal growth may cause an increase of oxide defect then degrading the crystal quality of active region and operation lifetime; in 1991, a lasing emission wavelength of 631 nm in InGaP/InGaAlP semiconductor laser is demonstrated by adding an aluminum composition of 15% into InGaP active region with a 7º misoriented GaAs substrate. The lasing characteristics could be comparable to the laser structure with QW active region on that time. As for QW semiconductor lasers, it is not until 1980s while the epitaxial techniques of molecular-beam epitaxy (MBE) and MOCVD are rapidly developed, the semiconductor lasers with quantum well active region can be well fabricated. Semiconductor lasers with QW active region design are very important because they provide a low threshold current operation, high power output, and high temperature operation characteristics. In 1990s, the semiconductor lasers with QW active region are vastly developed to fill in a

wide variety of ranging from the optical pick-up head in compact disk player to the transmitters optical fiber communication system, new applications in high-density compact disk storage system, local area data communications as well as consumer products. More reliable and manufacturable semiconductor lasers are demanded. Various types of semiconductor lasers with QW active region such as typical in-plane edge emitting lasers, grating based DFB and DBR lasers, and VCSELs are developed to be applicable in the specific applications, and to the present, most commercial semiconductor lasers are designed with QW active region. Next, a brief investigation of VCSEL and 1.3-mm InGaAsN/GaAs EELDs are given.

1-3-1 VCSELs

Unlike the first and still most common in-plane semiconductor lasers, VCSEL provides a laser emission normal to the plane of the wafer. As shown in Figure 1.15, VCSELs are made by sandwiching an active region between two highly reflective mirrors. The photons generated from the active region, oscillating in the cavity, and finally laser emits normal to the plane of the wafer with a circular beam shape. Unlike an in-plane laser, the resonant cavity of a VCSEL is commonly constructed during the epitaxial growth with a thickness of one or several wavelengths, and its magnitude is two orders smaller than that of an in-plane laser (typical to 250 μm). The mirrors of a VCSEL can be created in a number of ways. The trends include incorporating a sequence of distributed Bragg reflectors directly into the epitaxial growth of the laser structure. The DBR is constructed by two quarter-wave layers with different refractive index. For instance, varying the aluminum composition in AlGaAs material with lattice matching to GaAs allows a range of refractive index change ($\Delta n \sim 0.7$). Alternatively, dielectric (SiO_2, TiO_2, Ta_2O_5) or even metal mirrors can be deposited onto the epitaxial structure. As well as a result of the highly reflective mirrors and the smaller active

region volume, the threshold current of a VCSEL can be ~mA or even smaller. These unique advantages hasten the development of VCSELs being in applications of optical fiber communications, local area networks, laser printing, consumer electronics, optical sensors, barcode scanners, digital displays, spatial light modulators, backplanes and smart pixels, and microscopes [88–91].

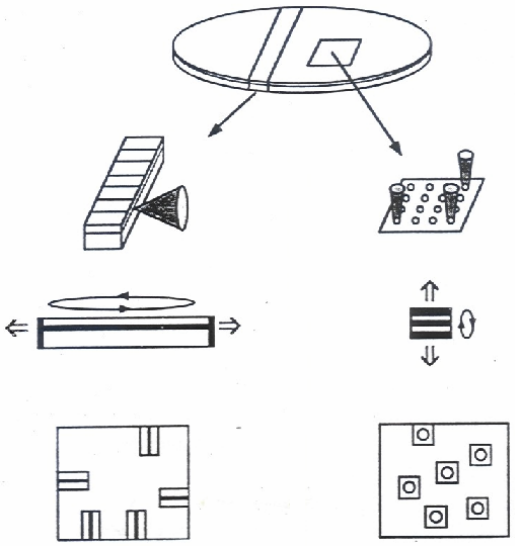

(a) in-plane laser (b) VCSEL

Figure 1.15 Schematic illustrations of (a) an in-plane laser and (b) a VCSEL.

In 1979, the first VCSEL structure was originated by Dr. Iga *et al* [92]. An InGaAsP material was used as active region and laser action occurred at 1180 nm under low temperature pulse operation. A threshold current density of 44 kA/cm^2 was obtained on that time. This is high due to that a large volume of active region, the poor crystal quality and carrier confinement, and the reflectivity of two mirrors, which were made by metallic reflectors, was not so high as to be >99%. So, with an aim to reduce the threshold current of a VCSEL, Ogura *et al*. initiatively used the DBR structure into the epitaxial structure, while the reflectivity of the mirrors can be >99%. The demonstrated VCSEL characteristics showed a reduced threshold current density of 1 kA/cm^2 at room temperature [93]. In 1989, the VCSEL with high reflectivity DBR

mirrors combining the QW design in the resonance cavity was demonstrated by Lee *et al* [94]. The VCSEL could be operated at room temperature continuous wave operation with a threshold current density of 1.8 kA/cm^2. Hereafter, the epitaxial structure of a VCSEL was almost fixed as schematically plotted in Figure 1.16.

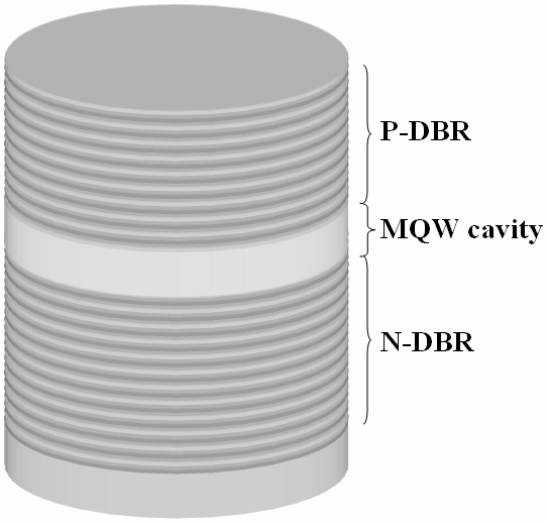

Figure 1.16 A schematic plot of a VCSEL epitaxial structure. The reflectors are formed by DBRs with reflectivity above 99%.

Short cavity characteristics

From the physics of semiconductor lasers, it is well-known that the cavity length is quite sensitive to the laser output characteristics. A laser with large cavity length always has higher threshold current, lower slope efficiency, and temperature insensitivity. As for the lasing mode control, we know that the longitudinal mode separation is equal to $\Delta\lambda = \lambda_0^2/(2n_{eff}L)$, which indicates that a laser with shorter cavity length can be easier to achieve single longitudinal mode operation. A comparison of the cavity mode spectrum distributions of an in-plane laser and a VCSEL is shown in Figure 1.17. Due to the larger cavity length of an in-plane laser, the mode separation is relatively smaller than that of a VCSEL, and it results in that the lasing wavelength shifts to red emission as the gain spectrum shifts caused by the increase of current or device temperature. In contrary, the cavity length of a VCSEL is about two orders less than that of an in-plane laser, and

it is always designed to be one-wavelength-thick. Therefore, it is possible to have single longitudinal mode operation in the range of gain spectrum.

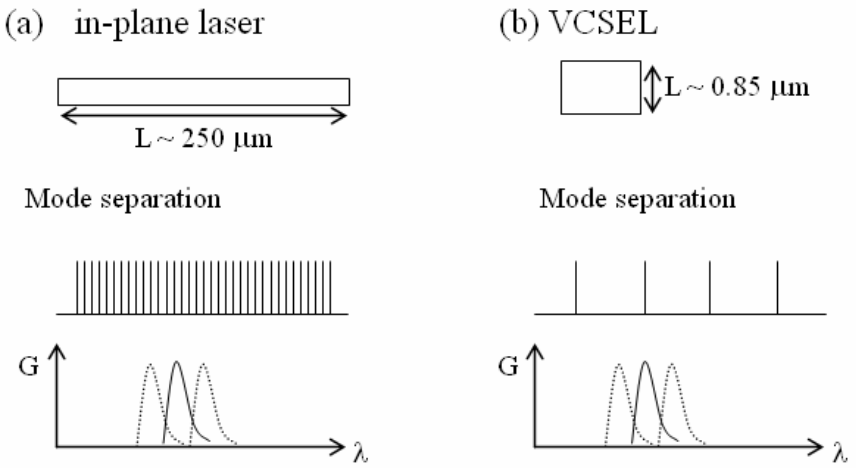

Figure 1.17 Lasing modes of (a) an in-plane laser and (b) a VCSEL change with the shift of gain spectrum.

Gain-cavity detuning

As depicted in Figure 1.17, one can know that a better VCSEL output performance is obtained if the gain spectrum of the active region matches to the cavity mode. This condition only can be obtained in a specific temperature range because the cavity mode changes with temperature at roughly 0.8 Å/ºC while the peak of the gain spectrum shifts at a rate of 3.3 Å/ºC [95]. As illustrated by Choquette *et al*., the gain-cavity detuning dominates the threshold current of a VCSEL in a particular full wafer mapping. As depicted in Figure 1.18, the threshold current of VCSELs located at different position in a wafer was different. This phenomenon can be illustrated in such a way that the optical thickness of a VCSEL cavity is different across a wafer. Since the gain spectrum of the active region is not the key element to affect the VCSELs at different wafer positions, the changes in the threshold current are mainly due to the variant optical thickness of the cavity which make the spectral misalignment between the gain spectrum and the cavity mode [96].

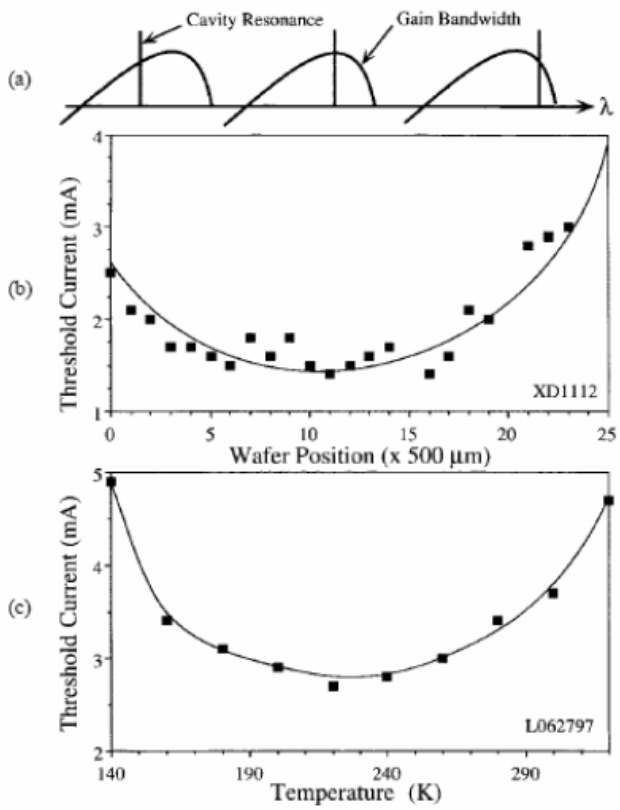

Figure 1.18 (a) Schematic illustration of the spectral misalignment between the cavity mode and the gain spectrum. (b) The VCSEL threshold current dependence on the position across a wafer. (c) The VCSEL threshold current dependence on the device temperature.

In such a way, the VCSEL output performance can be less temperature sensitive as compared to the typical in-plane laser. With a careful design of the gain-cavity detuning in a VCSEL structure, the threshold current of a VCSEL can be stable in a specific temperature range.

Device fabrication varieties

In the processes of fabricating VCSEL devices, there are several main techniques, including mesa etching, transverse confinement of electrical current or optical fields, ohmic contact metal deposition, and dielectric film deposition. Due to the laser light of a VCSEL is in vertical emission, the mesa etching is to isolate and form the shape. Ohmic contact metal deposition facilitates driving current injecting well into the active region with the minimum of electric resistance. The deposition of dielectric film is for

the purpose of passivation. As for the transverse confinement, the shape and the way to confine current and optical field may strongly affect the electrical output performance and the transverse mode pattern. It is undoubted that a well fabrication design of electrical and optical confinement will more enhance the natural characteristics of a VCSEL. Basically, the fabricated VCSEL structure can be divided into four mechanism such as index-guiding, gain-guiding, or hybrid gain/index-guiding. As illustrated in Figure 1.19(a), the simplest method to provide electrical and optical confinement of a VCSEL is the air-post type. By means of wet or chemical etching to form a smaller current injection volume, the current density in the active region becomes higher. As well, since the index difference between the air and the posted semiconductor is larger, a strong transverse confinement of the optical field is achieved. However, there may have diffraction and scattering losses while decreasing the active region diameter. Neither, single-mode operation is not stable in this structure, and high thermal resistance problem may be serious.

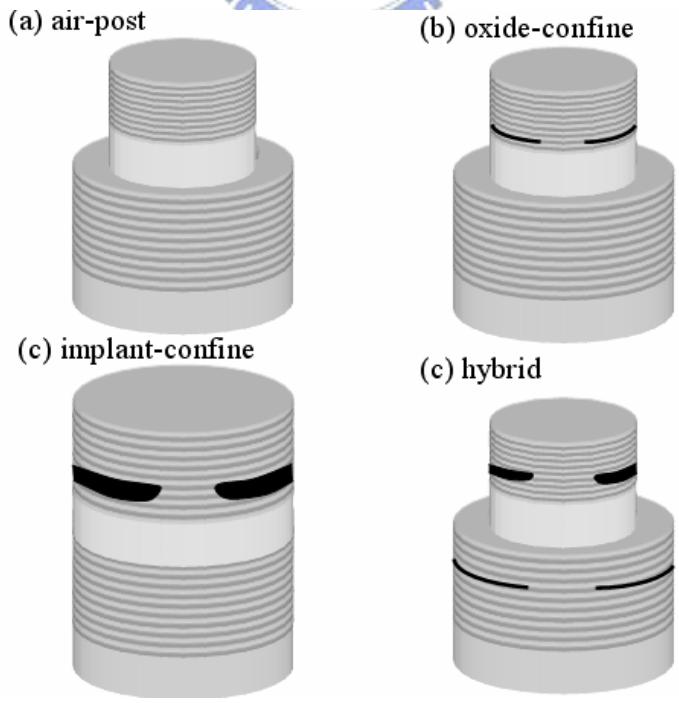

Figure 1.19 Schematic representations of (a) air-post index guide (b) oxide confine index guide (c) implant confine gain guide and (d) hybrid index and gain guide confine VCSELs.

To confine current effectively in a VCSEL, selective oxide confine technique is used to form a smaller current injection region. As shown in Figure 1.19(b), a mesa structure must be formed by etching so as to expose the sidewall of the oxide confine layer. For VCSELs with 850 nm emission or the VCSEL on GaAs substrate, the oxide confine layer is normally to be AlGaAs with high aluminum content (Al=0.98~1.0 typically). An oxide aperture can be obtained by placing the mesa structure into a H_2O/N_2 steam environment at temperature of ~420 ^oC, then the $Al_{0.98\sim1.0}Ga_{0\sim0.02}As$ layer becomes an insulating oxide layer and therefore forming an oxide aperture above the active region. Due to the refractive index of the oxided layer (AlO_x) is relatively lower than that of the surround semiconductor materials, the lateral mode can also be tightly confined by the oxide layer. As well, the oxided layer is insulated, the injected current can be further confined in a smaller area so that the threshold current can be reduced and so as improving the efficiency.

A gain-guiding mechanism can be realized by depositing the ring metal contact directly onto the wafer near the active region to confine the transverse mode. Laser action occurs at the active region where the current injects. Typically, to minimize the current injection region of a VCSEL, an ion implantation technique is used. The ion implantation is that implanting protons or oxygen ions into the p-DBR region forming a high resistance region to block the current without flowing into. As illustrated in Figure 1.19(c), the flow of the injection current can be well confined in the center of VCSEL device, and hence the threshold current can be reduced as compared to the air-post type VCSEL. For this type of VCSEL, the advantages include low threshold current achievement, easy fabrication, and high yield rate. However, the implantation shall prevent the damage of the active region. It is because that an additional optical loss may be induced if the active region is damaged. As for the optical lateral mode confinement, even the current path can be defined by the implanted areas, inherent transverse optical

confinement does not exist in this structure. That means, the transverse mode can always be found owing to the spatial hole burning effect in a gain-guide implanted VCSEL [97].

In a VCSEL, the output power is quite sensitive to the current aperture gain region. Enlarge the current aperture can increase the output power but in term results in the increase of transverse mode numbers. Hence, with an aim to obtain a low threshold current, high output power, and single mode operation VCSEL, hybrid index/gain guide technology is noticed and developed. As shown in Figure 1.19(d), the hybrid index/gain guide oxide/implant VCSEL structure is reported by Young *et al*. The current aperture can therefore be made smaller than the index-guide aperture; therefore a relatively low threshold current can be achieved. Furthermore, the overlap between of fundamental mode and gain spectrum can be kept sufficiently while optical loss of the higher-order modes decreases due to the larger mode spreading profile [98]. Other hybrid index/gain guide structures such as oxide/surface relief [99] and Zn diffusion/surface relief [100] can also have the VCSEL to operate with low threshold current, high output power and single mode.

To date, VCSEL devices have become the standard in free space optical communication and local area networks. These surface emission laser devices possess low divergent angle and circular beam, which lead to simple packaging and low electrical power consumption. The surface emission from the VCSELs also assists the integration of two-dimensional laser array and the facilitation of wafer level testing.

1-4 Historical review of 1.3-μm InGaAsN EELs

As depicted in Figure 1.13, the semiconductor layer plays an important role in the development of optical fiber communications due to the characteristics of coherent laser light emission, pure emission spectrum linewidth, and low divergent angle. Particularly,

semiconductor lasers with an emission wavelength of 1.55 μm are significant due to a relatively lowest attenuation loss in the silica fiber, and in addition, 1.3-μm semiconductor lasers are noticed due to the nearly zero dispersion. Being as the active light source in the optical communication system, the semiconductor lasers are demanded to be less temperature sensitive, low power consumption, high power operation, and high modulation speed. Due to the early and well-developed epitaxy and process techniques, the semiconductor lasers made by InGaAsP/InP material have become the standard active light sources. However, there always exists a major disadvantage in the InGaAsP/InP material system; that is, the conductor band offset ratio ($\Delta E_c/\Delta E_v$) is lower as 0.4/0.6 [101–104]. Even the InGaAsP semiconductor lasers can provide a laser performance with low threshold current and high output power operation, the high temperature dependent laser output characteristics are found poorer as compared to the InGaAs/GaAs semiconductor lasers. It can be realized that the low conduction band offset always indicates a poor carrier confinement in the active region. When the lasers are at high current or high temperature operation, the probability of carrier leakage may increase; therefore, the photon generation rate decreases. To clarify the temperature dependent characteristic of a semiconductor laser, a characteristic temperature (T_0) value, defined by $I_{th} = I_0 \cdot \exp(T/T_0)$, was used. It can be realized that less threshold current variation with elevated device temperature in a semiconductor laser leads to a higher T_0 value, which in other words indicates that the device becomes temperature insensitive. For InGaAsP/InP based semiconductor lasers, the T_0 value is typically in a range of 50–70 K [105]. While other material systems such as InGaAlAs/GaAs and InGaAsN/GaAsN based 1.3-μm semiconductor lasers can have a T_0 value exceeding 100 K. Specifically, the InGaAsN/GaAsN material is preferred due to the large conduction band offset ($\Delta E_c/\Delta E_v = 0.7/0.3$) [106].

InGaAsN material

In 1990, the material of GaAs incorporated with nitrogen was studied by Liu *et al*. It was the first observation of different nitrogen pair complexes in GaAs. The luminescence of excitons bound to nitrogen pairs as well as to isolated nitrogen in GaAs was studied. The bandgap energy of the GaAs incorporated with nitrogen was found decreased and it was though as a result of the inducing a exciton bonding state within the bandgap energy of GaAs [107]. Continued works on the theoretical calculations and growth film analysis were done to investigate the $GaAs_{1-x}N_x$ material, in which the studies showed only a small amount of nitrogen could be incorporated into GaAs [108] and a large bowing parameter was found [108–111]. As shown in Figure 1.20, the bandgap energy of $GaAs_{1-x}N_x$ functioned by nitrogen composition has a bowing parameter as high as 20 eV. Based on Van Vechten's model (solid line), a theoretical calculation also obtains a large bowing parameter, and negative bandgap energy of $GaAs_{1-x}N_x$ alloy is indicated.

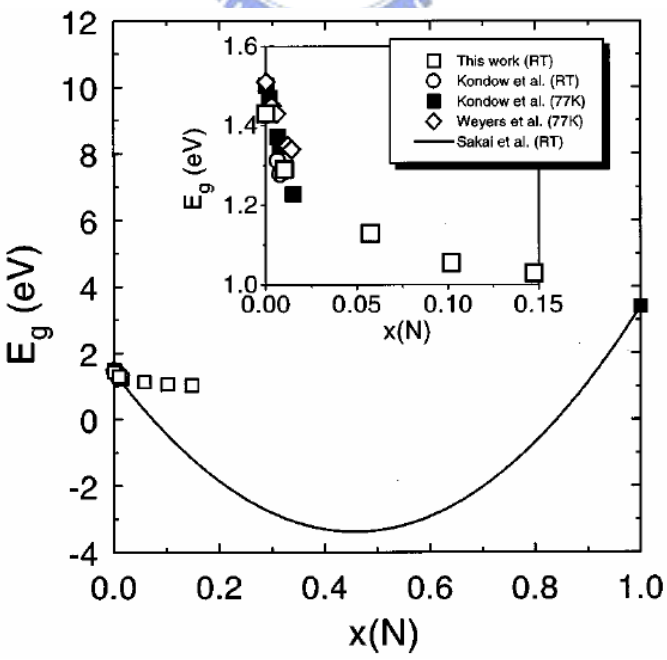

Figure 1.20 Bandgap energy of $GaAs_{1-x}N_x$ as a function of nitrogen composition. As shown the open squares are the experimental data and the solid line is the theoretical calculation.

Theoretically, $GaAs_{1-x}N_x$ material is attractive because it provides a lower bandgap energy, which can emit with a wavelength longer than GaAs characteristic wavelength (0.87 μm). However, the emission wavelength in the experiment when increasing nitrogen composition in the $GaAs_{1-x}N_x$ material seems to be distant from the theoretical trend. By incorporating 14.8% nitrogen into $GaAs_{1-x}N_x$ material, the bandgap energy changes slowly to 1.029 eV (1.205 μm). This phenomenon observed from experiment is suggested due to the variation of bowing parameters with variant nitrogen composition in $GaAs_{1-x}N_x$ material. Nevertheless, $GaAs_{1-x}N_x$ material is preferred to be an active region material due to the large bowing parameters. In 1996, $GaAs_{1-x}N_x$ material has again received great attraction when Kondow *et al*. successfully create the incorporation of indium into $GaAs_{1-x}N_x$ material. For long wavelength emission, InGaAsN material is much preferred because it can be grown on the GaAs substrate, a type I band lineup, and thus very deep quantum well structures can be fabricated.

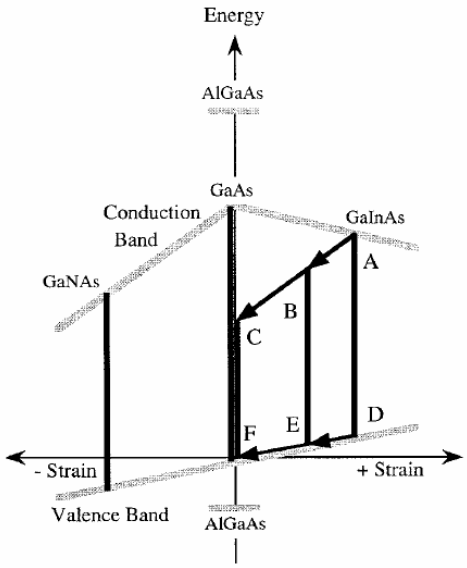

Figure 1.21 A schematic diagram of the band lineups for GaAsN, InGaAs, and InGaAsN materials.

As shown in Figure 1.21, GaAs material is located at center with bandgap energy of 1.42 eV and zero lattice mismatch as a template. Increasing In composition in InGaAs material results in a compressive strain, while increasing the nitrogen

composition in $GaAs_{1-x}N_x$ results in a tensile strain. If a small amount of nitrogen is added into InGaAs to form InGaAsN, the conduction and valence bands will move from A to B and from D to E, respectively. At the alloy composition in which the InGaAsN is lattice matched, the conduction and valence bands will be located at C and F. Therefore, a type I band lineup is easily achieved, which indicates that choosing InGaAsN as active region material can provide a better confinement of carriers.

Growth of InGaAsN

In early development of growing InGaAsN material, the most challenge has been how to achieve high quality quantum well structure. No one had grown InGaAsN until Kondow *et al*. did. In 1997, the key to obtain large nitrogen composition in $GaAs_{1-x}N_x$ material is the use of plasma-activated nitrogen source. In spite of M. Sato *et al*. developing a unique ultra-low-pressure MOCVD apparatus that utilized dimethylhydrazine (DMHy) as the nitrogen precursor, Kondow *et al*. had chosen the use of a commercial nitrogen radical cell that could be attached to a conventional gas-source molecular beam epitaxy (GS-MBE) system [113]. Both two ways were the sole method for InGaAsN growth in the late 1990s. The GS-MBE system used by Kondow *et al*. is schematically plotted in Figure 1.22. Metal-Ga, metal-In, arsine gas, and nitrogen gas were used as precursors. It is an advantage that using GS-MBE to grow InGaAsN produces more reactive-nitrogen and fewer reactions between the sources. By using GS-MBE to grow, the surface morphology of InGaAsN was mirror-likely smooth. After X-ray diffraction determination, the quantum well was found to be $In_{0.3}Ga_{0.7}As_{0.996}N_{0.004}$, and an emission wavelength of 1.17 μm was obtained for the first time.

Afterward the first demonstration of InGaAsN QW and the fabrication of InGaAsN laser in 1997, the research have been focused on the achievement of high-performance long wavelength InGaAsN/GaAs semiconductor lasers. Specifically, extending the

emission wavelength by increasing indium or nitrogen compositions in the InGaAsN quantum well but simultaneously keeping a feasible film quality is the most crucial issue. As a result of the InGaAsN is a solid solution with a large size mismatch of constituents on the group-V sublattice, this material brings a number of unusual optical properties, such as a large bandgap bowing as mentioned previously, a large Stokes shift between absorption and emission [113], and a blue-shift of the emission with post-growth annealing. Nitrogen incorporation into InGaAs beyond about 1% causes strong quenching of the luminescence and a broadening of the luminescence linewidth. Even post-growth annealing can improve the luminescence significantly and improve the optical properties but leads to a blue-shift of the PL peak [114–116]. The blue-shift of the PL on annealing is found due to the homogenization of the indium composition and to diffusion of nitrogen out of the active region [117].

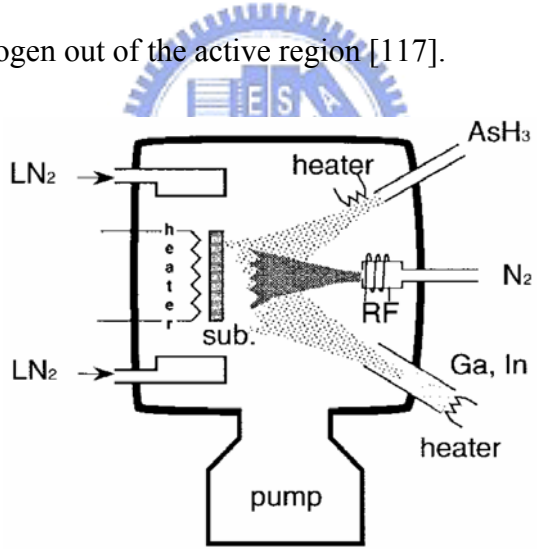

Figure 1.22 A schematic diagram of GS-MBE growth apparatus.

To date, a 1.55-μm InGaAsN quantum well with a GaAsN or an InGaAsN barrier and space layer is presented. By increasing nitrogen composition in GaAsN barrier and space layer instead of increasing nitrogen composition in InGaAsN quantum well, a stronger improvement of photoluminescence efficiency is observed [118]. As a result, by means of successful demonstration of high-quality quantum well structures, long wavelength InGaAsN/GaAsN semiconductor lasers with high output efficiency can be

fabricated.

InGaAsN/GaAs semiconductor laser

As illustrated in the beginning of this subsection, 1.3-μm or 1.55-μm semiconductor lasers are used as light sources to minimize the transmission loss at the silica optical fiber window in optical fiber communication system. These diodes consist mostly of InGaAsP alloy semiconductors formed on an InP substrate; however, their lasing characteristics remain unsatisfactory at high temperature operation. Compared to a typical InGaAs/GaAs semiconductor laser with 980 nm laser emission, which has a T_0 value of 150 K, the T_0 value of InGaAsP/InP semiconductor laser is much low as 60 K. Therefore, it always requires thermoelectric cooler in most practical uses. In order to drastically improve the high temperature characteristics of long wavelength lasers, the InGaAsN material is proposed due to a large conduction band offset value. Based on the calculation of T_0 value as a function of ΔE_c value with thermoionic emission model by Suemune *et al*., while the quasi-Fermi levels for electrons are assumed to be 50 and 70 meV at 300 and 360 K, a maximally achievable T_0 value of 180 K is predicted with a ΔE_c value over 300 meV, which completely suppress electrons from overflowing [119].

Recently, substantial works on InGaAsN/GaAs semiconductor lasers have showed an improvement in the T_0 values of 70–110 K over those achievable by the conventional InP technology under CW mode operation [120–124]. Improvement of lasing characteristics and high-temperature operation performance by anti-reflection–high-reflection facet coating that obtains a CW output power of 210 mW [125], and fabrication of laser chips that are bonded p-side-down onto copper heat-sink with pulsed anodic oxidation (PAO) technology, which can operate in CW mode up to 130 °C with a high T_0 value of 138 K [126] by Qu *et al*. is also found. In the case of laser structure design for improving lasing characteristics or obtaining better T_0 value,

Tansu *et al*. utilized tensile-strain $GaAs_{0.85}P_{0.15}$ layers on both sides of the InGaAsN/GaAs active region to reduce the strain in quantum wells for achieving better crystal quality [127–129]. Even the relatively low and unexpected low T_0 values when compared to the theoretical prediction are found due to the large Auger recombination and nitrogen penalty [130, 131], InGaAsN/GaAsN based design in the active region is still preferred in the development of long wavelength semiconductor lasers.

References

[1] Govind P. Agrawal, and Niloy K. Dutta, "*Semiconductor Lasers*", 2nd, Van Nostrand Reinhold, New York, 1993.

[2] R. N. Hall, G. E. Fenner, J. D. Kingsley, T. J. Soltys, and R. O. Carlson, "Coherent light emission from GaAs junctions," *Phys. Rev. Lett.*, vol. 9, pp. 366368, 1962.

[3] M. I. Nathan, W. P. Dumke, G. Burns, F. H. Dill, Jr., and G. Lasher, "Stimulated emission of radiation GaAs p-n junctions," *Appl. Phys. Lett.*, vol. 1, pp. 62–64, 1962.

[4] T. M. Quist, R. H. Rediker, R. J. Keyes, W. E. Krag, B. Lax, A. L. McWhorter, and H. J. Zeiger, "Semiconductor MASER of GaAs," *Appl. Phys. Lett.*, vol. 1, pp. 91–92, 1962.

[5] N. Holonyak, Jr., and S. F. Bevacqua, "Coherent (visible) light emission from $Ga(As_{1-x}P_x)$ junctions," *Appl. Phys. Lett.*, vol. 1, pp. 82–83, 1962.

[6] http://www.crosslight.com.tw/

[7] J. I. Pankove, and T. D. Moustakas, "*Gallium Nitride (GaN) I - Semiconductors and Semimetals Volume 50*," Academic Press, San Diego, California, USA (1998)

[8] S. D. Lester, F. A. Ponce, M. G. Craford, and D. A. Steigerwald, "High dislocation densities in high efficiency GaN-based light-emitting diodes," *Appl. Phys. Lett.*, vol. 66, pp. 1249–1251, 1995.

[9] S. Chichibu, T. Azuhata, T. Sota, and S. Nakamura, "Spontaneous emission of localized excitons in InGaN single and multiquantum well structure," *Appl. Phys. Lett.*, vol. 69, pp. 4188–4190, 1996.

[10] S. Yoshida, S. Misawa, and S. Gonda, "Improvements on the electric and luminescent properties of reactive molecular beam epitaxially grown GaN films by using AlN-coated sapphire substrates," *Appl. Phys. Lett.*, vol. 42, pp. 427–429, 1983.

[11] J. J. Hsieh, J. A. Rossi, and J. P. Donnelly, "Room-temperature cw operation of GaInAsP/InP double-heterostructure diode lasers emitting at 1.1 μm " *Appl. Phys. Lett.*, vol. 28, pp. 709–711, 1976.

[12] H. Amano, N. Sawaki, I. Akasaki, Y. Toyoda, "Metalorganic vapor phase epitaxial growth of a high quality GaN film using an AlN buffer layer," *Appl. Phys. Lett.*, vol. 48, pp. 353–355, 1986.

[13] S. Nakamura, Y. Harada, and M. Seno, "Novel metalorganic chemical vapor deposition system for GaN growth," *Appl. Phys. Lett.*, vol. 58, pp. 2021–2023, 1991.

[14] H. Amano, M. Kito, K. Hiramatsu, and I. Akasaki, "P-type conduction in Mg-doped GaN treated with low-energy beam irradiation (LEEBI)," *Jpn. J. Appl.*

Phys., vol. 28, p. L2112–L2114, 1989.

[15] S. Nakamura, T. Mukai, M. Senoh, and N. Iwasa, "Thermal annealing effects on p-type Mg-doped GaN films," *Jpn. J. Appl. Phys*., vol. 31, pp. L139–L142, 1992.

[16] G. B. Stringfellow, and M. G. Craford, "*High Brightness Light Emitting Diodes: Semiconductors and Semimetals Volume 48*," Academic Press, San Diego, California, USA (1997).

[17] S. Nakamura, "InGaN multiquantum-well-structure laser diodes with GaN-AlGaN modulation-doped strain-layer," *IEEE J. Sel. Top. Quantum. Electron.*, vol. 4, pp. 483–489, 1998.

[18] J. Piprek, "Nitride Semiconductor Devices," WILEY-VCH Verlag GmbH & Co. KgaA, Weinheim (2007).

[19] G. O. Mueller and R. Mueller-Mach, "*Set The Pace in White Space–White LEDs for illumination and Backlighting*," *Proceedings of Intertech Phosphor Global Summit*, San Diago, 2005.

[20] M. Kurata, "*Numerical Analysis for Semiconductor Devices*," D.C. Health & Company, Lexington Massachusetts, 1982.

[21] F. Bernardini, V. Fiorentini, and D. Vanderbilt, "Spontaneous polarization and piezoelectric constants of III-V nitrides," *Phys. Rev. B*, vol. 56, pp. R10024–R10027, 1997.

[22] S. L. Chuang and C. S. Chang, "A band-structure model of strained quantum-well wurtzite semiconductors," *Semicond. Sci. Technol*., vol. 12, pp. 252–263, 1997.

[23] S. L. Chuang and C. S. Chang, "k·p method for strained wurtzite semiconductors," *Phys. Rev. B*, vol. 54, pp. 2491–2504, 1996.

[24] S. L. Chuang and C. S. Chang, "Effective-mass Hamiltonian for strained wurtzite GaN and analytical solutions," *Appl. Phys. Lett.*, vol. 68, pp. 1657–1659, 1996.

[25] Y. P. Varshni, "Temperature dependence of the energy gap in semiconductors," *Physica*, vol. 34, pp. 149–154, 1967.

[26] R. Dingle, D. D. Sell, S. E. Stokowski, and M. Ilegems, "Absorption, reflectance, and luminescence of GaN epitaxial layers," *Phys. Rev. B*, vol. 4, pp. 1211–1218, 1971.

[27] M. Ilegems, R. Dingle, and R. A. Logan, "Luminescence of Zn-and Cd-doped GaN," *J. Appl. Phys.*, vol. 43, pp. 3797–3800, 1972.

[28] O. Lagerstedt and B. Monemar, "Luminescence in epitaxial GaN:Cd," *J. Appl. Phys.*, vol. 45, pp. 2266–2272, 1974.

[29] B. Monemar, "Fundamental energy gap of GaN from photoluminescence excitation spectra," *Phys. Rev. B*, vol. 10, pp. 676–681, 1974.

[30] B. Monemar, J. P. Bergman, I. A. Buyanova, W. Li, H. Amano, and I. Akasaki, *MRS J. Nitride Semicond. Res.*, vol. 1, pp. 2, 1996.

[31] G. D. Chen, M. Smith, J. Y. Lin, H. X. Jiang, S. H. Wei, M. A. Khan, and C. J. Sun, "Fundamrntal optical transitions in GaN," *Appl. Phys. Lett.*, vol. 68, pp. 2784–2786, 1996.

[32] C. Merz, M. Kunzer, U. Kaufmann, I. Akasaki, and H. Amano, "Free and bound excitons in thin wurtzite GaN layers on sappire," *Semicond. Sci. Technol.*, vol. 11, pp. 712–716, 1996.

[33] D. C. Reynolds, D. C. Look, W. Kim, O. Aktas, A. Botchkarev, A. Salvador, H. Morkoc, and D. N. Talwar, "Ground and excited state exciton spectra from GaN grown by molecular-beam epitaxy," *J. Appl. Phys.*, vol. 80, pp. 594–596, 1996.

[34] J. F. Muth, J. H. Lee, I. K. Shmagin, R. M. Kolbas, H. C. Casey, Jr., B. P. Keller, U. K. Mishra, and S. P. DenBaars, "Absorption coefficient, energy gap, exciton binding energy, and recombination lifetime of GaN obtained from transmission measurements," *Appl. Phys. Lett*., vol. 71, pp. 2572–2574, 1997.

[35] I. Vurgaftman and J. R. Meyer, "Band parameters for nitrogen-containing semiconductors," *J. Appl. Phys.*, vol. 94, pp. 3675–3696, 2003.

[36] K. Osamura, S. Naka, and Y. Murakami, "Preparation and optical properties of $Ga_{1-x}In_xN$ thin film," *J. Appl. Phys*., vol. 46, pp. 3432–3437, 1975.

[37] N. Puychevrier and M. Menoret, "Synthesis of III-V semiconductor nitrides by reactive cathodic sputtering," *Thin Solid Films*, vol. 36, pp. 141–145, 1976.

[38] V. A. Tyagai, A. M. Evstigneev, A. N. Krasiko, A. F. Andreeva, and V. Ya. Malakhov, *Sov. Phys. Semicond.*, vol. 11, pp. 1257, 1977.

[39] T. L. Tansley and C. P. Foley, "Optical band gap of indium nitride," *J. Appl. Phys.*, vol. 59, pp. 3241–3244, 1986.

[40] K. L. Westra and M. J. Brett, "Near IR optical properties of sputtered InN films," *Thin Solid Films*, vol. 192, pp. 227–234, 1990.

[41] Q. Guo and A. Yoshida, "Temperature dependence of band gap change in InN and AlN," *Jpn. J. Appl. Phys*., vol. 33, pp. 2453–2456, 1994.

[42] B. R. Nag, "Comment on "band gap of InN and In-rich $In_xGa_{1-x}N$ alloys ($0.36<x<1$)"," *Phys. Status Solidi (b)*, vol. 232, pp. R8–R9, 2002.

[43] T. Matsuoka, H. Okamoto, M. Nakao, H. Harima, and E. Kurimoto, "Optical bandgap energy of wurtzite InN," *Appl. Phys. Lett.*, vol. 81, pp. 1246–1248, 2002.

[44] S. Nakamura M. Senoh, and T. Mukai, "High-power InGaN/GaN double-heterostructure violet light emitting diodes," *Appl. Phys. Lett.*, vol. 62, pp. 2390–2392, 1993.

[45] S. Nakamura, T. Mukai, and M. Senoh, "High-brightness InGaN/AlGaN double-heterostructure blue-green-light-emitting diodes," *J. Appl. Phys.*, vol. 76, pp. 8189–8191, 1994.

[46] S. Nakamura, M. Senoh, N. Iwasa, and S. Nagahama, "High-power InGaN

single-quantum-well-structure blue and violet light-emitting diodes," *Appl. Phys. Lett.*, vol. 67, pp. 1868–1870, 1995.

[47] K. Osamura, K. Nakajima, and Y. Murakami, "Fundamental absorption edge in GaN, InN and alloys," *Solid State Commun.*, vol. 11, pp. 617–621, 1972.

[48] A. F. Wright and J. A. Nelson, "Band parameters for zinc-blende $Al_{1-x}Ga_xN$ and $Ga_{1-x}In_xN$," *Appl. Phys. Lett.*, vol. 66, pp. 3051–3053, 1995.

[49] K. Kassali and N. Bouarissa, "Pseudopotential calculations of electric properties of $Ga_{1-x}In_xN$ alloys with zinc-blende structure," *Sol. State Electron.*, vol. 44, pp. 501–507, 2000.

[50] O. Brandt, J. R. Millhauser, B. Yang, H. Yang, and K. H. Ploog, "Optical properties of cubic GaN and (In,Ga)N," *Physica E*, vol. 2, pp. 532–538, 1998.

[51] M. Ferhat, J. Furthmüller, and F. Bechstedt, "Gap bowing and Stokes shift in $In_xGa_{1-x}N$ alloys: First-principles studies," *Appl. Phys. Lett.*, vol. 80, pp. 1394–1396, 2002.

[52] M. Ferhat and F. Bechstedt, "First-principles calculations of gap bowing in $In_xGa_{1-x}N$ and $In_xAl_{1-x}N$ alloys: Relation to structural and thermodynamic properties," *Phys. Rev. B*, vol. 65, pp. 075213, 2002.

[53] S. Yoshida, S. Misawa, and S. Gonda, "Properties of $Al_xGa_{1-x}N$ films prepared by reactive molecular beam epitaxy," *J. Appl. Phys.*, vol. 53, pp. 6844–6848, 1982.

[54] J. Hagen, R. D. Metcalfe, D. Wickenden, and W. Clark, *J. Phys. C*, vol. 11, pp. L143–L146, 1978.

[55] Y. Kiode, H. Itoh, M. R. H. Khan, K. Hiramatu, N. Sawaki, and I. Akasaki, "Energy band-gap bowing parameter in an $Al_xGa_{1-x}N$ alloy," *J. Appl. Phys.*, vol. 61, pp. 4540–4543, 1987.

[56] Y. -K. Kuo and W. W. Lin, "Band-gap bowing parameter of the $Al_xGa_{1-x}N$ derived from theoretical simulation," *Jpn. J. Appl. Phys.*, vol. 41, pp. 73–74, 2002.

[57] H. Jiang, G. Y. Zhao, H. Ishikawa, T. Egawa, T. Jimbo, and M. Umeno, "Determination of exciton transition energy and bowing parameter of AlGaN alloys in AlGaN/GaN heterostructure by means of reflectance measurement," *J. Appl. Phys.*, vol. 89, pp. 1046–1052, 2001.

[58] J. Wagner, H. Obloh, M. Kunzer, K. Köhler, and B. Kohs, "Dielectric function spectra of GaN, AlGaN, and GaN/AlGaN heterostructures," *J. Appl. Phys.*, vol. 89, pp. 2779–2785, 2001.

[59] Q. Zhou, M. O. Manasreh, M. Pophristic, S. Guo, and I. T. Ferguson, "Observation of nitrogen vacancy in proton-irradiated $Al_xGa_{1-x}N$," Appl. Phys. Lett., vol. 79, pp. 2901–2903, 2001.

[60] O. Katz, B. Meyler, U. Tisch, and J. Salzman, "Determination of band-gap bowing for $Al_xGa_{1-x}N$ alloys," *Phys. Status Solidi (a)*, vol. 188, pp. 789–792, 2001.

[61] M. Asif Khan, J. W. Yang, G. Simin, R. Gaska, M. S. Shur, Hans-Conrad zur Loye, G. Tamulaitis, A. Zukauskas, David J. Smith, D. Chandrasekhar, and R Bicknell-Tassius, "Lattice and energy band engineering in AlInGaN/GaN heterostructures," Appl. Phys. Lett., vol. 76, pp. 1611–1613, 2000.

[62] I. Vurgaftman, J. R. Meyer, and L. R. Ram-Mohan, "Band parameters for III-V compound semiconductors and their alloys," *J. Appl. Phys*., vol. 89, pp. 5815–5875, 2001.

[63] V. Fiorentini, F. Bernardini, and O. Ambacher, "Evidence of nonlinear macroscopic polarization in III-V nitride alloy heterostructures," *Appl. Phys. Lett*., vol. 80, pp. 1204–1206, 2002.

[64] T. F. Kuech, R. T. Collins, D. L. Smith, and C. Maihiot, "Field-effect transistor structure based on strain-induced polarization charges," *J. Appl. Phys.*, vol. 67, pp. 2650–2652 ,1990.

[65] G. Martin, S. Strite, A. Botchkarev, A. Agarwal, A. Rockett, H. Morkov, W. R. L. Lambrecht, and B. Segall, "Valence-band discontinuity between GaN and AlN measured by x-ray photoemission spectroscopy," *Appl. Phys. Lett.*, vol. 65, pp. 610–612, 1994.

[66] G. Martin, A. Botchkarev, A. Rockett, and H. Morkov, "Valence-band discontinuities of wurtzite GaN, AlN, and InN heterojunctions measured by x-ray photoemission spectroscopy," *Appl. Phys. Lett.*, vol. 68, pp. 2541–2543, 1996.

[67] J. Baur, K. Maier, M. Kunzer, U. Kaufmann, and J. Schneider, " Determination of the GaN/AlN band offset via the (-/0) acceptor level of iron," *Appl. Phys. Lett.*, vol. 65, pp. 2211–2213, 1994.

[68] J. R. Waldrop, and R. W. Grant, "Measurement of AlN/GaN (0001) heterojunction band offsets by x-ray photoemission spectroscopy," *Appl. Phys. Lett.*, vol. 68, pp. 2879–2881, 1996.

[69] S. -H. Wei, and A. Zunger, " Valence band splittings and band offsets of AlN, GaN, and InN," *Appl. Phys. Lett.*, vol. 69, pp. 2719–2721, 1996.

[70] S. -H. Wei, and A. Zunger, " Calculated natural band offsets of all II–VI and III–V semiconductors: Chemical trends and the role of cation *d* orbitals," *Appl. Phys. Lett.*, vol. 72, pp. 2011–2013, 1998.

[71] E. F. Schubert, Y. -H. Wang, A. Y. Cho, L. -W. Tu, and G. J. Zydzik, "Resonant cavity light-enitting diode," *Appl. Phys. Lett.*, vol. 60, no. 8, pp. 921–923, 1992.

[72] E. Fred Schubert, "*Light-Emitting Diodes*," 2nd Cambridge New York: Cambridge University Press, 2006, ch 15.

[73] T. Ishigure, M. Satoh, O. Takanashi, E. Nihei, T. Nyu, S. Yamazaki, and Y. Koike, "Formation of the refractive index profile in the graded index polymer optical fiber for gigabit data transmission," *J. Lightw. Technol.*, vol. 15, no. 11, pp. 2095–2100,

1997.

[74] H. Kressel, and H. Nelson, *RCA Rev.*, vol. 30, pp. 106, 1969.

[75] I. Hayashi, M. B. Panish, and P. W. Foy, "A low-threshold room-temperature injection laser," *IEEE J. Quantum Electron.*, vol. 5, pp. 211–212, 1969.

[76] Zh. I. Alferov, V. M. Andreev, E. L. Portnoi, and M. K. Trukan, *Sov. Phys. Semicond.*, vol. 3, pp. 1107, 1970.

[77] A. P. Bogatov, L. M. Dolginov, P. G. Eliseev, M.G. Mil'vidskii, B. N. Sverdlov, and E. G. Shevchenko, *Sov. Phys. Semicond.*, vol. 9, pp. 1282, 1975.

[78] P. D. Wright, J. J. Coleman, N. Holonyak, Jr., M. J. Ludowise, and G. E. Stillman, "Homogeneous or inhomogeneous line broadening in a semiconductor laser: Observations on $In_{1-x}Ga_xP_{1-z}As_z$ double heterojunctions in an external grating cavity," *Appl. Phys. Lett.*, vol. 28, pp. 709–711, 1976.

[79] K. Oe, S. Ando, and K. Sugiyama, "1.3 μm CW operation of GaInAsP/InP DH diode lasers at room temperature," *Jpn. J. Appl. Phys.*, vol. 16, pp. 1273–1274, 1977.

[80] M. Horiguchi, and H. Osani, "Spectral losses of low-OH-content optical fibers," *Electron. Lett.*, vol. 12, pp. 310–312, 1976.

[81] T. Suzuki, I. Hino, A. Gomyo, and K. Nishida, "MOCVD-grown $Al_{0.5}In_{0.5}P$-$Ga_{0.5}In_{0.5}P$ double heterostructure lasers optically pumped at 90 K," *Jpn. J. Appl. Phys.*, vol. 21, pp. L731–L733, 1982.

[82] I. Hino, A. Gomyo, K. Kobayashi, T. Suzuki, and K. Nishida, "Room-temperature pulsed operation of AlGaInP/GaInP/AlGaInP double heterostructure visible light laser diodes grown by metalorganic chemical vapor deposition," *Appl. Phys. Lett.*, vol. 43, pp.987–989, 1983.

[83] H. Asahi, Y. Kawamura, and H. Nagai, "Molecular beam epitaxial growth of InGaAlP visible laser diodes operating at 0.66-0.68 μm at room temperature," *J. Appl. Phys.*, vol. 54, pp.6958–6964, 1983.

[84] D. C. Tran, K. H. Levin, C. F. Fisher, M. J. Burk, and G. H. S. Jun, "0.66 μm room-temperature operation of InGaAlP DH laser diodes grown by MBE," *Electron. Lett.*, vol. 19, pp.163–164, 1983.

[85] M. Ikeda, Y. Mori, H. Sato, K. Kaneko, and N. Watanabe, "Room-temperature continuous-wave operation of an AlGaInP double heterostructure laser grown by atmospheric pressure metalorganic chemical vapor deposition," *Appl. Phys. Lett.*, vol. 47, pp. 1027–1028, 1985.

[86] K. Kobayashi, S. Kawata, A. Gomyo, I. Hino, and T. Suzuki, "Room-temperature cw operation of AlGaInP double-heterostructure visible lasers," *Electron. Lett.*, vol. 21, pp. 931–932, 1985.

[87] M. Ishikawa, Y. Ohba, H. Sugawara, M. Yamamoto and T. Nakanisi,

"Room-temperature cw operation of InGaP/InGaAlP visible light laser diodes on GaAs substrates grown by metalorganic chemical vapor deposition," *Appl. Phys. Lett*., vol. 48, pp. 207–208, 1986.

[88] J. A. Hudging, S. F. Lim, G. S. Li, W. Yuen, K. Y. Lau, and C. J. Chang-Hasnain, "Compact, integrated optical disk readout head using a novel bistable vertical cavity surface emitting lasers," *IEEE Photon. Technol. Lett.*, vol. 11, no. 2, pp. 245–247. 1999.

[89] J. Geske, V. Jayaraman, T. Goodwin, M. Culick, M. MacDougal, T. Goodmough, D. Welch, and J. Bower, "2.5 Gb/s transmission over 50 Km with a 1.3 μm vertical cavity surface emitting laser," *IEEE Photon. Technol. Lett.*, vol. 12, no. 12, pp. 1707–1709, 2000.

[90] H. Kosaka, "Smart integration and packaging of 2D VCSEL's of high speed parallel links," *IEEE J. Select. Topic. Quantum Electron.*, vol. 5, no. 2, pp. 184–192, 1999.

[91] K. Kasahara, "VSTEP based smart pixels," *IEEE J. Quantum Electron.*, vol. 29, no. 2, pp. 757–768, 1993.

[92] H. Soda, K. Iga, and Y. Suematsu, "GaInAs/InP surface emitting injection lasers," *Jpn. J. Appl. Phys.*, vol. 18, pp. 2329–2330, 1979.

[93] M. Ogura, W. Hsin, M.-C. Wu, S. Wang, J. R. Whinnery, S. C. Wang, and J. J. Yang, "Surface-emitting laser diode with vertical GaAs/GaAlAs quarter-wavelength multilayer and lateral buried heterostructure," *Appl. Phys. Lett.*, vol. 51, pp. 1655−1657, 1987.

[94] Y. H. Lee, J. L. Jewell, A. Scherer, S. L. Mc. Call, J. P. Harbison, and L. T. Florez, "Room-temperature continuous-wave vertical cavity single-quantum-well microlaser diodes," *Electron. Lett.*, vol. 25, pp. 1377−1378, 1989.

[95] A. Cho, "Film deposition by molecular beam techniques," *J. Vac. Sci. Tech.*, vol. 8, pp. S31−S38, 1971.

[96] G. Hasnain, K. Tai, L. Yang, Y. H. Wang, R. J. Fischer, J. D. Wynn, B. Weir, N. K. Dutta, and A. Y. Cho, "Performance of gain-guided surface emitting lasers with semiconductor distributed Bragg reflectors," *IEEE J. Quantum Electron.*, vol. 27, pp. 1377−1385, 1991.

[97] D. Vakhshoori, J. D. Wynn, G. J. Aydzik, R. E. Leibengnth, M. T. Asom, K. Kojima, and R. A. Morgan, "Top-surface emittin g lasers with 1.9 V threshold voltage and the effect of spatial hole burning on their transverse mode operation and efficiencies," *Appl. Phys. Lett.*, vol. 62, pp. 1448−1450, 1993.

[98] E. W. Young, K. D. Choquette, S. L. Chuang, K. M. Geib, A. J. Fischer, and A. A. Allerman, "Single-transverse-mode vertical-cavity lasers under continuous and pulsed operation," *IEEE Photon. Technol. Lett.*, vol. 13, pp. 927–929, 2001.

[99] A. Haglund, J. S. Gustavsson, P. Modh, and A. Larsson, “Dynamic mode stability analysis of surface relief VCSELs under strong RF modulation,” *IEEE Photon. Technol. Lett.*, vol. 17, pp. 1602–1604, 2005.

[100] J. W. Shi, C. H. Jiang, K. M. Chen, T. J. Hung, and Y. J. Yang,“Vertical-cavity surface-emitting lasers (VCSELs) with high-power and single-spot far-field distributions at 850-nm waveelgnth by use of petal-shaped light-emitting apertures,” IEEE Photon. Technol. Lett., vol. 18, pp. 481–483, 2006.

[101] J. C. L. Yong, J. M. Rorison, M. Othman, H. D. Dawson, and K. A. Williams, “Simulation of gain and modulation bandwidths of 1300 nm RWG InGaAsN lasers,” *IEE Proc.-Optoelectron.*, vol. 150, pp. 80−82, 2003.

[102] C. -E. Zah, R. Bhat, B. N. Pathak, F. Favire, W. Lin, M. C. Wang, N. C. Andreadakis, D. M. Hwang, M. A. Koza, T. -P. Lee, Z. Wang, D. Darby, D. Flanders, and J. J. Hsieh, “High-performance uncooled 1.3-μm $Al_xGa_yIn_{1-x-y}As$/InP strained-layer quantum-well lasers for subscriber loop applications,” *IEEE J. Quantum Electron.*, vol. 30, pp. 511−523, 1994.

[103] T. Ishikawa, T. Higashi, T. Uchida, T. Yamamoto, T. Fujii, H. Shoji, M. Kobayashi, and H. Soda, “Well-thickness dependence of high-temperature characteristics in 1.3-μm AlGaInAs−InP strained-multiple-quantum-well lasers,” *IEEE Photon. Technol. Lett.*, vol. 12, pp. 1703−1705, 1998.

[104] J. Minch, S. H. Park, T. Keating, and S. L. Chuang, “Theory and experiment of $In_{1-x}Ga_xAs_yP_{1-y}$ and $In_{1-x-y}Ga_xAl_yAs$ long-wavelength strained quantum-well lasers,” *IEEE J. Quantum Electron.*, vol. 35, pp. 771−782, 1999.

[105] M. Kondow, K. Uomi, A. Niwa, T. Kitatani, S. Watahiki, and Y. Yazawa, “GaInNAs: a novel material for long-wavelength-range laser diodes with excellent high-temperature performance,” *Jpn. J. Appl. Phys.*, vol. 35, pp. 1273−1275, 1996.

[106] L. Bellaiche, S.-H. Wei, and A. Zunger, “Localization and percolation in semiconductor alloys: GaAsN vs GaAsP,” *Phys. Rev. B*, vol. 54, pp. 17568–17576, 1996.

[107] X. Liu, M.-E. Pìstol, L. Samuelson, S. Schwetlick, and W. Seifert, “Nitrogen pair luminescence in GaAs,” *Appl. Phys. Lett.*, vol. 56, pp. 1451−1453, 1990.

[108] S. Sakai, Y. Ueta, and Y. Terauchi, “Band gap energy and band lineup of III-V alloy semiconductors incorporating nitrogen and boron,” *Jpn. J. Appl. Phys.*, vol. 32, pp. 4413−4417, 1993.

[109] S.-H. Wei and A. Zunger, “Giant and composition-dependent optical bowing coefficient in GaAsN alloys,” *Phys. Rev. Lett.*, vol. 76, pp. 664−667, 1996.

[110] W. G. Bi and C. W. Tu, “Bowing parameter of the band-gap energy of GaN_xAs_{1-x},” *Appl. Phys. Lett.*, vol. 70, pp. 1608−1610, 1997.

[111] J. D. Perkins, A. Mascarenhas, Y. Zhang, J. F. Geisz, D. J. Friedman, J. M. Olson,

and S. R. Kurtz, “Nitrogen-activated transitions, level repulsion, and band gap reduction in $GaAs_{1-x}N_x$ with $x < 0.03$,” *Phys. Rev. Lett.*, vol. 82, pp. 3312−3315, 1999.

[112] M. Kondow, T. Kitatani, S. Nakatsuka, Michael C. Larson, K. Nakahara, Y. Yazawa, M. Okai, and K. Uomi, “HaInNAs: A novel material for long-wavelength semiconductor lasers,” *IEEE J. Select. Topic. Quantum Electron*., vol. 4, no. 3, pp. 719–730, 1997.

[113] T. Makimoto, H. Saito, T. Nishida, and N. Kobayashi, “Excitonic luminescence and absorption in dilute $GaAs_{1-x}N_x$ alloy (x<0.3%),” *Appl. Phys. Lett.*, vol. 70, pp. 2984–2986, 1997.

[114] Z. Pan, L. H. Li, W. Zhang, R. H. Wu, and W. Ge, “Effect of rapid thermal annealing on GaInNAs/GaAs quantum wells grown by plasma-assisted molecular-beam epitaxy,” *Appl. Phys. Lett*., vol. 77, pp. 1280–1282, 2000.

[115] Z. Pan, T. Miyamoto, DietmarSchlenker, F. Koyama, and K. Iga, “Quality improvement of GaInNAs/GaAs quantum well growth by metalorganic chemical vapor deposition using tertiarybutylarsine,” *Jpn. J. Appl. Phys.*, vol. 38, pp. 1012–1024, 1999.

[116] T. Kitatani, K. Nakahara, M. Kondow, K. Uomi, and T. Tanaka, “Mechanism analysis of improved GaInNAs optical properties through thermal annealing,” *J. Crystal Growth*, vol. 209, pp. 345–349, 2000.

[117] M. Albrecht, V. Grillo, T. Remmele, H. P. Strunk, A. Yu Egorov, Gh. Dumitras, H. Riechert, A. Kaschner, and A. Hoffmann, “Effect on annealing on the In and N distribution in InGaAsN quantum well,” *Appl. Phys. Lett*., vol. 81, pp. 2719–2721 ,2002.

[118] H. Y. Liu, M. Hopkinson, P. Navaretti, M. Gutierrez, J. S. Ng, and J. P. R. David, “Improving optical properties of 1.55 μm GaInNAs/GaAs multiple quantum wells with Ga(In)NAs barrier and space layer,” Appl. Phys. Lett., vol. 83, pp. 4951–4953, 2003.

[119] I. Suemune, “Theoretical estimation of leakage current in II-VI heterostructure lasers,” *Jpn. J. Appl. Phys*., vol. 31, pp. L95–L98, 1992.

[120] D. Gollub, S. Moses, M. Fischer, and A. Forchel, “1.42 μm continuous-wave operation of GaInNAs laser diodes,” *Electron. Lett.* vol. 39 pp. 777–778, 2003.

[121] N. Tansu, N. J. Kirsch, and L. J. Mawst, “Low-threshold-current-density 1300-nm dilute-nitride quantum well lasers,” *Appl. Phys. Lett.*, vol. 81, pp. 2523–2525, 2002.

[122] C. S. Peng, T. Jouhti, P. Laukkanen, E. M. Pavelescu, J. Konttinen, W. Li, and M. Pessa, “1.32-mm GaInNAs-GaAs laser with a low threshold current density,” *IEEE Photon. Technol. Lett.*, vol. 14 pp. 275–277, 2002.

[123] D. A. Livshits, A. Y. Egorov, and H. Riechert, "8 W continuous wave operation of InGaAsN lasers at 1.3 μm," *Electron. Lett.*, vol. 36, pp. 1381–1382, 2000.

[124] J. Wei, F. Xia, C. Li, and S. R. Forrest, "High T_0 long-wavelength InGaAsN quantum-well lasers grown by GSMBE using a solid arsenic source," *IEEE Photon. Technol. Lett.*, vol. 14, pp. 597–599, 2002.

[125] A. R. Kovsh, J. S. Wang, R. S. Hsiao, L. P. Chen, D. A. Livshits, G. Lin, V. M. Ustinov, and J. Y. Chi, "High-power (200 mW) singlemode operation of InGaAsN/GaAs ridge waveguide lasers with wavelength around 1.3 μm," *Electron. Lett.*, vol. 39, pp. 1726–1728, 2003.

[126] Y. Qu, C. Y. Liu, S. G. Ma, S. Yuan, B. Bo, G. Liu, and H. Jiang, "High-power ridge waveguide InGaAsN lasers fabricated with pulsed anodic oxidation," *IEEE Photon. Technol. Lett.*, vol. 16, pp. 2406–2408, 2004.

[127] N. Tansu, J. Y. Yeh, and L. J. Mawst, "Improved photoluminescence of InGaAsN-(In)GaAsP, quantum well by organometallic vapor phase epitaxy using growth pause annealing," *Appl. Phys. Lett.*, vol. 82 pp. 3008–3010, 2003.

[128] N. Tansu, A. Quandt, M. Kanskar, W. Mulhearn, and L. J. Mawst, "High-performance and high-temperature continuous-wave-operation 1300 nm InGaAsN quantum well lasers by organometallic vapor phase epitaxy," *Appl. Phys. Lett.*, vol. 83 pp. 18–20, 2003.

[129] N. Tansu and L. J. Mawst, "Low-threshold strain-compensated InGaAs(N) (λ=1.19-1.31 μm) quantum-well lasers," *IEEE Photon. Technol. Lett.*, vol. 14, pp. 444–446, 2002.

[130] A. Y. Polyakov, N. B. Smirnov, A. V. Goverkov, A. E. Botchkarev, N. N. Nelson, M. M. E. Fahmi, J. A. Griffin, A. Khan, S. N. Mohammad, D. K. Johnstone, V. T. Bublik, K. D. Chsherbatchev, M. I. Voronova, and V. S. Kasatochkin, "Optical properties and defects in GaAsN and InGaAsN films and quantum well strucutres," *Solid-State Electron.*, vol. 46, pp. 2147–2153, 2002.

[131] R. Fehse , S. Tomic, A. R. Adams, S. J. Sweeney, E. P. O'Reilly, A. Andreev, and H. Riechert, "A qualitative study of radiative, Auger, and defect related recombination process in 1.3-μm GaInNAs-based quantum-well lasers," *IEEE J. Select. Topic. Quantum Electron.*, vol. 8, pp. 801–810, 2002.

Chapter 2 Physical and numerical models

In this chapter, a description of the fundamental theories in the all of the simulation programs (APSYS, LASTIP, and PICS-3D) used in this dissertation is applied. Since the drift-diffusion model is though to be the governing model of semiconductors and the most basic equations to illustrate the electric behaviors of a semiconductor device, it is shown in advance. The QW models with relevant interband optical transition such as optical gain/absorption calculation, self-consistent carrier density and optical gain with many-body coulomb interaction in wide-bandgap nitride-based materials are investigated. Thermal effects in semiconductors are included. At last, the specific models used in each of the three simulation programs are given.

2-1 Drift-diffusion model

To describe the semiconductor device behavior, Poisson's equation, in which can be shown in a typical form as $\nabla^2 V = -\rho/\varepsilon$, is though to be the basic. As considered in the semiconductors, this equation to describe the electric field shall be revised as

$$-\nabla\left(\frac{\varepsilon_0\varepsilon_{dc}}{q}\times\nabla V\right) = -n + p + N_D(1-f_D) - N_A f_A + \sum_j N_{tj}(\delta_j - f_{tj}), \tag{2.1}$$

where ∇V represents the electric field, ε_{dc} is the relative dielectric constant, n and p are the electron and hole concentrations, N_A and N_D are the acceptor and donor doping concentration with respective Fermi levels of f_A and f_D, δ_j is a delta-function that equals to zero when acceptor is considered and equals to one when donor is considered. Also, based on the current continuity equation, $\nabla J + \partial\rho/\partial t = 0$, it can be

$$\nabla J_n - \sum_j R_n^{tj} - R_{sp} - R_{st} - R_{au} = \frac{\partial n}{\partial t} + N_D\frac{\partial f_D}{\partial t}, \text{ and} \tag{2.2}$$

$$\nabla J_p + \sum_j R_p^{tj} + R_{sp} + R_{st} + R_{au} = -\frac{\partial p}{\partial t} + N_A \frac{\partial f_A}{\partial t} \tag{2.3}$$

to describe the electron and hole continuities in semiconductors, where the carrier flux density is equal to $J_n = n \cdot \mu_n \cdot \nabla E_{fn}$ and $J_p = p \cdot \mu_p \cdot \nabla E_{fp}$. In equation (2.1), the recombination rates in each confined energy deep level traps, spontaneous emission, stimulated emission, and Auger are represented, respectively, and are illustrated subsequently.

The carrier recombination due to deep level traps (Shockley-Reed-Hall, SRH recombination), which is one of the main nonradiative recombination processes, can be illustrated in the following expressions:

$$R_n^{tj} = c_{nj} \cdot n \cdot N_{tj}(1 - f_{tj}) - c_{nj} \cdot n_{1j} \cdot N_{tj} \cdot f_{tj} - G_{tn}, \tag{2.4}$$

$$R_p^{tj} = c_{pj} \cdot p \cdot N_{tj} \cdot f_{tj} - c_{pj} \cdot p_{1j} \cdot N_{tj}(1 - f_{tj}) - G_{tp}, \tag{2.5}$$

with the trap occupancy $0 < f_t < 1$. n_{1j} is the electron concentration when the electron quasi-Fermi level coincides with the energy level E_{tj} of the *j*th trap. Under transient condition, the dynamic variation of the trap occupancy can be $N_{tj} \cdot \partial f_{tj} / \partial t = R_n^{tj} - R_p^{tj}$, and because the capture coefficient is related to the carrier lifetime and carrier concentration as $1/\tau_j = c_j \cdot N_j$, which can be further expressed by

$$c_{nj} = \sigma_{nj} \cdot \sqrt{8kT/(\pi \cdot m_n)}, \tag{2.6}$$

$$c_{pj} = \sigma_{pj} \cdot \sqrt{8kT/(\pi \cdot m_p)}. \tag{2.7}$$

Each last term in expressions (2.4) and (2.5) can be though as the photon-carrier generation to emission. Because it is still possible to generate photo-carriers if deep level traps are sensitive to light whose energy is less than the semiconductor bandgap, it shall be taken into account. In general, this term is proportional to the trap density and

carrier occupancy, as given by

$$G_{tn} = v_g \cdot S \cdot N_{tj} \cdot f_{tj} \cdot \sigma_{xn}, \tag{2.8}$$

$$G_{tp} = v_g \cdot S \cdot N_{tj} \cdot (1 - f_{tj}) \cdot \sigma_{xp}, \tag{2.9}$$

for trapped electrons and holes where v_g is the group velocity of light, S is the photon density, σ_x is the unit of area.

Another main nonradiative recombination, which is shown by the terms of R_{au} in equations (2.2) and (2.3), is the Auger recombination. The rate can be determined by

$$R_{au} = (C_n \cdot n + C_p \cdot p) \cdot (np - n_i^2), \tag{2.10}$$

with the Auger coefficients C_n and C_p. As for the electron and hole concentrations in semiconductors, Fermi-Dirac distributions and a parabolic density of states which, when integrated, yield

$$\begin{aligned} n &= N_c \cdot F_{1/2} \cdot (\frac{E_{fn} - E_c}{kT}), \\ p &= N_v \cdot F_{1/2} \cdot (\frac{E_v - E_{fp}}{kT}), \end{aligned} \tag{2.11}$$

where $F_{1/2}$ is the Fermi integral of order one-half. The occupancies f_D and f_A are used to describe the degree of ionization of shallow impurities in semiconductors. It is assumed that the shallow impurities are in equilibrium with the local carriers, and therefore can be

$$\begin{aligned} f_D &= \frac{1}{1 + g_d^{-1} \cdot \exp[(E_D - E_{fn})/kT]}, \\ f_A &= \frac{1}{1 + g_a \cdot \exp[(E_A - E_{fp})/kT]}, \end{aligned} \tag{2.12}$$

where g_d and g_a are the donor and acceptor wave functions.

The carrier mobilities μ_n and μ_p, which account for the scattering mechanism in electrical transport, is typically as a function of the electric field. In the simulation

program, a commonly used mobility model has the following forms for electrons and holes:

$$\mu_n = \frac{\mu_{0n}}{(1+(\mu_{on}F/v_{sn})^{\beta n})^{1/\beta n}},$$
$$\mu_p = \frac{\mu_{0p}}{(1+(\mu_{op}F/v_{sp})^{\beta p})^{1/\beta p}}, \quad (2.13)$$

where β is used to define a unitless parameter appearing in the field dependent carrier mobility function of the semiconductors.

2-2 Optical gain/absorption calculation for quantum well

In the simulation programs, the QW models assume the QW having a single, symmetric, flat-band, and step-wise potential profile. Parabolic subbands are assumed, and non-parabolic subbands appear while the valence mixing model is taken into account. The calculation of QWs always starts from the QWs without external applied field. All the confined levels in QWs for the subbands of Γ, L, light holes, and heavy holes (and crystal field holes for wurtzite) are computed from well-known formulas in quantum mechanics for a square QW [1]. As external filed is applied, the quasi-Fermi levels are allowed to vary as a function of distance. The density of states and quantum levels are assumed to be the same as if there is no applied filed. The density of electrons and holes in a QW is revised from expression (2.11), and can be expressed by

$$n = \sum_j \rho_j^0 kT \ln[1+e^{(E_{fn}-E_j)/kT}] + unconfined\ \ electrons,$$
$$p = \sum_i \rho_i^0 kT \ln[1+e^{(E_i-E_{fp})/kT}] + unconfined\ \ holes, \quad (2.14)$$

where the subscript *i* denotes all confined states for the different hole bands, and *j* denotes those for the Γ and L bands. The number of unconfined carriers is calculated using Fermi-Dirac distributions.

As the QW is strained, the valence band of III-V semiconductors splits into separated light-hole and heavy-hole bands. The bands become strongly non-parabolic.

To treat this, an anisotropic parabolic band structure is approximated to simplify the calculation of gain, spontaneous emission, and carrier concentration. For zinc-blende structure, a simplified analytical band structure of a strained QW is developed [2], and is based on the $k \cdot p$ theory. Typically, by using the Luttinger-Kohn model [3], the valence band structure can be described by a 6×6 Hamiltonian in the envelope function space [4] as

$$H^{v}(k) = \begin{bmatrix} H^{U}_{3\times3}(k) & 0 \\ 0 & H^{L}_{3\times3}(k) \end{bmatrix},$$

$$H^{\sigma}_{3\times3}(k) = \begin{bmatrix} P+Q-V_h(z) & R_k \mp iS_k & \sqrt{2}R_k \pm \frac{i}{\sqrt{2}}S_k \\ R_k \pm iS_k & P-Q-V_h(z) & \sqrt{2}Q \pm i\sqrt{\frac{3}{2}}S_k \\ \sqrt{2}R_k \mp \frac{i}{\sqrt{2}}S_k & \sqrt{2}Q \mp i\sqrt{\frac{3}{2}}S_k & P+\Delta(z)-V_h(z) \end{bmatrix}, \tag{2.15}$$

where

$$P = P_k + P_\varepsilon, \quad Q = Q_k + Q_\varepsilon$$

$$P_k = \left(\frac{\hbar^2}{2m_0}\right)\gamma_1\left(k_t^2 + k_z^2\right),$$

$$Q_k = \left(\frac{\hbar^2}{2m_0}\right)\gamma_2\left(k_t^2 - 2k_z^2\right),$$

$$R_k = \left(\frac{\hbar^2}{2m_0}\right)\sqrt{3}\left(\frac{\gamma_2+\gamma_3}{2}\right)k_t^2, \tag{2.16}$$

$$S_k = \left(\frac{\hbar^2}{2m_0}\right)2\sqrt{3}\gamma_3 k_t k_z,$$

$$P_\varepsilon = -a_v\left(\varepsilon_{xx}+\varepsilon_{yy}+\varepsilon_{zz}\right),$$

$$Q_\varepsilon = -\frac{b}{2}\left(\varepsilon_{xx}+\varepsilon_{yy}-2\varepsilon_{zz}\right),$$

$V_h(z)$ is the unstrained valence band edge, k_t is the wave factor in the plane of QW. a_v and b are the deformation potentials. $\Delta(z)$ is the spin-orbit split-off energy. γ_1, γ_2, and γ_3 are the Luttinger parameters. In general, the reference energy is taken to be the top of the unstrained valence band. For QW, k_z is replaced by $-i(d/dz)$. The

valence band structures are obtained by solving the expression (2.15). Within the effective mass approximation, the wave function of a QW can be though in the Schrödinger equation by adding an appropriate potential $V_{qw}(z)$ to the periodic potential $V(\vec{r})$ of the crystal lattice, and is given by $\Psi(\vec{r}) = \Phi(z)u_{no}(\vec{r})$. The envelope function $\Phi(z)$ is the solution to the one-dimensional Schrödinger equation:

$$\left[-\frac{\hbar^2}{2}\frac{d}{dz}\frac{1}{m_n^z(z)}\frac{d}{dz}+V_{qw}(z)\right]\Phi(z) = E(k_z)\Phi(z), \tag{2.17}$$

where the periodic crystal potential $V(\vec{r})$ is represented by the effective mass $m_n^z(z)$, which is different for well and barrier material. The subscript *n* is band index.

The optical gain spectrum is then calculated by taking the valence band mixing into account over k_t as [3]

$$g(E) = \frac{q^2\hbar}{2\varepsilon_0 cm_0^2 ntE}\sum_{ij}\int_0^\infty \frac{(\pi/\Gamma)f_{dip}(k_t)M_b(f_j - f_i)dk_t^2}{1+(E_{cj}(k_t)-E_{kpi}(k_t)-E)^2/\Gamma^2} \tag{2.18}$$

where t is QW thickness, $\Gamma = \hbar/\tau_{scat}$ is broadening due to intraband scattering relaxation time, E_{cj} is the jth conduction subband, E_{kpi} is the ith valence subband from the $k\cdot p$ calculation, n is the refractive index. M_b is the bulk dipole moment given by

$$M_b = \frac{1}{6}\frac{m_0 q}{m_c}\frac{E_{g0}(E_{g0}+\Delta_{so})}{E_{g0}+(2/3)\Delta_{so}}, \tag{2.19}$$

f_j and f_i are the Fermi functions expressed by

$$\begin{aligned} f_j^{-1} &= 1+e^{\left[\frac{1}{kT}\left(E_{cjo}+\frac{\hbar^2k_t^2}{2m_0m_c}-E_{fn}\right)\right]}, \\ f_i &= 1+e^{\left[\frac{E_{kpi}(k_t)}{kT}\right]}. \end{aligned} \tag{2.20}$$

The evaluation of spontaneous emission rate when a laser is under threshold can be expressed by

$$R_{sp}^{qw}(E) = \int_0^\infty [\sum_{i=j}(\frac{\hbar}{2\pi})\cdot(\frac{q}{m_0})^2\cdot(\frac{2\hbar w}{4\varepsilon_1\varepsilon_0 w^2})\cdot M_{ij}^2\cdot f_j'(1-f_i')\cdot D(E)\cdot\rho_{ij}]dE \tag{2.21}$$

where $D(E)$ is the optical mode density in the material which has a refractive index of n, given by $D(E) = n^3 E^2 / \pi^2 \hbar^3 c^3$. $|M_{ij}|$ is a transition matrix element being averaged over all polarization directions. The Fermi factor $f_j^{'}(1-f_i^{'})$ gives the probability that the conduction band level is occupied and the valence band level is empty at the same time [5].

2-3 Self-consistent carrier density in nitrides

To solve the quantum confined states in uneven band condition when the local potential well is under strong piezoelectric effect in nitride-based materials, it is assumed in the simulation program that the well is tilted to one side, as well as the wave function, the optical transition between conduction and valence bands will have a different dipole moment. The two-dimensional self-consistent electron density is given as

$$n_{2D}(x,y) = \sum_j g_n^j(y) \rho_o^j kT \ln(1 + e^{\frac{E_{fn}(x,y) - E_j}{kT}}), \tag{2.22}$$

where $g_n^j(y)$ is the electron wave function assuming the well is parallel to x-axis. ρ_o^j is the 2D density of states.

The confined hole density can be written as an integral over the non-parabolic subbands $E_j(k)$,

$$p = \sum_j g_p^j(y) \frac{1}{2\pi} \sum_{-\infty}^{E_k(0)} [1 - f_v(E_j(k), E_{fp})] dk^2. \tag{2.23}$$

2-4 Many-body Coulomb interaction in nitrides

It has been reported that the inter-band Coulombic enhancement of the optical

transitions, together with a bandgap renormalization result in an increase in gain and a reduction in the antiguiding or linewidth enhancement factor [6]. Especially, the Coulomb enhancement is stronger in short wavelength ZnCdSe and nitrides due to the lower values of dielectric constant in wide bandgap materials. Many-body carrier-carrier Coulomb interaction can be though as it attracts the electrons and holes in the QW active region so closer that the radiative recombination rate is enhanced. As a result, the spontaneous emission increases with a shift of gain peak towards to lower energies. The Coulomb interaction effects the bandgap to renormalize and the inter-band recombination of electrons and holes. Often, it is called bandgap narrowing effect because of the screening of conduction band electron-electron Coulomb repulsion by positively charged valence band holes available near electrons. If think the renormalization bandgap as $E_{g-ren} = E_g + \Delta E_g$, the total bandgap narrowing is given by ΔE_g with $\Delta E_g = \Delta E_{gCH} + \Delta E_{gSX}$, where ΔE_{gCH} is called the Coulomb Hole bandgap renormalization and ΔE_{gSX} is called self-energy correction to electron-hole plasma due to exchange interaction. The Coulomb Hole contribution to the bandgap reduction can be given in two-dimension by

$$\Delta E_{CH} = -2E_0 a_0 k \cdot \ln[1 + \sqrt{32\pi N_{2D} / C_{pl}\kappa^3 n_0}] \qquad (2.24)$$

where a_0 is the Bohr radius of QW electron-hole exciton given by $4\pi^2\hbar^2\varepsilon_b\varepsilon_0 / e^2 m_{rj}$, and E_0 is corresponding effective Rydberg energy given by $\hbar^2 / 2m_{rj}a_0^2$. κ is the inverse screening length for electrons and holes confined in the QW. C_{pl} is a unitless constant typically n a range of 1–4. The reduction of bandgap energy due to electron-hole plasma exchange interaction is given by

$$\Delta E_{gSX} = -\frac{2E_0 a_0}{k}\int_0^{\infty} dkk \frac{1 + C_{pl}\kappa a_0 k^2 / 32\pi N_{2D}}{1 + q/\kappa + C_{pl} a_0 k^3 / 32\pi N_{2D}}\left[f_e(E_{cjk} + f_h(E_{vjk})\right] \qquad (2.25)$$

The effected gain spectral function derivation after including interaction becomes

$$g(\hbar w) = real\left\{\int_{E_{g0}}^{\infty} \frac{g_0(E_{cv})}{1 - q_1(E_{cv}, \hbar w)}\left[1 - i\frac{E_{cv} - \hbar w}{\Gamma_{cv}}\right] L(\hbar w - E_{cv}) dE_{cv}\right\}, \qquad (2.26)$$

in which

$$q(E_{cv}, \hbar w) = \frac{-ia_0 E_0 E_{cv}}{\pi k \left|M_{ji}(E_{cv})\right|}\int_0^{\infty} dk' k' \frac{\left|M_{ji}(E_{cv'})\right|}{E_{cv'}} \times \frac{f_e(E_{cjk'}) + f_h(E_{vjk'}) - 1}{\Gamma_{cv} + i(E_{cv} - \hbar w)} \times \Theta(k, k'),$$

$$\Theta(k, k') = \int_0^{2\pi} d\theta \frac{1 + C_{pl} k a_0 q^2 / 32\pi N_{2D}}{1 + q/k + C_{pl} k a_0 q k^3 / 32\pi N_{2D}},$$

and $q^2 = k^2 + k'^2 - 2kk'\cos\theta,$ (2.27)

where where θ is the angle between in-plane vectors k and k'; $g_0(E_{cv})$ is the spectral wave function, which consists of a sum of $g_{ji}(E_{cv})$ contributions from transitions between j^{th}-subband electrons and i^{th}-subband holes; Γ_{cv} represents the Lorenzian width and equals to $\hbar / \tau_{cv}$, which is simplified without considering the dependence upon $\hbar w$ and E_{cv} energies in the calculations; a_0 is exciton Bohr radius given by $4\pi\hbar^2 \varepsilon_b \varepsilon_0 / e^2 m_{rj}$; E_0 is the corresponding Rydberg energy; E_{cv} is specified by $E_{cv}(k) = E_g + \Delta E_g + E_{cjk} + E_{vik}$ where E_{cjk} and E_{vik} are electron and hole energies from j^{th}-subband of conduction band and i^{th}-subband of valence band in the QW active region; $\left|M_{ji}\right|^2$ is the transition matrix element.

2-5 Thermal effects

For the treatment of device heating, the thermoelectric power and thermal current induced by temperature gradient are solved utilizing the method provided by Wachutka [7]. Various heat sources, including Joule heat, generation/recombination heat,

Thomson heat, and Peltier heat, are taken into account in this dissertation.

Joule heat

In Joule heating, the heat sources can be from two parts, which are the steady state or low frequency part of the electric field and the optical frequency. In which,

$$H_{Joule-dc} = \frac{J_n^2}{q\mu_n n} + \frac{J_p^2}{q\mu_p p} \tag{2.28}$$

The heating caused by the optical frequency can be regarded as the absorption by the impure material, which the internal loss is the cause. A simple derivation of this term is

$$power\ loss = \sigma_{op} F_{op}^2 = \frac{\overline{n}_1 \alpha_i}{k_0} \varepsilon_0 \omega F_{op}^2 \tag{2.29}$$

where the optical field F_{op} is the root mean square of the oscillating field.

Generation/recombination heat

The generation/recombination heat comes from an assumption that the photons emitted by spontaneous radiative recombination are eventually absorbed by the semiconductor and are converted into heat. The heated is released from the difference between the quasi-Fermi levels as

$$H_{rec} = (R_{trap} + R_{Aug} + R_{spon})(E_{fn} - E_{fp}) \tag{2.30}$$

Thomson and Peltier heat

The Thomson heat comes from the change in thermoelectric power when an electron-hole pair recombines:

$$H_T = qR_{total} T(P_p - P_n) \tag{2.31}$$

where P_p and P_n are thermoelectric power for holes and electrons. The Peltier heat is related to the spatial variation in thermoelectric power:

$$H_p = -T(J_n \nabla P_n + J_p \nabla P_p) \tag{2.32}$$

2-6 Specific models in APSYS

APSYS is a simulation program that to model almost devices, except for semiconductor lasers, such as silicon MOSFET's, HBTs, and LEDs, etc. It is a two-dimensionally powerful simulation program, which mainly solve, self-consistently, the Poisson's equations, current continuity equations, carrier energy transport equations, and heat transfer equations. Mainly, the APSYS simulation program used in this dissertation is to model and optimize our fabricated ultraviolet InGaAlN/InGaAlN LED. Based on the semiconductor physics, it is well-known that the LEDs are quite different from laser devices because LEDs operate well below laser threshold and no stimulated emission is observed. Continuous emission spectrum have to be considered for LEDs while longitudinal modes of laser only require a limited number of lasing wavelength. The spontaneous emission power shall be calculated by the integral of all mode spontaneity:

$$P_{spon}(w)\Delta w = (1-\gamma_1^2)\frac{n_g}{6n} A\int_0^L \left|Z_2(z_s)\right|^2 dz_s(\hbar w \cdot r_{sp}^{qw}(E))\Delta E, \qquad (2.33)$$

where in the APSYS simulation program, the LED is regarded as a special case of Fabry-Peröt laser with cavity length of L, and the waveguiding is in the z-direction. While at the same time, it is assumed that the extraction efficiency is concerned in only one facet with a factor of 1/6. γ_1 is set from the wave function in a Fabry-Peröt cavity, and can be though as a value of facet reflectivity. A is the active region cross section in the LED. The extracted output power from the LED top surface can be:

$$P_L(w)\Delta w = \sum_{ny}(1-r_1^2)\frac{n_g}{n}\frac{L_x g_l}{k}\int_0^L \left|Z_2(z_s)\right|^2 dz_s(\hbar w)\left\langle n\left|r_{sp}^{qw}(E)\right|n\right\rangle \cdot \Delta E, \qquad (2.34)$$

where n and n_g are the indices, and g_l is a integral constant. The ratio of P_L/P_{spon} gives the LED external efficiency.

2-7 Specific models in LASTIP

LASTIP (LASer Technology Integrated Program) is a simulation tool to model the electrical and optical behaviors in a semiconductor laser in two dimensions. Typical laser emission L-I-V curves, 2D potential, electric field, and current distribution, special electron and hole concentrations, band diagram, optical field distribution, gain spectrum, and far-field patterns can be obtained. It is a useful simulation program to give a qualitatively theoretical analysis and to provide a way to realize the physics of the optoelectronic semiconductor lasers. Typically, LASTIP is used to simulate an edge emitting laser by solving the photon rate equation of stimulated recombination and typical drift-diffusion equations etc. The stimulated emission rate, R_{st} defined in LASTIP is as the rate of photon emission per unit volume as a result of material gain enhanced by traveling waves. The modal gain can be

$$g_m = \frac{1}{P}(\hbar\omega)\int R_{st}\,dxdy \tag{2.35}$$

where P represents the power, can be further replaced by $P = \hbar\omega v_g S$ under using group velocity as the traveling speed of the optical power; v_g is the group velocity and can be $1/v_g = \partial k/\partial\omega$. S gives the photon number in the 2D simulation plane. By normalizing a 2D optical wave function W as $\int |W|^2\,dxdy = 1$, we can have

$$g_m = \int g(x,y)|W|^2\,dxdy\,. \tag{2.36}$$

Combining equations (2.35) and (2.36), we therefore can have an expression of R_{st} as

$$R_{st} = v_g \cdot g(x,y) \cdot S \cdot |W|^2$$

Therefore the stimulated emission can be $\int R_{st}\,dxdy = v_g g_m S$.

2-8 Specific models in PICS-3D

PICS-3D (Photonic Integrated Circuit Simulator in 3D) is a program to simulate

laser diodes and related waveguiding photonic devices, such as VCSELs, DFB lasers etc., in three dimensions. PICS-3D usually combines solutions of the semiconductor equations in multiple 2D cross sections of a waveguiding device with the longitudinal mode solution to construct a quasi-3D model of a photonic device. It to model a VCSEL device, a cylindrical coordinate system shall be set up to treat the drift-diffusion model in 3D characteristics. As well, a multiple longitudinal mode must be solved. The differential equations in drift-diffusion models shall be revised by converting the gradient parts into cylindrical symmetry coordinate system:

$$\nabla u = \frac{\partial u}{\partial r} e_r + \frac{\partial u}{\partial z_r} e_z \tag{2.37}$$

and the divergence by

$$\nabla \cdot A = \frac{1}{r}\left[\frac{\partial}{\partial r}(rA_r) + \frac{\partial}{\partial z_r}(rA_z)\right]. \tag{2.38}$$

For the calculation of lateral optical modes of a VCSEL, an effective index method approximation [8] is utilized. This method is useful if the VCSEL structure becomes more complex, especially when a oxide confine layer is existed. Based on the solution of scalar wave equation in VCSELs, the laterally optical modal filed distribution is solved in

$$\frac{-c}{2k_0 < \varepsilon_i >}\left[\frac{1}{r}\frac{\partial}{\partial r} r \frac{\partial}{\partial r} - \frac{m}{r^2} + k_0^2 \Delta\varepsilon_{eff}\right]\Psi_{mn} = \Delta\omega_{mn}\Psi_{mn} \tag{2.39}$$

where ε_i is the relative permittivity of a region in the transverse direction in which the effective index is calculated. $k_0 = \omega_0 / c$, $\Delta\omega_{mn}$ is the deviation of the LP_{mn} mode from the angular oscillation frequency ω_0. Ψ_{mn} represents the modal field distribution function as $\Psi_{mn}(r,\phi,t) \equiv \Psi_{mn}(r,t)e^{im\phi}$.

References

[1] D. I. Blokhintsev, "*Quantum mechanics*," D. Reidel Publishing Company, Dordrecht-Holland, Corzine, (1964).

[2] S. L. Chuang, "Efficient band-structure calculation of strained quantum-wells," *Phys. Rev. B*, vol. 43, pp. 9649–9661, 1991.

[3] S. L. Chuang, "*Physics of Optoelectronic Devices*," John Wiley & Sonc., Inc., New York, (1995).

[4] C. Y. P. Chao and S. L. Chuang, "Spin-orbit-coupling effects on the valence-band structure of strained semiconductor quantum wells," *Phys. Rev. B*, vol. 46, pp. 4110−4122, 1992.

[5] R. H. Yan, S. W. Corzine, L.A. Coldren, and I. Suemune, "Corrections to the expression for gain in GaAs," *IEEE J. Quantum Electron.*, vol. 26, pp. 213–216, 1990.

[6] W. W. Chow and S. W. Koch, "Many-body coulomb effects in room-temperature II-VI quantum well semiconductor lasers," *Appl. Phys. Lett*., vol. 66, pp. 3004–3006, 1995.

[7] G. K. Wachutka, "Rigorous thermodynamic treatment of heat generation and conduction in semiconductor device modeling," *IEEE Trans. Comput.-Aided Des. Integr. Circuits Syst.*, vol. 9, pp. 1141–1149, 1990.

[8] G. R. Hadley, K. L. Lear, M. E. Warren, K. D. Choquette, J. W. Scott, and S. W. Corzine, "Comprehensive numerical modeling of vertical-cavity surface-emitting lasers," *IEEE J. Quantum Electron.*, vol. 32, pp. 607–616, 1996.

Chapter 3 Ultraviolet AlGaInN/GaN LEDs

During the past few years, greatly impressive development of III-V nitride based light emitting devices have been witnessed for illuminated devices, laser diode light sources for high-density optical storage system, full-color display, and medical applications. High-efficiency GaN-based LEDs between the UV and amber spectral regions are now commercially available [1–6]. Especially, UV LEDs have recently attracted much attention to be strong candidate in biological agent detection, air cleaner, and transceivers for convert nonlinear-of-sight optical communications. As well, using UV LEDs as light emitters to excite phosphor can achieve white fluorescence for solid state lighting. The LEDs with an emission wavelength less than 370 nm are specifically significant due to most of the phosphors can absorb and provide a more effective down-conversion quantum efficiency. To date, the UV LEDs in a spectral region of 267–370 nm have been successfully fabricated [7–10]. However, as decreasing UV LED emission wavelength to a deeper level in the fabrication of UV LEDs, a rapid degradation of light output power is observed. The reason had been found to be attributed to the large threading dislocation, poor carrier confinement in the QW active region, and self absorption in the thick GaN contact layers [11].

As expected to be a replacement of conventional incandescent and fluorescent lamps, high-efficiency UV LEDs are strongly demanded. In particular, the UV LED with an emission wavelength between 365–370 nm is more favorable due to it can provide relatively higher output performance to pump phosphors [3].

3-1 Literature survey

To fabricate an UV LED with 365–370 nm emission, InGaN, AlGaN or quaternary AlGaInN are expected to be applied as QW active region in UV LEDs due to the

naturally direct high-bandgap transition. However, as compared with those of the visible LEDs, the illuminated power and efficiency of the UV LEDs are extremely worse. While, the reasons had been observed due to some factors, including defects in the quantum well active region, device heating under continuous-wave operation, and especially carrier leakage from the active region.

Significant progress of UV LEDs had been made in emission wavelength region of 325–400 nm with mW output [12–15]. For UV LEDs with an emission wavelength of 267 nm, AlGaN-based LEDs with a pulse operation output power of 4.5 mW and 165 μW at 435 mA under CW operation for an array of four LEDs in parallel had been demonstrated by Yasan *et al.* [16]. For 365 nm UV LEDs, with the use of laser-induced liftoff and polishing technologies, Morita *et al.* had obtained an output power of 100 mW with an external quantum efficiency of 5.6% at 500 mA [17]. On the other hand, with an emission wavelength shorter than the characteristic wavelength corresponding to the GaN bandgap, Nishida *et al*. adopted a short period alloy superlattice as p-type cladding and p-type contact layers to have a transparent 348–351 nm LED with 7 mW output at 220 mA [18].

These efforts had made the UV LEDs to have an acceptable output characteristic; however, it needs to be mentioned that substantial work is necessitated with an aim to improve the emitting power and efficiency. For 370 nm UV LED, the use of quaternary AlGaInN QW active region is beneficial for obtaining better material quality and higher internal quantum efficiency [19]. Zhang *et al.* had also pointed out that the use of quaternary AlGaInN as barriers could drastically improve the heterostructure quality [20]. In this chapter, we presented the growth and fabrication of UV LEDs operating at 370 nm based on quaternary AlGaInN QW active region. To create more efficient UV LED, we further theoretically investigated the relationships of the Al composition in AlGaN electron-block layer and the QW number to the LED output performance, with

an aim to reduce the electron leakage current.

3-2 Device fabrication and characteristics

The LEDs used in this study were grown on c-face sapphire substrate by low-pressure horizontal-flow MOCVD system using a 30-nm-thick low-temperature GaN nucleation layer at 550 °C, followed by a 2-μm-thick high-temperature undoped GaN buffer layer and a 1-μm-thick Si doped GaN to form the n-contact layer at 1050 °C. Next, a 50-nm-thick graded n-type $Al_xGa_{1-x}N$ (x=0.1 to 0.14) was deposited for cladding. Then, the growth temperature was linearly decreased to 850 °C to grow the active region of the UV LED. The active region was consisted of three quaternary $Al_{0.06}Ga_{0.85}In_{0.09}N$ multiple QWs sandwiched by four $Al_{0.05}Ga_{0.94}In_{0.01}N$ barriers. The temperature was afterwards increased to 1050 °C for growing a 25-nm-thick p-type $Al_{0.19}Ga_{0.81}N$ electron-block layer, followed by a 125-nm-thick p-type $Al_{0.09}Ga_{0.91}N$ and a 10-nm-thick p-GaN contact layer to complete the structure.

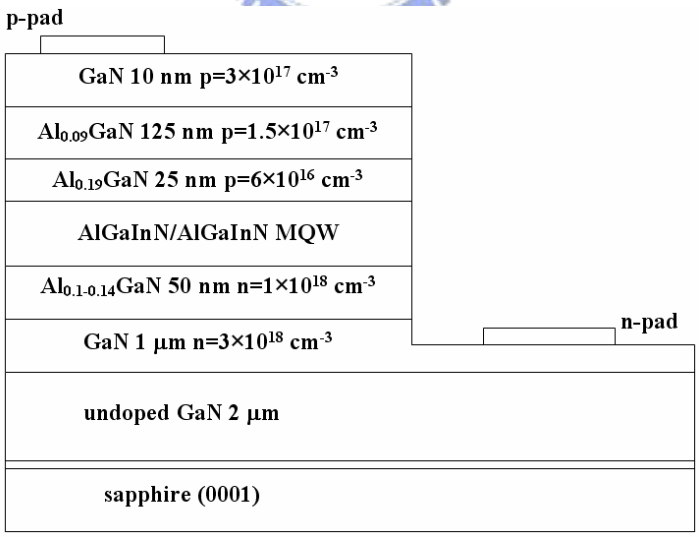

Figure 3.1 A schematic plot of the UV LED device.

After MOCVD growth, the fabrication process began from partially etching by reactive ion etching from the surface of the p-type GaN contact layer until the n-type GaN exposed. Ni/Au metal was evaporated onto the p-type GaN, and Ti/Al metal was

evaporated onto the n-type GaN. The chip size was 300×300 μm^2 and was formed by packing into 5 mm lamps with a standard process for output characteristic measurement. A schematic plot of the UV LED device was shown in Figure 3.1.

The device characteristics were obtained with a probe station, Keithlyn 238 current source, and Newport 1835C power meter module. Electroluminescence (EL) spectrum was measured by Advantec optical spectrum analyzer (OSA) with a 0.1 nm spectrum resolution. Figure 3.2 showed the EL spectrum of the UV AlGaInN LED under continuous-wave operation when the input current was in a range of 10–100 mA. The main peak of the emission wavelength designed slightly longer than 365 nm was for the purpose of preventing strong internal absorption by the bulk GaN, and it shifted from 368 nm to 372 nm with increased input current from 10 mA to 100 mA.

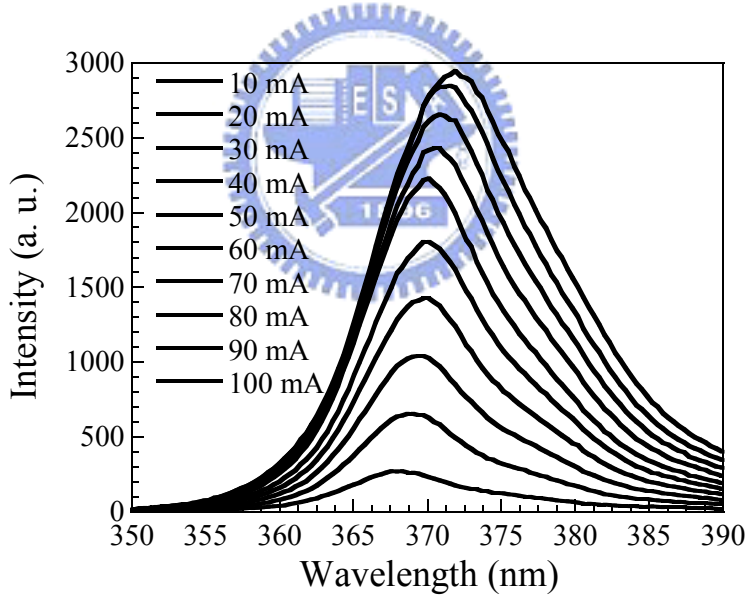

Figure 3.2 EL spectrum of the UV AlGaInN LED under continuous-wave operation when the input current was in a range of 10–100 mA.

Figure 3.3 showed the output characteristics of the UV LED when the device temperature was varied in a range of 300–380 K. During the measurement of the temperature dependent output characteristics, the UV LED was mounted on a hot plate, and the device temperature was monitored with a thermal coupler. The room-temperature UV power of the LED was near 0.8 mW at 20 mA with 3.6 V

operation voltage and increased to 4 mW when the LED was driven at 125 mA under CW operation. The wall plug efficiency was approximately 1.1% and the external quantum efficiency was 1.2%. When the device temperature was operated at 380 K, the UV LED could still provide 0.5 mW output when the input current was 20 mA. A maximum output power of 2.1 mW could be achieved at 380 K when the input current was 100 mA.

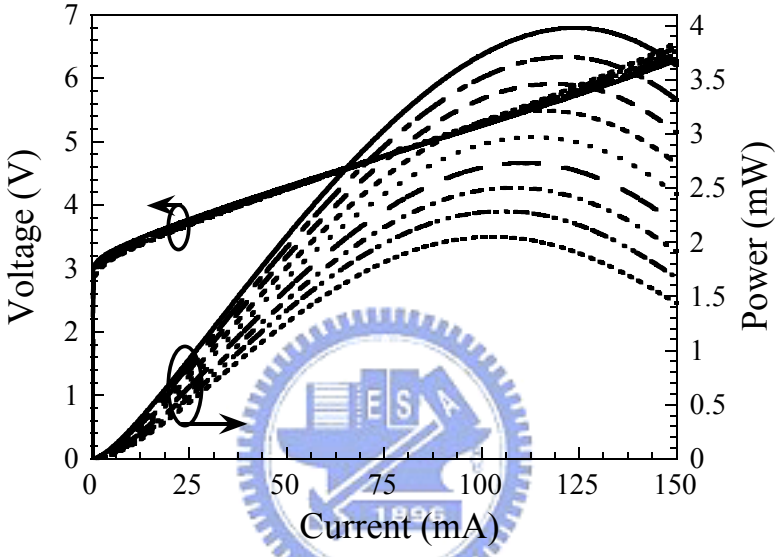

Figure 3.3 Output characteristics of the UV LED when the device temperature was varied in a range of 300–380 K.

For blue and green LEDs, which were made by III-nitride materials, the reports had shown that the main peak of the emission wavelength decreased first and increased afterward as the input current was increased. This phenomenon was found to be attributed to the localized states resulting from indium inhomogeneity. However, there was no short-wavelength shift in our UV AlGaInN LED, and it was supposed that the indium composition in the AlGaInN QWs was much less than that in the blue or green LEDs and the segregation of indium could not dominate under this situation.

3-3 Theoretical analysis

It is universally known that qualitatively theoretical analysis can advantageously provide a way to realize the output characteristic of the optoelectronic semiconductor device. Numerical simulation is always required to model and optimize the output characteristic of the device. In this study, the numerical simulation was executed with the use of an advanced physical model of semiconductor devices (APSYS) [21], which was utilized as a full two-dimensional simulator that solved the Poisson's equation, current continuity equations, photon rate equation and scalar wave equation, and accounts for current spreading in this specific study.

For this specific simulation, the temperature dependent bandgap energies of binary InN, GaN, AlN alloys were governed by Varshni equation and the bowing factors of ternary GaInN, AlGaN and AlInN alloys were 2.4, 0.7, and 2.5 eV respectively [22, 23]. Most Luttinger-like valence band parameters we used in this study such as A_1, $A_2 \cdots A_6$ for nitrides and the deformation potentials, elastic constants, etc. were also obtained from Ref. 13, as listed in Table 1.1, excepted that the electron and hole mobilities were taken from the default database values given in the APSYS material macro file [21].

For the treatment of device heating, the thermoelectric power and thermal current induced by temperature gradient were solved utilizing the methods provided by Wachutka *et al.* [24–26]. Various heat sources, including Joule heat, generation/recombination heat, Thomson heat and Peltier heat, were taken into account in this specific study. The boundary temperature between the LED contacts and the ambiance was solved assuming that the contacts were connected to a thermal conductor with a fixed temperature set by the simulator. The calculation of the interface charge density including spontaneous and piezoelectric polarization in the ternary III-nitride material as a function of composition and microscopic structure was by the use of *ab*

initio density-functional techniques and Berry phase method [27], while we assumed the charges at multiple QWs were with partial 85% screening. For the interface charge of quaternary AlGaInN QW, it was predicted by ternary interpolation formulas [28]:

$$D_{charge}Al_xGa_yIn_zN = \frac{x\cdot y\cdot D_{charge}(Al_uGa_{1-u}N)}{xy+yz+zx} + \frac{y\cdot z\cdot D_{charge}(Ga_yIn_{1-y}N)}{xy+yz+zx} + \frac{z\cdot x\cdot D_{charge}(In_wAl_{1-w}N)}{xy+yz+zx},$$

$$z=1-x-y,\quad u=\frac{1+x-y}{2},\quad v=\frac{1+y-z}{2},\quad w=\frac{1+z-x}{2}. \tag{3.1}$$

while the calculated interface charge densities in the fabricated UV AlGaInN/GaN LED structure were summarized in Table 3.1.

Table 3.1 Net surface charge density at each interface of the UV LED.

Interface	Surface charge density
$GaN/Al_{0.1}Ga_{0.9}N$	$+5.50\times10^{15}$ m^{-2}
$Al_{0.14}Ga_{0.86}N/Al_{0.05}Ga_{0.94}In_{0.01}N$	-6.60×10^{15} m^{-2}
$Al_{0.05}Ga_{0.94}In_{0.01}N/Al_{0.06}Ga_{0.85}In_{0.09}N$	-1.13×10^{16} m^{-2}
$Al_{0.06}Ga_{0.85}In_{0.09}N/Al_{0.05}Ga_{0.94}In_{0.01}N$	$+1.13\times10^{16}$ m^{-2}
$Al_{0.05}Ga_{0.94}In_{0.01}N/Al_{0.19}Ga_{0.81}N$	$+9.50\times10^{15}$ m^{-2}
$Al_{0.19}Ga_{0.81}N/Al_{0.09}Ga_{0.91}N$	-5.80×10^{15} m^{-2}
$Al_{0.09}Ga_{0.91}N/GaN$	-4.90×10^{15} m^{-2}

The numerical spontaneous emission rate spectrum of the UV AlGaInN LED as a function of the input current was shown in Figure 3.4. The inset in Figure 3.4 depicted the main peaks of the numerical spontaneous emission rate spectra and the experimental EL spectra. It was clearly seen that the main peaks of the numerical spontaneous emission rate spectra and the experimental EL spectra were of great agreement. The spontaneous emission rate calculated in this study was given by [29]:

$$r_{sp}^{qw}(E) = \sum_{i,j}\left(\frac{2\pi}{\hbar}\right)\left|H_{ij}\right|^2 f_j(1-f_i)D(E)\rho_{ij}, \tag{3.2}$$

where $\left|H_{ij}\right|^2 = \left(\frac{q}{m_0}\right)^2\left(\frac{2\hbar w}{4\varepsilon_1\varepsilon_0\omega^2}\right)M_{ij}^2$, and $\rho_{ij} = \rho_{ij}^0\cdot h(\hbar\omega - E_{ij}^0)$, (3.3), (3.4)

and f_i, f_j represented the Fermi functions for the i^{th} and j^{th} levels. $D(E)$ was the optical mode density.

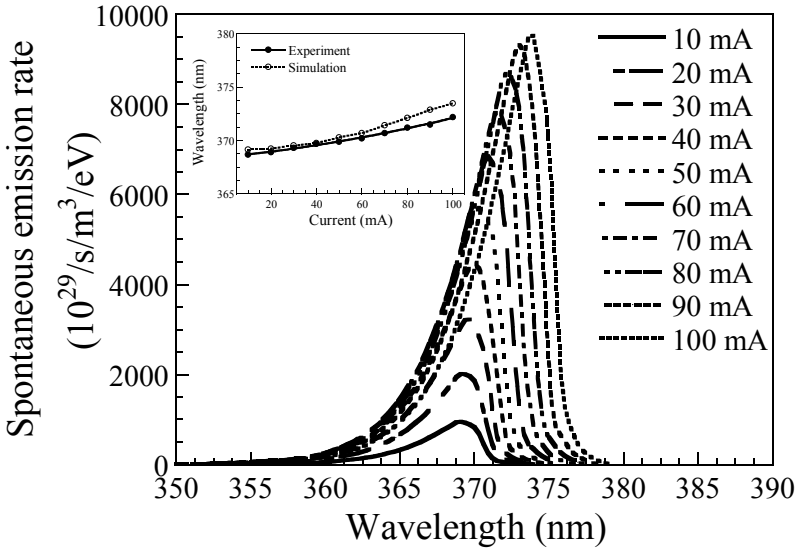

Figure 3.4 Numerical spontaneous emission rate spectrum of the UV AlGaInN LED as a function of the input current. The inset shows the main peaks of the numerical spontaneous emission rate spectra and the experimental EL spectra.

The spontaneous emission power (P_{spon}) was calculated by the integral of all modes spontaneity:

$$P_{spon}(w)\Delta w = A\int_0^L dz_s(\hbar w \cdot r_{sp}^{qw}(E))\Delta E, \tag{3.5}$$

and the extracted output power from the LED top surface was

$$P_L(w)\Delta w = \sum_{ny}(1-r_1^2)\frac{n_g}{n}\frac{L_x g_l}{k}\int_0^L \left|Z_2(z_s)\right|^2 dz_s(\hbar w)\left\langle n\left|r_{sp}^{qw}(E)\right|n\right\rangle \cdot \Delta E, \tag{3.6}$$

where A was the active region cross section in the LED and we regarded the LED as a special case of Fabry-Perot laser with cavity length of L. n and n_g were the indices, and g_l was a integral constant. We wished to underscore that the package loss assumed in this study was zero, and therefore the ratio of P_L/P_{spon} gave the LED external efficiency. Besides, a current efficiency could also be obtained from the ratio of the spontaneous recombination current (I_{spon}) to the total current, which was the sum of the spontaneous recombination current, nonradiative recombination current (I_{nr}), and leakage current (I_{leak}):

$$\eta_{curr} = \frac{I_{spon}}{I_{spon} + I_{nr} + I_{leak}}. \tag{3.7}$$

To fit the experimental LED output characteristic, some parameters were used such as the radiative recombination coefficient for the bulk AlGaInN, AlGaN, GaN was 2.9×10^{-15} m^3/s, the auger coefficients for n and p carrier were both set to 4×10^{-40} m^6/s, and the carrier lifetime was 1 ns [30]. A large internal loss value of 1000 m^{-1} was assumed due to the large defect density in III-V nitride material. It was clearly seen that the temperature dependent light output versus current (*L-I*) characteristic obtained numerically was fit in with the experiment despite that the differential resistance was slightly inconsistent. Practically, the characteristics of the UV AlGaInN LED could be quantitatively analyzed by the simulator with the parameters shown above, which remained unchanged throughout the study. To enhance the output power of the UV AlGaInN LED, we further investigated the effects of the aluminum composition in AlGaN electron-block layer and the QW number on the UV AlGaInN LED. The purpose was with an aim to reduce the electron leakage current and therefore improved the output performance.

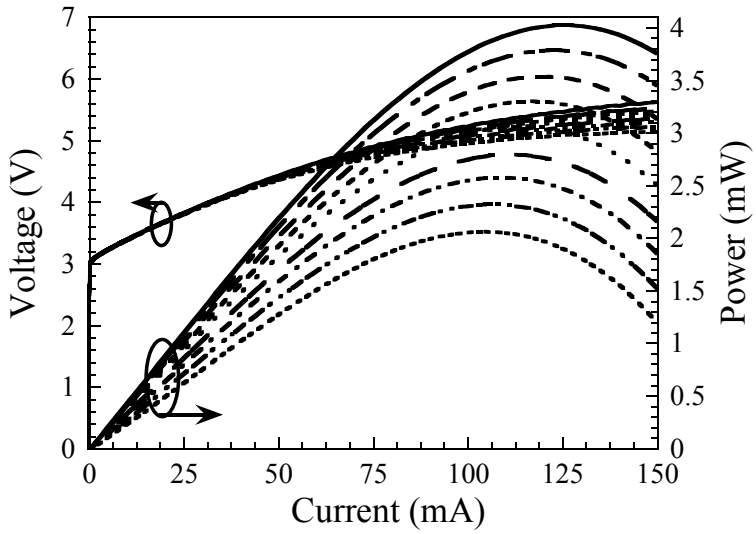

Figure 3.5 Numerical temperature dependent output characteristics of the UV AlGaInN LED.

Several reports had shown that the electron leakage current played an important role in the III-V nitride material due to the large discrepancy of electron and hole effective masses and the low p-type doping concentration [31–36]. For UV LEDs with emission wavelength of 305–365 nm, the Al composition in AlGaN electron-block layer was typically in a range of 23–70% [37–40]. When the emission wavelength was shorter, the Al composition in AlGaN electron-block layer should be increased accordingly because the conduction band offset was decreased and more electrons overflowed to the p-type layers. Figure 3.6 showed the *L-I* characteristics of the UV AlGaInN LED with variant Al compositions in AlGaN electron-block layer when the device temperatures were 300 K and 380 K. It was observed that the output power was enhanced when the Al composition in AlGaN electron-block layer was increased, and the output power at 300 K was limited when the Al composition in AlGaN electron-block layer was higher than 19%. For the UV LED operated at 380 K, increasing the Al composition in AlGaN electron-block layer to be higher than 19% could also effectively prevent the electrons overflow, and the output power remained unchanged when the input current was lower than 110 mA.

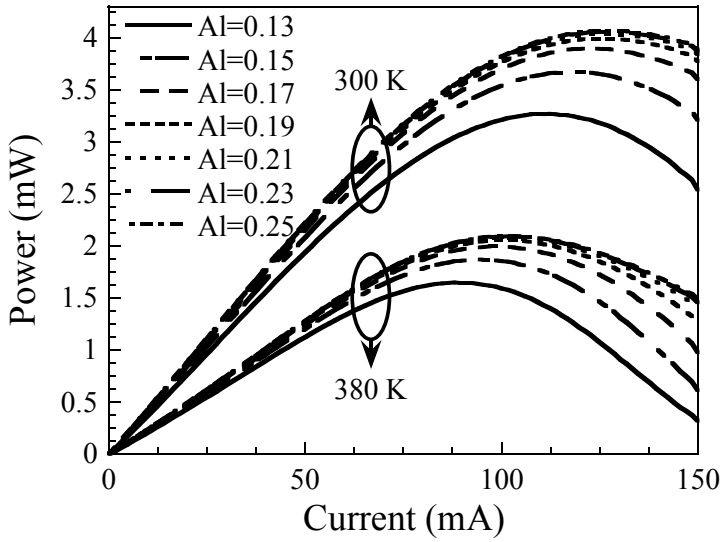

Figure 3.6 *L-I* characteristics of the UV AlGaInN LED with variant Al compositions in AlGaN electron-block layer when the device temperatures were 300 K and 380 K.

Figure 3.7 showed the current efficiency of the UV AlGaInN LED as a function of the input current for variant Al compositions in AlGaN electron-block layer when the device temperature were 300 K and 380 K. Increasing device temperature with decreased internal efficiency was found due to the increase of recombination loss and carrier leakage from the active region. With higher input current and higher device temperature, the electron leakage current and the nonradiative recombination increased which in turn resulted in reduction in current efficiency. The simulated results suggested that the low internal efficiency might be limited by the electron leakage current and the large nonradiative recombination we assumed for the purpose of fitting the experimental output characteristics.

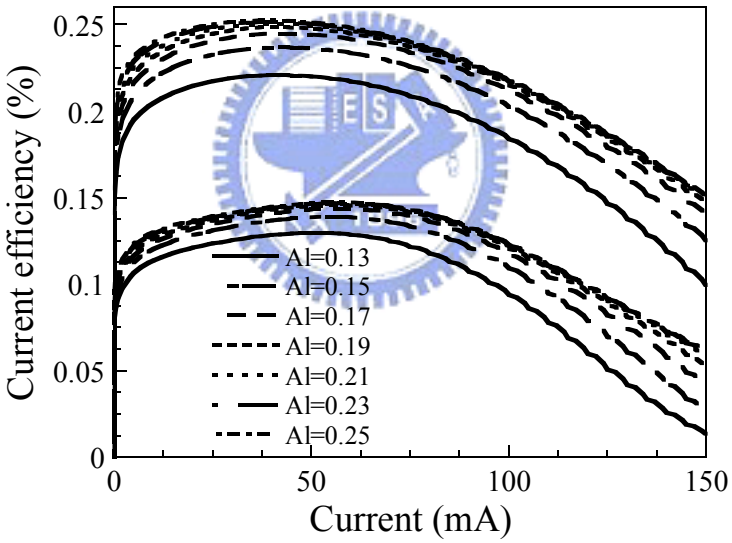

Figure 3.7 Current efficiency of the UV AlGaInN LED as a function of the input current for variant Al compositions in AlGaN electron-block layer when the device temperature were 300 K and 380 K.

To further reduce the electron leakage current and improve the output characteristics, we subsequently investigated the QW number effect on the output characteristics of the UV AlGaInN LED. In this specific study, the Al composition in AlGaN electron-block layer was 19% since our numerical analysis indicated that the relatively better output characteristics were indicated when the Al composition in

AlGaN electron-block layer was 19%. The internal loss value was set and remained unchanged at 1000 m^{-1} when varying the QW number in a range of 1–11, without contemplating the increased defects by increasing QW number during crystal growth. Figure 3.8 showed the *L-I* characteristic of the UV AlGaInN LED with variant QW numbers when the device temperatures were 300 K and 380 K. Figure 3.9 showed the percentage of electron leakage current as a function of the device temperature when the QW number was in a range of 1–11. It could be observed that the lowest output power was obtained when the QW number was one. As the QW number increased, the output power was enhanced respectively; however, we wished to underscore that the output power at lower injection current was decreased as the QW number was more than five, and the hole leakage was much small in the numerical analysis. Nevertheless, more QWs in the active region could undoubtedly reduce the electron leakage current and provide higher output power for higher injection current operation. Thus, numerical results suggested that the optimized QW number in the UV AlGaInN LED was in a range of 5–7.

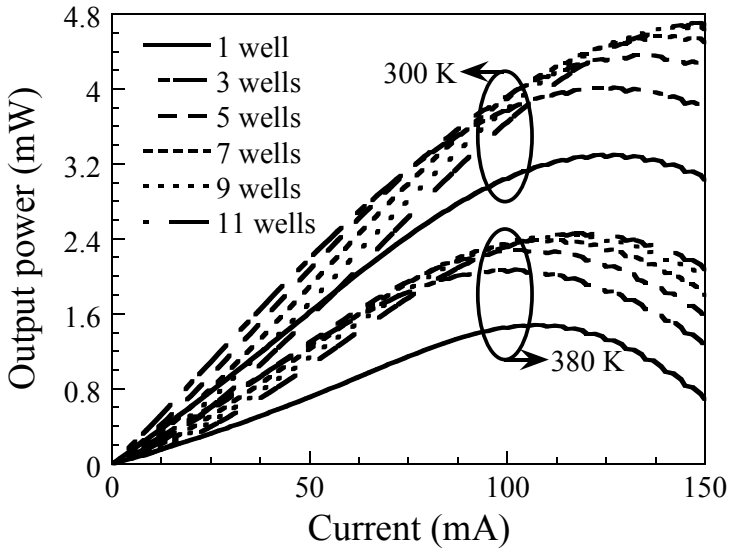

Figure 3.8 *L-I* characteristic of the UV AlGaInN LED with variant QW numbers when the device temperatures were 300 K and 380 K.

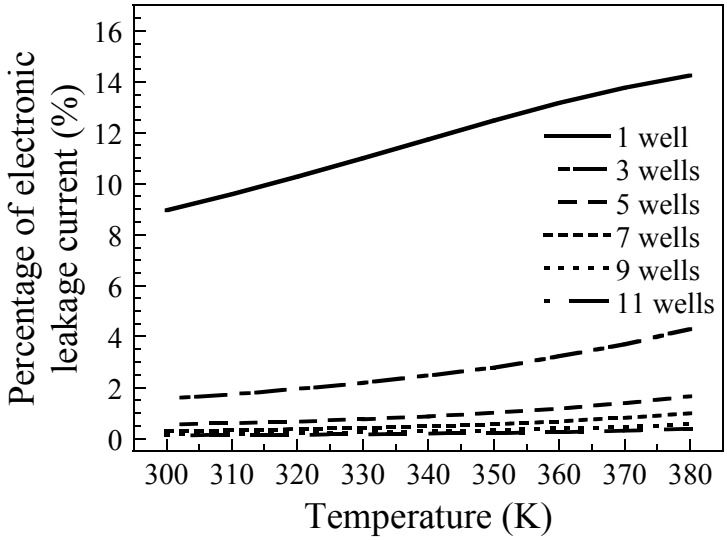

Figure 3.9 Percentage of electron leakage current as a function of the device temperature when the QW number was in a range of 1–11.

3-4 Summary

We had fabricated high-performance 370-nm AlGaInN UV LED. The AlGaInN LED could provide an output power of 0.8 mW at 20 mA with 3.6 V operation voltage and 4 mW at 125 mA under continuous-wave operation. With the help of numerical analysis, we further investigated the effects of the Al composition in AlGaN electron-block layer and the QW number on the 370-nm AlGaInN LED. The results obtained numerically suggested that the 370-nm AlGaInN LED could provide better output characteristics when the Al composition in AlGaN electron-block layer was in a range of 19%–21% and the AlGaInN QW number was in a range of 5–7. The qualitative analysis was significant for improving the output characteristics of the UV LED.

References

[1] M. Yamada, T. Mitani, Y. Nalukawa, S. Shioji, I. Niki, S. Sonobe, K. Deguchi, M. Sano, and T. Mukai, "InGaN-based bear-ultraviolet and blue-light-emitting diodes with high external quantum efficiency using a pattern sapphire substrate and a mesh electrode," *Jpn. J. Appl. Phys.*, vol. 41, pp. L1431–L1433, 2002.

[2] S. Nakamura, M. Senoh, N. Iwasa, S. Nagahama, T. Yamada, and T. Mukai, "Superbright green InGaN single-quantum-well-structure light-emitting diodes," *Jpn. J. Appl. Phys*., vol. 34, pp. L1332–1335, 1995.

[3] T. Mukai, D. Morita, and S. Nakamura, "High-power UV GaInN/AlGaN double-heterostructure LEDs," *J. Cryst. Growth*, vol. 189, pp. 778–, 1998.

[4] T. Mukai, M. Yamada, and S. Nakamura, "Current and temperature dependences of electroluminescence of InGaN-based UV/blue/green light-emitting diodes," *Jpn. J. Appl. Phys*., vol. 37, pp. L1358–L1361, 1998.

[5] T. Mukai, H. Narimatsu, and S. Nakamura, "Amber InGaN-based light-emitting diodes operable at high ambient temperatures," *Jpn. J. Appl. Phys.*, vol. 37, pp. L479–L481, 1998.

[6] M. Yamada, Y. Narukawa, and T. Mukai, "Phosphor free high-luminous-efficiency white light-emitting diodes composed of InGaN multi-quantum well," *Jpn. J. Appl. Phys*., vol. 41, pp. L246–L248, 2002.

[7] V. Adivarahan, W. H. Sun, A. Chitnis, M. Shatalov, S. Wu, H. P. Maruska, and M. Asif Khan, "250 nm AlGaN light-emitting diodes," Appl. Phys. Lett., vol. 85, pp. 2175–2177, 2004.

[8] J. P. Zhang, S. Wu, S. Rai, V. Mandavilli, V. Adivarahan, A. Chitnis, M. Shatalov, and M. Asif. Khan, "AlGaN multiple-quantum-well-based, deep ultraviolet light-emitting diodes with significantly reduced long-wave emission," Appl. Phys. Lett., vol. 83, pp. 3456–3458, 2003.

[9] J. P. Zhang, A. Chitnis, V. Adivarahan, S. Wu, V. Mandavilli, R. Pachipulusu, M. Shatalov, G. Simin, J. W. Yang, and M. Asif Khan, "Milliwatt power deep ultraviolet light-emitting diodes over sapphire with emission at 278 nm," *Appl. Phys. Lett*., vol. 81, pp. 4910–4912, 2002.

[10] H. Hirayama, A. Kinoshita, T. Yamabi, Y. Enomoto, A. Hirata, T. Araki, Y. Nanishi, and Y. Aoyagi, "Marked enhancement of 320–360 nm ultraviolet emission in quaternary $In_xAl_yGa_{1-x-y}N$ with In-segregation effect," *Appl. Phys. Lett*., vol. 80, pp. 207–209, 2002.

[11] V. Adivarahan, S. Wu, J. P. Zhang, A. Chitnis, M. Shatalov, V. Mandavilli, R. Gaska, and M. Asif Khan, "High-efficiency 269-nm emission deep ultraviolet light-wmitting diodes," *Appl. Phys. Lett.*, vol. 84, pp. 4762–4764, 2004.

[12] A. Chitnis, J. Sun, V. Mandavilli, R. Pachipulusu, S. Wu, M. Gaevski, V. Adivarahan, J. P. Zhang, M. Asif Khan, A. Sarua, and M. Kuball, "Self-heating effects at high pump currents in deep ultraviolet light-emitting diodes at 324 nm," *Appl. Phys. Lett*., vol. 81, pp. 3491–3493, 2002.

[13] A. Chitnis, J. P. Zhang, V. Adivarahan, M. Shatalov, S. Wu, R. Pachipulusu, V. Mandavilli, and M. Asif Khan, "Improved performance of 325-nm emission AlGaN ultraviolet light-emitting diodes," *Appl. Phys. Lett*., vol. 82, pp. 2565–2567, 2003.

[14] J. Han and A. V. Nurmikko, "Advances in AlGaInN blue and ultraviolet emitters," *IEEE J. Select. Topics Quantum Electron*., vol. 8, pp. 289–297, 2002.

[15] C.-C. Pan, C.-M. Lee, J.-W. Liu, G.-T. Chen, and J.-I. Chyi, "Luminescence efficiency of InGaN multiple-quantum-well ultraviolet light-emitting diodes," *Appl. Phys. Lett*., vol. 84, pp. 5249–5251, 2004.

[16] A. Yasan, R. McClintock, K. Mayes, D. Shiell, L. Gautero, S. R. Darvish, P. Kung, and M. Razeghi, "4.5 mW operation of AlGaN-based 267 nm deep-ultraviolet light-emitting diodes," *Appl. Phys. Lett*., vol. 83, pp. 4701–4703, 2003.

[17] D. Morita, M. Sano, M. Yamamoto, T. Murayama, S. Nagahama, and T. Mukai, "High output power 365 nm ultraviolet light emitting diode of GaN-free structure," *Jpn. J. Appl. Phys*., vol. 41, pp. L1434–L1436, 2002.

[18] T. Nishida, N. Kobayashi, and T. Ban, "GaN-free transparent ultraviolet light-emitting diodes," *Appl. Phys. Lett*., vol. 82, pp. 1–3, 2003.

[19] V. Zabelin, D. A. Zakheim, and S. A. Gurevich, "Efficiency improvement of AlGaInN LEDs advanced by ray-tracing analysis," *IEEE J. Quantum Electron.*, vol. 40, pp. 1675–1686, 2004.

[20] J. Zhang, J. Yang, G. Simin, M. Shatalov, M. Asif Khana, M. S. Shur, and R. Gaska, "Enhanced luminescence in InGaN multiple quantum wells with quaternary AlInGaN barriers," *Appl. Phys. Lett*., vol. **77**, pp. 2668–2670, 2000.

[21] *APSYS Version 2006.7*, Burnaby, BC, Canada: Crosslight Software, 2006.

[22] I. Vurgaftman and J. R. Meyer, "Band parameters for nitrogen-containing semiconductors," *J. Appl. Phys*., vol. 94, pp. 3675–3696, 2003.

[23] W. Shan, W. Walukiewicz, E. E. Haller, B. D. Little, J. J. Song, M. D. McCluskey, N. M. Johnson, Z. C. Feng, M. Schurman, and R. A. Stall, "Optical properties of $In_xGa_{1-x}N$ alloys grown by metalorganic chemical vapor deposition," *J. Appl. Phys*., vol. 84, pp. 4452–4458, 1998.

[24] G. K. Wachutka, "Rigorous thermodynamic treatment of heat generation and conduction in semiconductor transmodeling," *IEEE Trans.*, vol. CAD-9, pp. 1141–1149, 1990.

[25] A. Marshak and K. van Vilet, "Electrical current in solids with position dependent

band structure," *Solid State Electron.*, vol. 21, pp. 417–427, 1978.

[26] L. Liou, J. Ebel, and C. Huang, "Thermal effects on the characteristics of AlGaAs/GaAs heterojunction bipolar transistors using two dimensional numerical simulation," *IEEE Trans.*, vol. ED-40, pp. 35–43, 1993.

[27] F. Bernardini and V. Fiorentini, "Nonlinear behavior of spontaneous and piezoelectric polarization in III-V nitride alloys," *Phys. Stat. Sol. (a)*, vol. 190, pp. 65–73, 2002.

[28] S. Adachi, "Band gaps and refractive indices of AlGaAsSb, GaInAsSb, and InPAsSb: Key properties for a variety of the 2–4-μm optoelectronic device applications," *J. Appl. Phys*., vol. 61, pp. 4869–4876, 1987.

[29] R. H. Yan, S. W. Corzian, L. A. Coldren, and I. Suemune, "Corrections to the expression for gain in GaAs," *IEEE J. Quantum Electron.*, vol. 26, pp. 213–216, 1990.

[30] J. Piprek, T. Katona, S. P. DenBaars, and S. Li, "3D simulation and analysis of AlGaN/GaN ultraviolet light emitting diodes," *Light-Emitting Diodes: Research, Manufacturing and Applications VIII, Photonics West*, *SPIE Proc*., 5366-59, 2004.

[31] I. Akasaki and H. Amano, *High Brightness Light Emitting Diodes*, G. B. Stringfellow and M. G. Craford, Eds. San Diego, CA: Academic, 1997, vol. 48, ch. 7, p. 357.

[32] H. Morkoc, F. Hamdani, and A. Salvador, *Gallium Nitride (GaN) I*, J. I. Pankove and T. D. Moustakas, Eds. San Diego, CA: Academic, 1998, vol. 50, ch. 8, p. 193.

[33] M. Hansen, J. Piprek, P. M. Pattison, J. S. Speck, S. Nakamura, and S. P. DenBaars, "Higher efficiency InGaN laser diodes with an improved quantum well capping configuration," *Appl. Phys. Lett.*, vol. 81, pp. 4275–4277, 2002.

[34] T. Asano, M. Takeya, T. Tojyo, T. Mizuno, S. Ikeda, K. Shibuya, T. Hino, S. Uchida, and M. Ikeda, "High-power 400-nm-band AlGaInN based laser diodes with low aspect ratio," *Appl. Phys. Lett.*, vol. 80, pp. 3497–3499, 2002.

[35] K. Sasanuma and G. Hatakoshi, "Analysis of current overflow for GaN based laser diodes," IEICE, Japan, Tech. Rep. LQE97-152, 1998.

[36] Y.-K. Kuo and Y.-A. Chang, "Effects of electronic leakage current and inhomogeneous carrier distribution on InGaN quantum-well laser performance," *IEEE J. Quantum Electron.*, vol. 40, pp. 437–444, 2004.

[37] C.-W. Jeon, H. W. Choi, E. Gu, and M. D. Dawson, "High-density matrix-addressable AlInGaN-based 368-nm microarray light-emitting diodes," *IEEE Photon. Technol. Lett.*, vol. 16, pp. 2421–2423, 2004.

[38] D. Morita, M. Sano, M. Yamamoto, M. Nonaka, K. Yasutomo, K. Akaishi, S. Nakahama, and T. Mukai, "Over 200-mW on 365 nm light emitting diode of GaN-free structure," *Phys. Stat. Sol. (a)*, vol. 200, pp.114–117, 2003.

[39] V. Adivarahan, A. Chitinis, J. P. Zhang, M. Shatalov, J. W. Yang, G. Simin, and M. Asif Khan, "Ultraviolet light-emitting diodes at 340 nm using quaternary AlInGaN multiple quantum wells," *Appl. Phys. Lett.*, vol. 79, pp. 4240–4242, 2001.

[40] K. H. Kim, Z. Y. Fan, M. Khizar, M. L. Nakarmi, J. Y. Lin, and H. X. Jiang, "AlGaN-based light-emitting diodes grown on AlN epilayers," *Appl. Phys. Lett.*, vol. 85, pp. 4777–4779, 2004.

Chapter 4 Temperature Insensitive 660-nm RCLED

RCLEDs are promising light emitters when compared to typical light emitting diode for the application of data communication due to they provide higher extraction efficiency, improved spectral purity, highly directional light output, less chromatic dispersion and improved modulation bandwidth [1]. As compared with vertical-cavity surface-emitting lasers, the epitaxial complexity of RCLED structure is reduced since the reflectivity of upper DBRs has to be less than 90%, and thus the RCLEDs provide thresholdless operation, less temperature dependence and better fabrication reliability. RCLEDs with visible red emission are suitable candidates for short-distance data communication applications due to a minimum attenuation loss (0.15 dB/m) at 650 nm in the polymethyl methacrylate plastic optical fibers (PMMA POFs) [2]. Recently, the application of POFs has been extended to the automotive industry, such as MOST, which needs to carrier 50–250 Mbps of data over POFs. In a RCLED, the Fabry-Pérot cavity, sandwiched between upper and lower DBRs, is generally designed with 1-λ thickness, and the QWs are embedded at the antinode of the standing wave cavity mode. The gain cavity detuning ($\Delta\lambda_{detuning}=\lambda_{FP}-\lambda_{qw}$) is often designed to be positive to have a higher optical gain. Most importantly, to obtain better characteristics under high temperature operation the careful design of $\Delta\lambda_{detuning}$ is required because the maximal modal gain red-shifts and matches the resonance dip as the device temperature increases. Hild *et al*. had reported the RCLEDs were less temperature sensitive over 15–75 ºC temperature range by a large gain cavity detuning [3]. However, the high temperature output performance was still restricted by carrier leakage [3]–[5]. In the field of 650-nm RCLEDs, the researchers had reported a high output power of 8.4 mW operated at 120 mA with 202 μm device diameter [6], a peak external quantum efficiency of 10.2% for large area device [7], low voltage operation [8], a maximum emission in the normal

direction [9], and high modulation bandwidth [10]–[13].

These efforts have made the RCLEDs to have better output characteristics under room temperature operation and improving modulation bandwidth; however, it needs to be mentioned that substantial work is still necessitated with the aim of stabilizing output performance in RCLEDs with elevated device temperature and injection current. In this chapter, the design and fabrication of temperature insensitive InGaP/InGaAlP RCLEDs by means of widening the resonant cavity to 3 λ, where the number of QWs was increased by a factor of three and the QWs were separated into three parts to reduce electronic leakage current, were reported. As compared with conventional RCLED of 1-λ-cavity design, the temperature dependent light output and voltage (L-I-V) characteristics, 3 dB modulation bandwidths, and far-field patterns are characterized and discussed. To further investigate the device physics of the RCLED devices, a theoretical analysis of the structure dependent RCLED output characteristics was presented. An advanced physical model of semiconductor devices (APSYS) program [14] was utilized for a main purpose of specifying the electronic leakage current.

4-1 Fabricated device characteristics

The RCLED structures in the specific study were grown by a low pressure (50 torr) Veeco D180 metal-organic chemical vapor deposition (MOCVD) system on n-type GaAs substrates. Methyl-organometallics, phosphine, and arsine were used as the sources for epitaxy. SiH_4, CBr_4, and DEZn were the n- and p-type dopants. A schematic plot of device structures was shown in Figure 4.1. Two structures were prepared, in which the bottom DBR was identically comprised of 35 pairs of *n*-type quarter-wave $Al_{0.95}Ga_{0.05}As/Al_{0.5}Ga_{0.5}As$ layers for both devices to provide a ~99% reflectivity, and the top DBRs was identically comprised of 7 pairs of *p*-type $Al_{0.95}Ga_{0.05}As/Al_{0.5}Ga_{0.5}As$ layers.

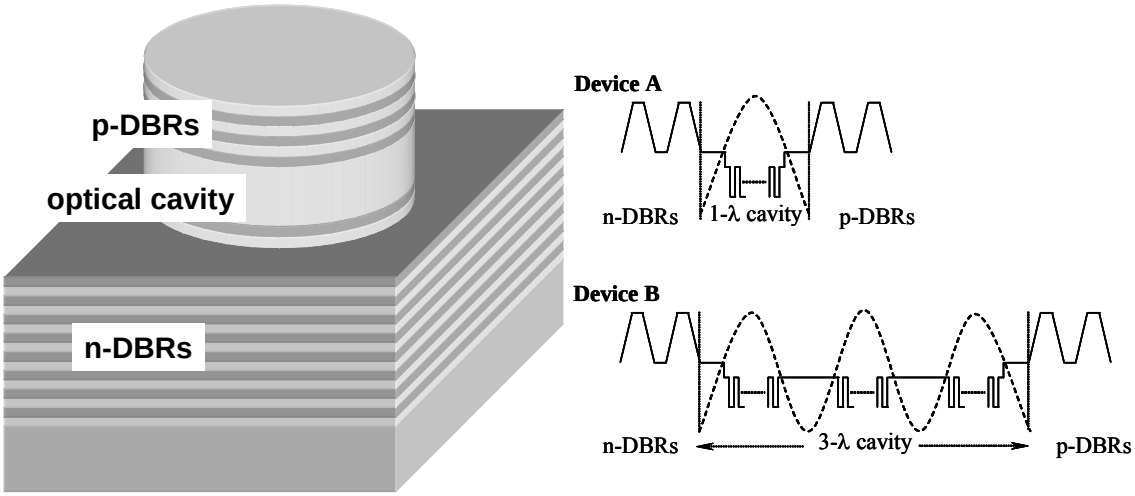

Figure 4.1 A schematic plot of device structure. Device A was designed with a conventional 1-λ resonant cavity. Device B was designed to have a 3-λ resonant cavity, while the number of QWs was tripled and separated into three parts.

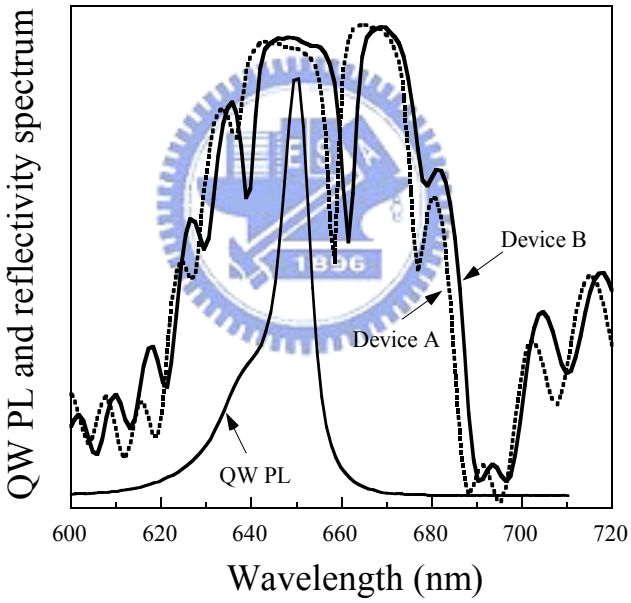

Figure 4.2 Spectra of QW photoluminescence and reflectivity of devices A and B.

A separate-confinement-heterostructure strained multiple QWs active region, which contained $In_{0.52}Ga_{0.48}P$ wells and $In_{0.5}(Ga_{0.5}Al_{0.5})_{0.5}P$ barriers, and $In_{0.5}(Ga_{0.3}Al_{0.7})_{0.5}P$ cladding layers formed the resonant cavity. For device A, the cavity was standardized to 1 λ, and the cavity for device B was widened to 3 λ and the number of QWs was tripled. The $\Delta\lambda_{detuning}$ was designed to be 8~10 nm, as could be found in Figure 4.2. The doping levels of *n*- and *p*-type DBRs, determined from ECV

measurement, were 2×10^{18} and 4×10^{18} cm^{-3}. After epitaxial growth, standard fabrication processes, including photolithography, implantation, metallization, and bonding techniques, were used to fabricate the devices with surface emission. The light extraction window of both devices in this study was 80 μm in diameter. The RCLED chips were mounted onto TO-46 headers and the chip size was in 250×250 μm^2 square.

The direct current characteristics of RCLEDs were measured using a Keithly 238 current source, a Newport 1835C power meter module, and an Advantec optical spectrum analyzer (OSA) with a 0.1 nm spectral resolution. As a result of Joule heating, the peak emission wavelength increased with increased bias current at a redshift of 0.083 nm/mA for device A, 0.082 nm/mA for device B, and the devices exhibited a peak of 656.8 and 659.4 nm when the bias current was 40 mA, respectively. Temperature dependent L-I-V characteristics of devices A and B are shown in Figure 4.3. The highly C-doped p-type DBRs and high quality ohmic contacts resulted in a low operating voltage of 2.1 V at a current of 20 mA in device A, while the thicker undoped cavity in device B gave a higher voltage of 2.37 V at 20 mA. An output power of 1.9 mW in device A at 20 mA under RT operation was achieved, and it reached to a maximum of 3.1 mW output when the device was biased at 57 mA. For device B, even though the output power at low current was not higher than that in device A, the output characteristic was stable, which indicated that the temperature effect on device B was much less sensitive. The power variation between 25 and 95 ºC for devices A and B at 20 mA were approximately -2.1 and -0.6 dB. We supposed that the improved stable output performance under high current injection and high temperature operation in device B was from the increased number of QWs that decreased the carrier leakage.

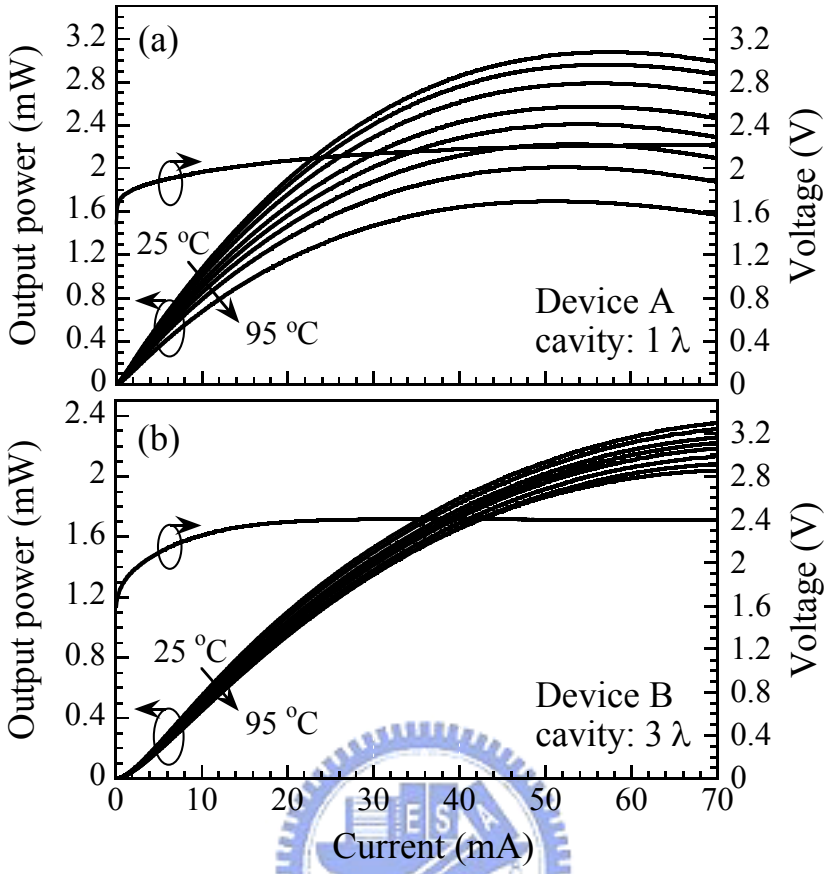

Figure 4.3 Temperature dependent L-I-V characteristic of the fabricated (a) device A and (b) device B. The curve was obtained in a device temperature range of 25–95 ºC.

The temperature dependent external quantum efficiency (η_{ext}) normalized to the value obtained at 20 mA was depicted in Figure 4.4. The inset showed the η_{ext} value versus current at RT. For device A, a maximum η_{ext} value of 6% was achieved when the device was biased at 5.8 mA. As shown in previous studies, the highest η_{ext} value of RCLEDs was often obtained at a low current level, typically less than 10 mA, and consequently decreased at higher current levels by internal heating effect. In red emitting devices, this phenomenon was more serious because the conduction band offset value in InGaP/InGaAlP material is relatively low compared to the InGaN/GaN and AlGaAs/GaAs materials [15, 16]. The increased device temperature at higher current level would induce more leakage current, resulting in less radiative recombination, and therefore decreased the output performance. To reduce the induced

leakage current at high current level injection and under high temperature operation, the resonant cavity in device B was increased to 3 λ and the number of QWs was tripled simultaneously, which was a direct way to confine more carriers in the QWs of the resonant cavity. This approach should be effective since the normalized η_{ext} value for device B dropped only 14% with elevated device temperature to 95 ºC. In addition, the decrease of η_{ext} at high current levels, shown in the inset of Figure 4.4, was also less pronounced. The lower η_{ext} for device B than for device A might be due to the number of QWs was tripled that induced more absorption in QWs, and a less optimally tuned cavity due to the thicker emission region.

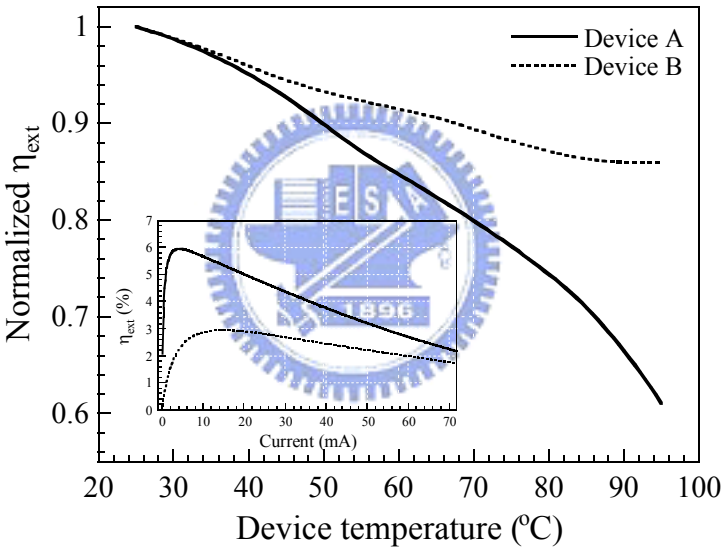

Figure 4.4 Normalized external quantum efficiency (η_{ext}) value obtained at 20 mA with elevated device temperature from 25 to 95 ºC. The inset was the η_{ext} value versus current at room temperature for both devices.

Dynamic properties of the RCLED devices were studied by using a calibrated vector network analyzer (Agilent 8720ES) and 50-μm multimode optical fiber connected to a Si photodetector. A light extraction window diameter of 80 μm was used for POF-based communication. However, there is a trade-off between light extraction output power and small signal 3 dB frequency bandwidth ($f_{-3\ dB}$). A smaller light extraction window diameter will bring on a lower capacitance, resulting in the

decreased RC time constant, but a weak output power performance. The measured $f_{-3\ dB}$ frequency bandwidth for devices A and B as a function of bias current were shown in Figure 4.5. In our devices, the $f_{-3\ dB}$ value was found to increase with increased bias current with a slope of 0.44 MHz/mA for device A, 0.2 MHz/mA for device B, and achieved to a maximum of 116, and 87 MHz at 70 mA, respectively. The lower $f_{-3\ dB}$ value for device B than for device A might be attributed to that the number of QWs is tripled. Hence, the current density in each QW of the device B may be relatively lower than that of the device A. In addition, the thicker resonant cavity might cause the increase of series resistance that reduced the $f_{-3\ dB}$ value. Further minimization of the capacitance at the pn junction and adjustment of the bonding pad to reduce the parasitic capacitance will be required.

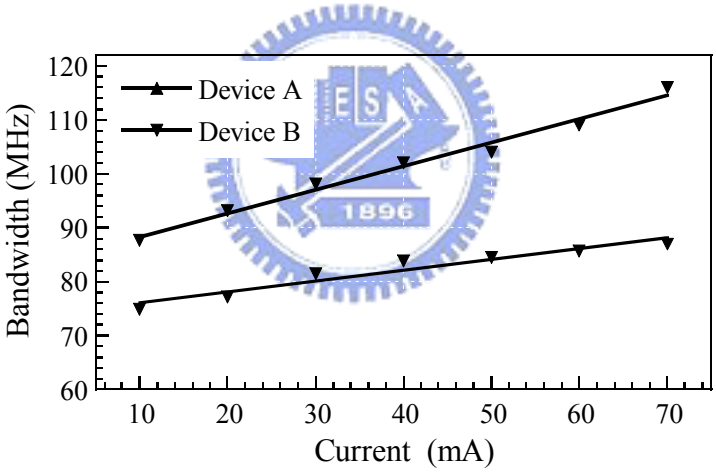

Figure 4.5 $f_{-3\ dB}$ frequency bandwidth for devices A and B as a function of bias current. The current aperture for both devices A and B was 80 μm in diameter.

The evolution of far field patterns under room temperature with increased bias current of 10–50 mA was shown in Figure 4.6. For device A, the emission took place at the angle of ±33º, and the angle became ±20º when the device was biased at 50 mA. Narrowing far field angle was undoubtedly required under the consideration of fiber coupling efficiency. In conventional 1-λ-cavity RCLEDs, while increasing bias current could narrow the far field emission angle, the output power often rolled over at high current level injection. By widening the resonant cavity to 3 λ, we found that the angle

of the lobe was zero and the small divergence angle of the far field pattern remained almost unchanged over the entire measured bias current range.

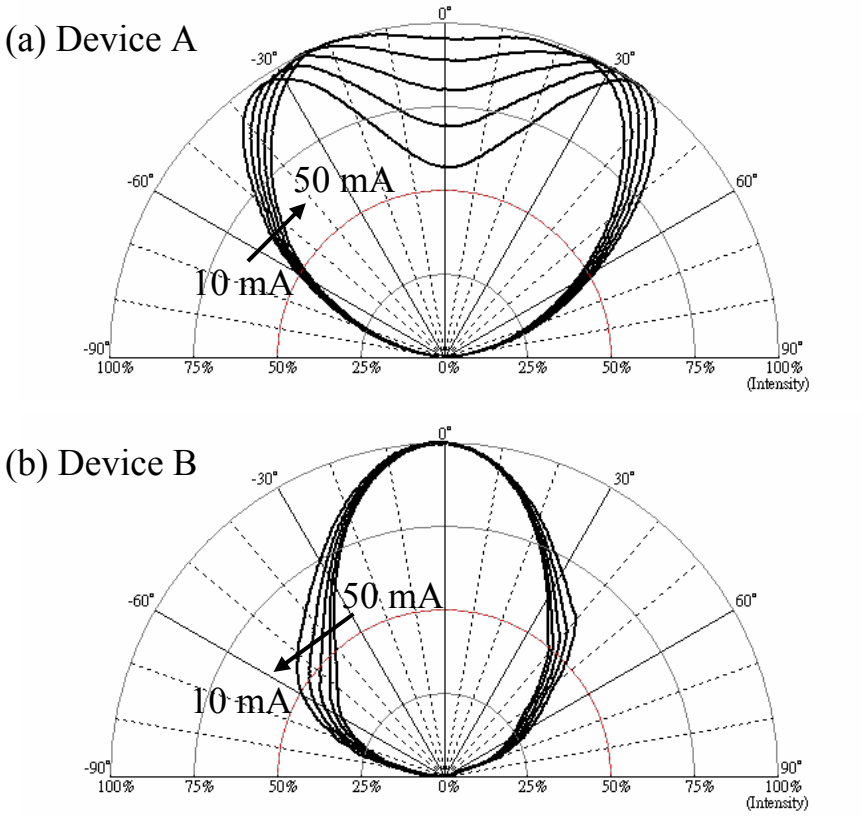

Figure 4.6 Evolution of far field patterns for both devices under room temperature operation with increased bias current of 10–50 mA. The slightly unsymmetrical patterns could be attributed to the TO package.

4-2 Theoretical analysis

It is universally known that qualitatively theoretical analysis can provide a way to realize the physics of the optoelectronic semiconductor devices. The numerical simulation in this study was executed with the use of an advanced physical model of semiconductor devices (APSYS) [14], which solved the Poisson's equation, three-dimensional drift diffusion and photon rate equations, and scalar wave equation inside RCLEDs. In the optical mode model, all modes were treated as possible since they all contribute to the non-coherent spontaneous emission power [17]. Photon recycling effect was rigorously taken into account by accurately determinate photon

power density. In the gain model, material gain and loss for both bulk and QW as functions of wavelength and carrier density were computed. For the numerical simulation, based on the *k·p* theory, a Hamiltonian matrix of the Luttinger-Kohn type and an envelope function approximation were used to solve the QW subband structures [18]. Except for the unstrained bandgap energies, in order to obtain the numerical parameters required for *k·p* calculations for the InGaAlP materials, a linear interpolation among InP, GaP, and AlP was utilized in this study [19], [20]. The material parameters of the binary semiconductors used in this study were taken from the values reported by Vurgaftman *et al.* [21]. The formula for the calculation of unstrained InGaAlP bandgap energies were considered in accordance with the model provided by Mbaye *et al.* [22]. The temperature dependent bandgap energies of the relevant binary semiconductors were calculated using the commonly employed Varshni formula and the Varshni parameters were taken from Ref. 22. The conduction to valence band offset ratio was chosen as 65:35 according to the latest measurement results [23]. The spontaneous emission rate, with the valence-band-mixing effect being taken into account, could be expressed by [24]

$$r_{sp}(E) = \frac{2nq^2E}{\pi^2\hbar^2c^3\varepsilon_0 m_0^2 L_z} \sum_{n,m} \int_0^\infty \frac{k_t M_{nm}(k_t)\Gamma/(2\pi)}{\left(E_{cn}(k_t) - E_{kpm}(k_t) - E\right)^2 + (\Gamma/2)^2} \times f_c^n(1 - f_v^m)dk_t \quad (4.1)$$

where q was the free electron charge, $\hbar$ was the reduced Planck's constant, n was the index of refraction, ε_0 was the free-space dielectric constant, c was the speed of light, L_z was the thickness of QW, E was the photon energy, $M_{nm}(k_t)$ was the momentum matrix element in the strained QW, $\Gamma = \hbar/\tau$ was the broadening due to intraband scattering relaxation time τ, E_{cn} was the n^{th} conduction subband, E_{kpm} was the m^{th} valence subband from the *k·p* calculation, f_c^n and f_v^m were the Fermi functions for the conduction band states and the valence band states respectively. The indices n and m denoted the

electron states in the conduction band and the heavy hole (light hole) subband states in the valence band. To account for the broadening due to scattering, it was assumed that τ = 0.1 ps [25]–[27] during the calculations.

The effect of self heating has a major impact on the performance of RCLED devices. The increased internal temperature caused by current injection limits the maximum output power due to the increase of nonradiative carrier recombination, the spread of gain spectrum, and the temperature-induced gain-cavity misalignment at higher operation current. For the treatment of device heating, the thermoelectric power and thermal current induced by temperature gradient were solved by utilizing the methods provided by Wachutka *et al.* [28]. Various heat sources, including Joule heat, generation/recombination heat, Thomson heat and Peltier heat, were taken into account in this specific study. The random distribution of alloy atoms in quaternary AlGaInP compounds caused strong alloy scattering of phonons, which lead to a significant reduction in the thermal conductivity. The thermal conductivity of quaternary alloys of the type $AB_xC_yD_{1-x-y}$ could be estimated from binary values using [29]

$$\frac{1}{\kappa(x,y)} = \frac{x}{\kappa_{AB}} + \frac{y}{\kappa_{AC}} + \frac{1-x-y}{\kappa_{AD}} + xyC_{ABC} + x(1-x-y)C_{ABD} + y(1-x-y)C_{ACD} \tag{4.2}$$

with the empirical bowing parameters C_{ABC}, C_{ABD}, and C_{ACD}. In our calculation, the thermal conductivities of the binary AlP, GaP, and InP were 1.3, 0.77, and 0.68 W/Kcm, respectively [29], [30]. The empirical bowing parameters of AlGaP, AlInP, and GaInP were 30, 77, and 19.9 Kcm/W, respectively [29], [30].

The calculations of carrier capture and escape from the QWs are considered in accordance with the model provided by Romero *et al.* [31]. As for the parameter of refractive index, Adachi model is employed to calculate the refractive index values of the AlGaInP materials [32]. More description about the physical models utilized in APSYS simulation program, which is a useful tool to access new designs or to optimize

existing devices after calibrating with specific materials, can be found in [29], [33], [34]. During numerical simulation, the device structures, including the active regions and DBRs were considered in accordance with the experimental device structures. Device A (1-λ cavity) and device B (3-λ cavity) were numerically analyzed for investigating the internal physical mechanism. Figure 4.7 showed the vertical profile of refractive index and optical intensity for device A [Figure 4.7(a)] and device B [Figure 4.7(b)]. The position of QWs was designed to be located at the peak of optical standing wave. This design can enhance the spontaneous emission and photon recycling in microcavity-based system [35], [36].

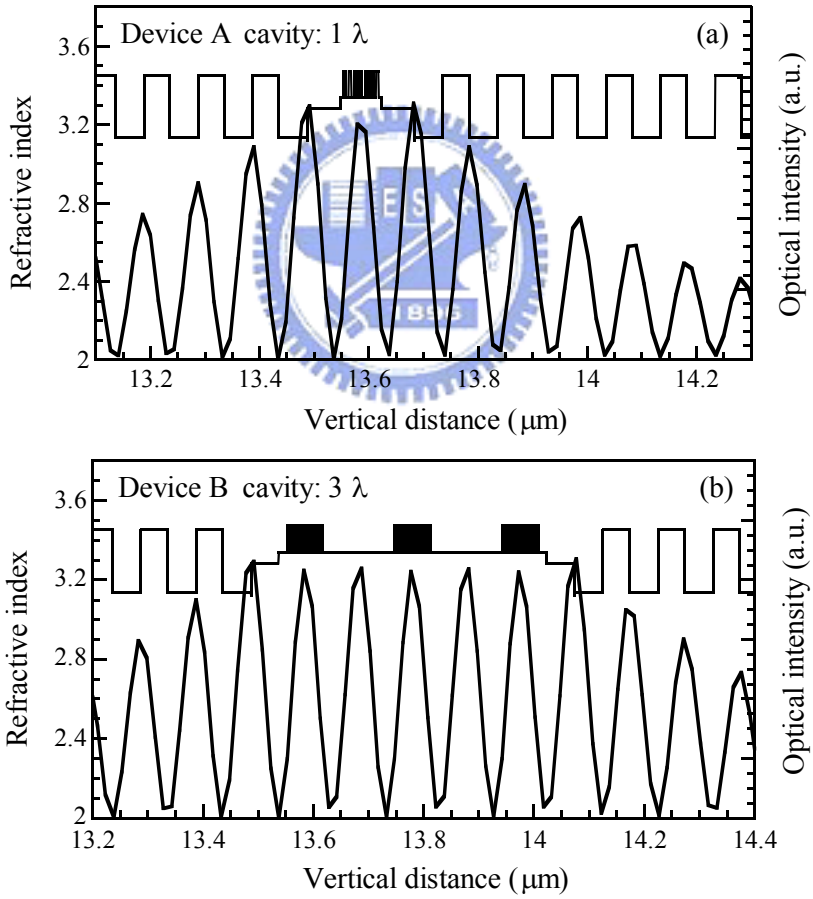

Figure 4.7 Vertical profile of refractive index and optical intensity for (a) device A and (b) device B.

The simulation results of temperature dependent L-I characteristics of devices A and B were shown in Figure 4.8. It was clearly seen that the results obtained

numerically were approximately fit in with the experiments, and the same tendency that device B provided a relatively temperature-insensitive L-I characteristics was obtained. For the design of device B, the positions of the twenty one pairs of QWs were separated into three parts, and each period of QWs were also individually located at the peak of the optical standing wave. Basically, a good overlap between the optical standing wave and the position of QWs could provide a better emission output performance. However, it could not be prevented that an external optical loss occurred when device B was biased at low input current. Because the distribution of electrons and holes in the special QW regions was inhomogeneous, the QWs that did not contribute spontaneous emission might absorb photons. Thus, the output power in device B could not be comparable to device A. The optimal design of position and number of QWs in the 3-λ cavity might be important for obtaining better temperature dependent L-I characteristics and large output power.

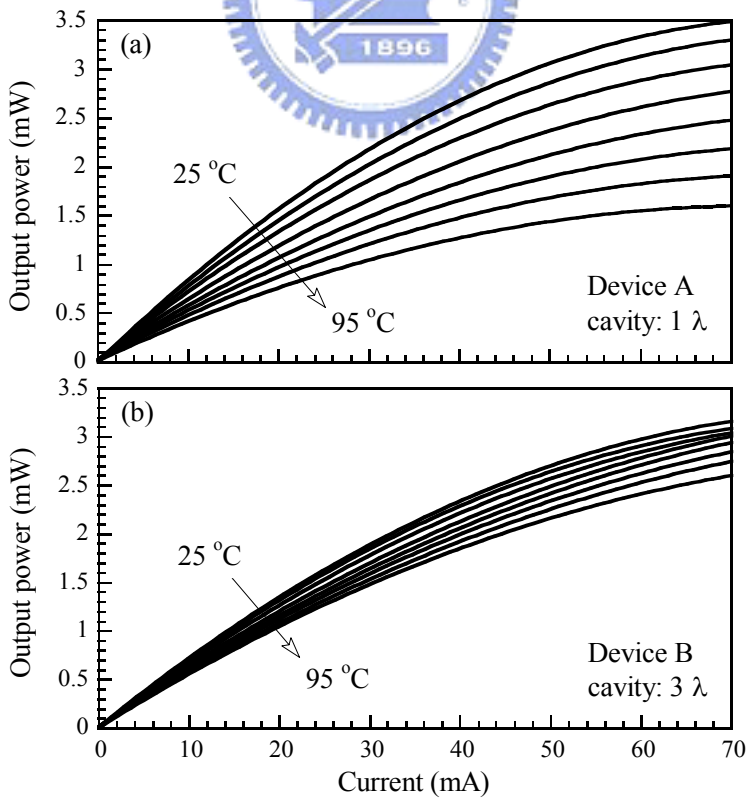

Figure 4.8 Numerical results of temperature dependent L-I characteristics of devices A and B.

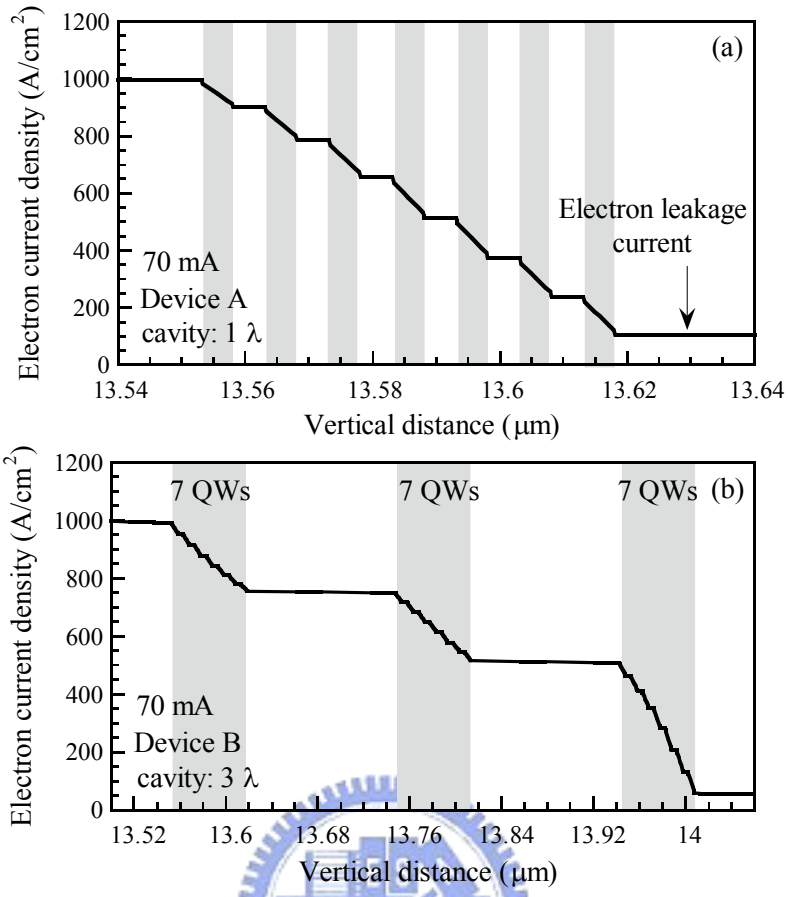

Figure 4.9 Vertical electron current distribution at 70 mA injection current within the active regions of devices A and B.

To further investigated the effects of electronic leakage current on RCLED performance, the vertical electron current distributions at 70 mA injection current within the active regions of devices A and B were plotted in Figure 4.9. The positions of QWs are marked with gray areas. The left-hand side of the figure was the n-side of the device. The electron current was injected from n-type layers into quantum wells and recombined with holes in quantum wells; therefore, the electron current density was reduced in the quantum wells closed to the right-side (p-side) of the figure. Electron current which overflows through quantum wells was viewed as leakage current, while in this study, the percentage of electronic leakage current was defined as the ratio of electronic leakage current to the total current pouring into the QW active region. For InGaAlP materials, since the limited barrier height in the InGaP/InGaAlP quantum-well

structures and larger thermal resistivity due to the large mass difference between gallium and indium, the electronic leakage current was more due to the poor electron confinement and the serious self-heating effect. For device A, as indicated in Figure 4.9(a), the electronic leakage current was observed more when compared to device B. Less electronic leakage current was found in device B, and we supposed that it was as a result of tripling the QW numbers to be twenty one pairs. Increasing more QWs in the resonant cavity was found to beneficially reduce the electronic leakage current.

Figure 4.10 depicted the percentage of electronic leakage current as a function of the bias current in devices A and B when the device temperatures were 25 and 95 °C, respectively. When the devices were at an input current range of 0–75 mA, the percentage of electron leakage current of device A was about twice larger than that of device B. As the device temperature was increased to 95 °C, the electronic leakage current in device A became more serious with increased bias current. In the mean time, it was noteworthy that the percentage of electronic leakage current in device B was apparently reduced. Therefore, the temperature dependent L-I characteristics in device B showed more stable.

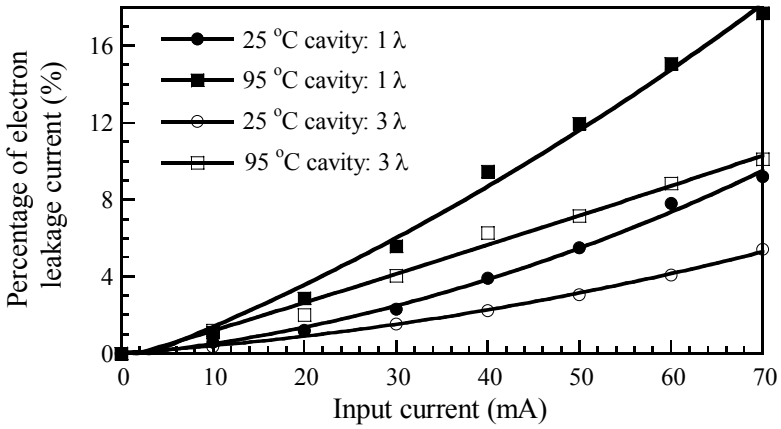

Figure 4.10 Percentage of electronic leakage current as a function of the bias current in devices A and B when the device temperatures were 25 and 95 °C.

4-3 Summary

In summary, we have fabricated visible InGaP/InGaAlP RCLEDs with low temperature sensitivity of the output performance. By widening the resonant cavity to 3 λ, the degree of power variation was apparently reduced to -0.6 dB, and the η_{ext} value dropped only 14.1% when the device was biased at 20 mA with elevated temperature from 25 to 95 ºC. The current dependent far field patterns also showed that the emission of the 3-λ RCLEDs always took place perfectly in the normal direction. The results indicate the 3-λ RCLEDs can provide stable output characteristics and are suitable for data communication applications. The results obtained numerically also suggested that the temperature insensitive light output characteristics of the 3-λ RCLED was due to the reduced electronic leakage current by tripling the QW numbers.

References

[1] E. Fred Schubert, "*Light-Emitting Diodes*," 2nd Cambridge New York: Cambridge University Press, 2006, ch 15.

[2] T. Ishigure, M. Satoh, O. Takanashi, E. Nihei, T. Nyu, S. Yamazaki, and Y. Koike, "Formation of the refractive index profile in the graded index polymer optical fiber for gigabit data transmission," *J. Lightw. Technol.*, vol. 15, no. 11, pp. 2095–2100, 1997.

[3] K. Hild, T. E. Sale, T. J. C. Hosea, M. Hirotana, Y. Mizuno, and T. Kato, "Spectral and thermal properties of red AlGaInP RCLEDs for polymer optical fibra applications," *IEE Proc.-Optoelectron.*, vol. 148, no. 5/6, pp. 220–224, 2001.

[4] A. I. Onischenko, T. E. Sale, E. P. O'Reilly, A. R. Adams, S. M. Pinches, J. E. F. Frost, and J. Woodhead, *IEE Proc.-Optoelectron.*, vol. 147, no. 1, pp. 15–21, 2000.

[5] K. Streubel, N. Linder, R. Wirth, and A. Jaeger, "High brightness AlGaInP light-emitting diodes," *IEEE J. Select. Topics Quantum Electron.*, vol. 8, no. 2, pp. 321–332, 2002.

[6] K. Streubel, U. Helin, V. Oskarsson, E. Bäcklin, and Å Johansson, "High brightness visible (660 nm) resonant-cavity light-emitting diode," *IEEE Photon. Technol. Lett*., vol. 10, no. 12, pp. 1685–1687, 1998.

[7] R. Wirth, C. Karnutsch, S. Kugler, and K. Streubel, "High efficency resonant-cavity LEDs emitting at 650 nm," *IEEE Photon. Technol. Lett*., vol. 13, no. 5, pp. 421–423, 2001.

[8] J. W. Gray, Y. S. Jalili, P. N. Stavrinou, M. Whitehead, G. Parry, A. Joel, R. Robjohn, R. Petrie, S. Hunjan, P. Gong, and G. Duggan, "High-efficiency, low voltage resonant-cavity light-emitting diodes operating around 650nm," *Electron. Lett.*, vol. 36, no. 20, pp. 1730–1731, 2000.

[9] R. Joray, M. Ilegems, Ross P. Stanley, W. Schmid, R. Butendeich, R. Wirth, A. Jaeger, and K. Streubel, "Far-field radiation pattern of red emitting thin-film resonant cavity LEDs," *IEEE Photon. Technol. Lett*., vol. 18, no. 9, pp. 1502–1504, 2006.

[10] P. Sipilä, M. Saarinen, M. Guina, V. Vilokkinen, M. Toivonen, and M. Pessa, "Temperature behaviour of resonant cavity light-emitting diodes at 650 nm," *Semicond. Sci. Technol.*, vol. 15, pp. 418–421, 2000.

[11] E. F. Schubert, N. E. J. Hunt, Roger J. Malik, M. Micovic, and David. L. Miller, "Temperature and modulation characteristics of resonant-cavity light-emitting diodes," *J. Lightw. Technol.*, vol. 14, no. 7, pp. 1721–1729, 1996.

[12] M. Guina, S. Orsila, M. Dumitrescu, M. Saarinen, P. Sipilä, V. Vilokkinen, B. Roycroft, P. Uusimaa, M. Toivonen, and M. Pessa, "Light-emitting diode emitting

at 650 nm with 200-MHz small-signal modulation bandwidth," *IEEE Photon. Technol. Lett*., vol. 12, no. 7, pp. 786–788, 2000.

[13] C. -L. Tsai, C. -W. Ho, C. -Y. Huang, F. -M. Lee, M. -C. Wu, H. -L. Wang, S. -C. Ko, W. -J. Ho, J. Huang, and J. R. Deng, "Fabrication and characterization of 650 nm resonant-cavity light-emitting diodes," *J. Vac. Sci. Technol. B*, vol. 22, no. 5, pp. 2518–2521, 2004.

[14] *APSYS Version 2006.7*, Burnaby, BC, Canada: Crosslight Software, 2006.

[15] D. P. Bour, R. S. Geels, D. W. Treat, D. L. Paoli, F. Ponce, R. L. Thomton, B. S. Krusor, R. D. Bringans, and D. F. Welch, "Strained $Ga_xIn_{1-x}P/(AlGa)_{0.5}In_{0.5}P$ heterostructures and quantum-well laser diodes," *IEEE J. Quantum Electron.*, vol. 30, no. 2, pp. 593–607, 1994.

[16] K. Interholzinger, D. Patel, C. S. Menoni, P. Thiagarajan, Gary Y. Robinson, and Julie E. Fouquet, "Strain-induced modifications of the band structure of $In_xGa_{1-x}P–In_{0.5}Al_{0.5}P$ multiple quantum wells," *IEEE J. Quantum Electron.*, vol. 34, no. 1, pp. 93–100, 1993.

[17] C. H. Henry, "Theory of spontaneous emission noise in open resonators and its application to lasers and optical amplifiers," *IEEE J. Lightware Technol.*, vol. LT-4, pp. 288–297, 1986.

[18] Y.-P. Chao and S. L. Chuang, "Spin-orbit-coupling effects on the valence-band structure of strained semiconductor quantum wells," *Phys. Rev. B*, vol. 46, pp. 4110–4122, 1992.

[19] J. Minch, S. H. Park, T. Keating, and S. L. Chuang, "Theory and experiment of $In_{1-x}Ga_xAs_yP_{1-y}$ and $In_{1-x-y}Ga_xAl_yAs$ long-wavelength strained quantum-well lasers," *IEEE J. Quantum Electron.*, vol. 35, pp. 771–782, 1999.

[20] S. T. Yen and C.-P. Lee, "Theoretical analysis of 630-nm band GaInP–AlGaInP strained quantum-well lasers considering continuum states," *IEEE J. Quantum Electron.*, vol. 33, pp. 443–456, 1997.

[21] I. Vurgaftman, J. R. Meyer, and L. R. Ram-Mohan, "Band parameters for III-V compound semiconductors and their alloys," *J. Appl. Phys.*, vol. 89, pp. 5815–5875, 2001.

[22] A. A. Mbaye, C. Verié, and F. Aymerich, "Electronic structure of trimetallic III-V alloys: the Al1-x-zGaxInzP system," *Phys. Rev. B*, vol. 29, pp. 3756–3758, 1984.

[23] K. Interholzinger, D. Patel, C. S. Menoni, P. Thiagarajan, G. Y. Robinson, and J. E. Fouquet, "Strain-induced modifications of the band structure of $In_xGa_{1-x}P–In_{0.5}Al_{0.5}P$ multiple quantum wells," *IEEE J. Quantum Electron.*, vol. 34, pp. 93–100, 1998.

[24] S. L. Chuang, *Physics of Optoelectronic Devices*. John Wiley & Sonc, Ind., New York, (1995).

[25] S. Kamiyama, T. Uenoyama, M. Mannoh, Y. Ban, and K. Ohnaka, "Analysis of GaInP/AlGaInP compressive strained multiple-quantum-well laser," *IEEE J. Quantum Electron.*, vol. 30, pp. 1363–1369, 1994.

[26] S. Kamiyama, T. Uenoyama, M. Mannoh, and K. Ohnaka, "Theoretical studies of GaInP–AlGaInP strained quantum-well lasers including spin-orbit split-off band effect," *IEEE J. Quantum Electron.*, vol. 31, pp. 1409–1417, 1995.

[27] S. Kamiyama, T. Uenoyama, M. Mannoh, Y. Ban, and K. Ohnaka, "Theoretical analysis of valence subband structures and optical gain of GaInP/AlGaInP compressive strained-quantum wells," *IEEE Photon. Technol. Lett.*, vol. 4, pp. 439–441, 1993.

[28] G. K. Wachutka, "Rigorous thermodynamic treatment of heat generation and conduction in semiconductor device modeling," *IEEE Trans. Comput.-Aided Des. Integr. Circuits Syst.*, vol. 9, pp. 1141–1149, 1990.

[29] J. Piprek, *Semiconductor Optoelectronic Devices: Introduction to Physics and Simulation.* San Diego, CA: Academic, 2003.

[30] W. Nakwaski, "Thermal conductivity of binary, ternary, and quaternary III-V compounds," *J. Appl. Phys.*, vol. 64, pp. 159–166, 1988.

[31] B. Romero, J. Arias, I. Esquivias, and M. Cada, "Simple model for calculating the ratio of the carrier capture and escape times in quantum-well lasers," *Appl. Phys. Lett.*, vol. 76, pp. 1504–1506, 2000.

[32] H. Kato, S. Adachi, H. Nakanishi, and K. Ohtsuka, "Optical properties of $(Al_xGa_{1-x})_{0.5}In_{0.5}P$ quaternary alloys," *Jpn. J. Appl. Phys.*, vol. 33, pp. 186–192, 1994.

[33] J. Piprek and S. Li, "GaN-based light emitting diodes," *Optoelectronic Devices: Advanced Simulation and Analysis*. Springer, 2005.

[34] Yen-Kuang Kuo, Sheng-Horng Yen, and Jun-Rong Chen, "Ultraviolet light-emitting diodes," *Nitride Semiconductor Devices: Principles and Simulation*. WILEY-VCH Verlag GmbH & Co. KGaA, 2007.

[35] G. Björk, S. Machida, Y. Yamamoto, and K. Igeta, "Modification of spontaneous emission rate in planar dielectric microcavity structures," *Phys. Rev. A*, vol. 44, pp. 669–681, 1991.

[36] H. Benisty, H. D. Neve, and C. Weisbuch, "Impact of planar microcavity effects on light extraction–part II: selected exact simulations and role of photon recycling," *IEEE J. Quantum Electron.*, vol. 34, pp. 1632–1643, 1998.

Chapter 5 850-nm InAlGaAs/AlGaAs VCSEL

Vertical-cavity surface-emitting lasers with 850 nm emission had become standard in local area interconnects and free-space optical communications. The advantages, including relatively low threshold current, low divergent angle, and circular beam, which lead to simpler packaging, of these surface emission devices had been found to provide the low-cost short-distance data links [1]–[4]. To emit at 850 nm, the choice of the active region grown on GaAs substrate had been conscious of the materials including (In)GaAs/AlGaAs [5], [6], InAlGaAs/AlGaAs [7]–[9], and InGaAsP/InGaP [10], [11]. The incorporation of In into GaAs QWs had been demonstrated to provide compressive strain, which in turn resulted in lower threshold current and higher modulation speed [12], [13]. Previous research also showed that the InGaAsP, which was used during most of the initial development of long wavelength VCSELs, could provide comparable laser performance [5], [14]–[16].

It is well known that low transparency current achievable with strained QWs is required for providing low threshold current in a semiconductor laser. For laser devices with an emission wavelength of 850 nm, the incorporation of Al into InGaAs QWs with higher In composition can possess a desired strain level that beneficially reduces the threshold current densities of the devices [17], [18]. However, qualitative analysis of varying Al and In contents in approximately 850 nm InAlGaAs QWs is rarely reported in literature. In this study, we first theoretically study the gain-carrier characteristics of InGaAs and InAlGaAs QWs with variant In and Al compositions in order to investigate the In and Al compositional effect in InAlGaAs QWs. Then, an InAlGaAs QW is prepared by low-pressure MOCVD (VEECO D180), and the optical properties are studied by temperature dependent PL. The device characteristics of 850-nm InAlGaAs/AlGaAs VCSELs are then investigated. To improve the high temperature

performance, we propose to incorporate a high-bandgap 10-nm-thick $Al_{0.75}Ga_{0.25}As$ electronic blocking layer into the InAlGaAs/AlGaAs VCSELs for the first time. The threshold current and slope efficiency of the devices with a high-bandgap 10-nm-thick $Al_{0.75}Ga_{0.25}As$ electronic blocking layer are found to be less sensitive to the substrate temperature, and the output performance is enhanced in the mean time.

5-1 Theoretical analysis on InAlGaAs QWs

All the well widths of InGaAs and InAlGaAs QWs are designed to be 7 nm. Numerical parameters, required for *k·p* theory, used in this calculation are taken from Ref. [19]. The energy bandgaps of binary InAs, AlAs, GaAs alloys at room temperature are 0.354 eV, 3.004 eV, 1.423 eV, respectively, and the temperature dependent energy bandgaps are governed by *Varshini* equation. Specifically, the temperature dependent energy bandgaps of the binary alloys are calculated by following expressions:

$$E_g(InAs) = 0.417 - \frac{0.276\times10^{-3}\cdot T^2}{T+93}, \tag{5.1}$$

$$E_g(AlAs) = 3.099 - \frac{0.885\times10^{-3}\cdot T^2}{T+530}, \tag{5.2}$$

$$E_g(GaAs) = 1.519 - \frac{0.5405\times10^{-3}\cdot T^2}{T+204}, \tag{5.3}$$

For the energy bandgaps of ternary GaInAs, AlInAs and GaAlAs, and quaternary InAlGaAs alloys, the interpolation formulae are adapted from the composition dependent properties [20]:

$$E_g(InGaAlAs) = \frac{xyE_g^u(GaAlAs) + yzE_g^v(InAlAs) + xzE_g^w(InGaAs)}{xy+yz+zx}, \tag{5.4}$$

$$E_g^u(GaAlAs) = uE_g(AlAs) + (1-u)E_g(GaAs) - u(1-u)B(GaAlAs), \tag{5.5}$$

$$E_g^v(InAlAs) = vE_g(InAs) + (1-v)E_g(AlAs) - v(1-v)B(InAlAs), \tag{5.6}$$

$$E_g^w(InGaAs) = wE_g(InAs) + (1-w)E_g(GaAs) - w(1-w)B(InGaAs), \tag{5.7}$$

$$u = \frac{1-x+y}{2}, \quad v = \frac{1-y+z}{2}, \quad w = \frac{1-x+z}{2}, \tag{5.8}$$

where x, y, and $z = 1-x-y$ represented the compositions of Ga, Al, and In in the InAlGaAs material system respectively. The bandgap bowing parameters of AlGaAs, InAlAs, and InGaAs were $-0.127+1.310y$, 0.70, and 0.477 eV, respectively. The temperature dependent bandgap energies of the binary semiconductors were calculated using the Varshni formula. The conduction band offset for the compressively strained InAlGaAs/AlGaAs QW was assumed to be 67% of the total band offset [21].

During the simulations, the VCSEL devices were built up layer by layer except for the stepped $Al_{0.15}Ga_{0.85}As/Al_{0.9}Ga_{0.1}As$ DBRs which were assumed to be a bulk layer having an averaged Al content with the same thickness under simulation efficiency concern. It was convenient and might not influence the qualitative simulation results in this study because we specifically focused on the carrier blocking effect on the VCSEL devices by employing a high bandgap layer on the p-side of the QW active region.

For the InGaAs QWs and InAlGaAs QWs with variant In and Al compositions, the gain spectra and optical gain as a function of carrier density were calculated using the $k \cdot p$ theory with valence band mixing effects. For a fixed QW emission wavelength of 838 nm, the In composition in InGaAs QW is theoretically determined to be 2%, and a series design of InAlGaAs QWs with various In and Al compositions of (In, Al)=(8.5%, 4%), (15%, 8%), (21%, 12%), and (27%, 16%) are performed with unchanged $Al_{0.3}Ga_{0.7}As$ barriers. The induced compressive strains in $In_{0.02}Ga_{0.98}As$, $In_{0.085}Al_{0.04}Ga_{0.875}As$, $In_{0.15}Al_{0.08}Ga_{0.77}As$, $In_{0.21}Al_{0.12}Ga_{0.67}As$, and $In_{0.27}Al_{0.16}Ga_{0.57}As$ QWs are 0.143%, 0.611%, 1.053%, 1.498%, and 1.918%, respectively. The material gain available from a QW can be affected by a number of factors that need to be taken into account. It is well known that the QWs have to be designed with a low density of states and a closely matched density of states in the valence and conduction bands

[22]–[24]. However, a low density of states will cause the rapid rising of Fermi level with increased temperature; that is, more carriers may escape from the QW at elevated temperatures. Therefore, a large conduction band offset is required to secure the carrier confinement. Figure 5-1 shows the calculated material gains of the $In_{0.02}Ga_{0.98}As$ and InAlGaAs QWs with $Al_{0.3}Ga_{0.7}As$ barrier at 25 ºC when the input carrier concentration is 6×10^{18} cm^{-3}. The InAlGaAs QWs with variant Al compositions of 4%, 8%, 12%, and 16% are calculated and compared with the $In_{0.02}Ga_{0.98}As$ QW. In the calculation of the radiative currents, the thickness of the AlGaAs barriers is assumed to be three times that of the QWs. Moreover, the material of the barriers is $Al_{0.3}Ga_{0.7}As$ throughout the numerical analysis. It is found that the InAlGaAs QWs can provide higher material gain than the $In_{0.02}Ga_{0.98}As$ QW. It is also noteworthy that the material gain of the InAlGaAs QWs can be enhanced when the Al composition in InAlGaAs QW is increased. The material gain tends to saturate when the Al composition in InAlGaAs QW is higher than 8%.

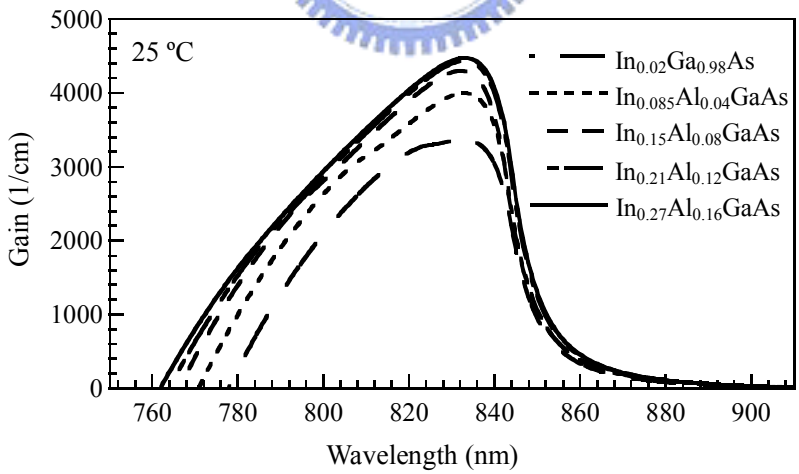

Figure 5.1 Calculated material gains of the $In_{0.02}Ga_{0.98}As$ and InAlGaAs QWs with $Al_{0.3}Ga_{0.7}As$ barrier at 25 ºC when the input carrier concentration is 6×10^{18} cm^{-3}. The material gain tends to saturate when the Al composition in InAlGaAs QW is higher than 8%.

Figure 5.2 shows the peak material gain as a function of (a) carrier concentration and (b) radiative current density of the $In_{0.02}Ga_{0.98}As$ and InAlGaAs QWs with

$Al_{0.3}Ga_{0.7}As$ barrier at 25 ºC. The radiative current density is obtained from the integral of spontaneous emission spectrum and the thickness of QW [25], [26]. Both the transparencies of carrier concentration and radiative current density of the InAlGaAs QWs are lower than those of the $In_{0.02}Ga_{0.98}As$ QW. The transparency carrier concentration depends primarily on the band curvatures, which is sensitive to the effective masses and the amount of strain. When the Al composition in InAlGaAs QW increases with increased In composition, the transparency carrier concentration decreases. Numerical results indicate that the density of states and the effective mass decrease with increased Al composition in InAlGaAs QW. The decrement in transparency carrier concentration is less apparent when the Al composition is higher than 8%.

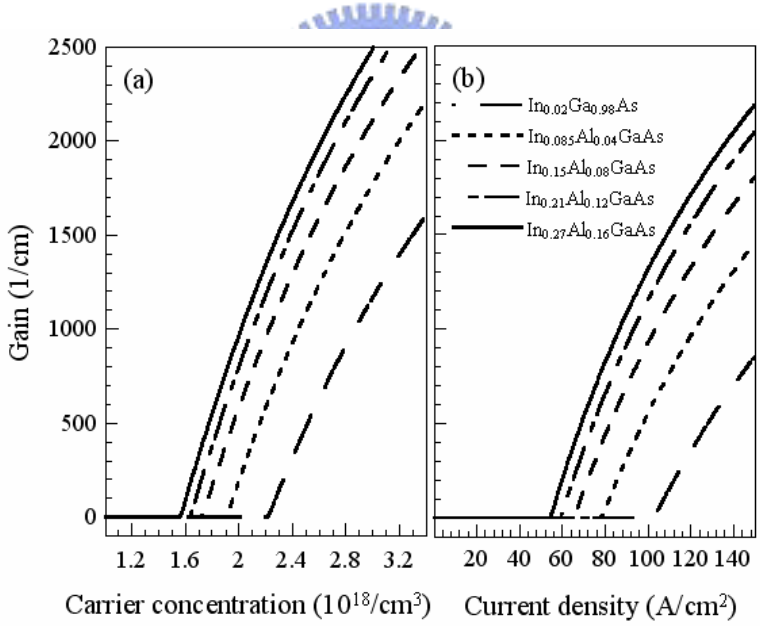

Figure 5.2 Peak material gain as a function of (a) carrier concentration and (b) radiative current density of the $In_{0.02}Ga_{0.98}As$ and InAlGaAs QWs with $Al_{0.3}Ga_{0.7}As$ barrier at room temperature.

Figure 5.3 shows the curves of valence band for the $In_{0.02}Ga_{0.98}As$ and InAlGaAs QWs with variant In and Al compositions at room temperature. The *y* axis of the figures represents the valence band QW potential. It is found that there are four confined hole levels in the InAlGaAs QWs, and the $In_{0.02}Ga_{0.98}As$ QW has another confined hole level

(LH_2) in addition to the four HH_1, HH_2, LH_1, and HH_3 confined levels. The number of confined hole levels may be influenced by the amount of strain in QWs and the effective masses of electrons and holes. With the increase of In and Al compositions in InAlGaAs QW, the amount of strain in QWs increases, and the effective mass of holes decreases. The reduction of the density of states in the valence band is desirous because low transparency carrier concentration can be achieved.

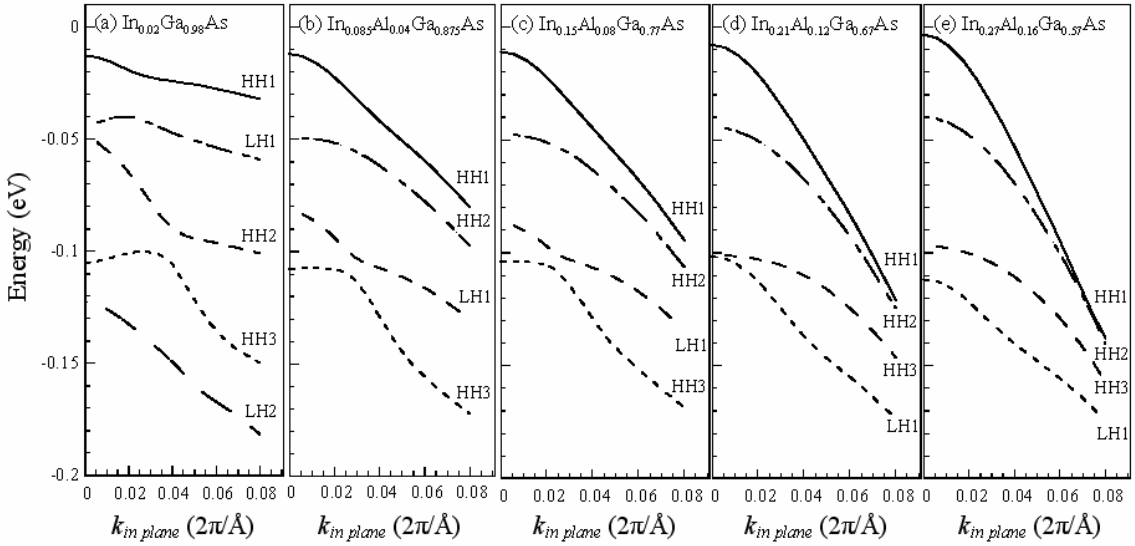

Figure 5.3 Curves of valence band for the $In_{0.02}Ga_{0.98}As$ and InAlGaAs QWs with variant In and Al compositions at 25 ºC. The *y* axis of the figures represents the valence band QW potential.

When the QW is at a temperature of 95 ºC, the spectra of material gain, and the peak material gain as a function of carrier concentration and radiative current density of the $In_{0.02}Ga_{0.98}As$ and InAlGaAs QWs with $Al_{0.3}Ga_{0.7}As$ barrier are shown in Figures 5.4, and 5.5, respectively. The InAlGaAs QW with more In and Al compositions is also found to provide higher material gain, and the gain tends to saturate when the Al composition is higher than 12%. The red shift of the peak emission wavelength is 0.25 nm/K, which is approximately the same for all $In_{0.02}Ga_{0.98}As$ and InAlGaAs QWs. The decrement of the peak material gain with increased temperature from 25 to 95 ºC in $In_{0.02}Ga_{0.98}As$ and InAlGaAs QWs is also approximately the same when the input carrier concentration remains unchanged at 6×10^{18} cm^{-3}. As indicated in Fig. 5, lower

transparency carrier concentration and radiative current density are observed when the In and Al compositions in InAlGaAs QW increase. Due to the relatively incremental compressive strain, higher differential gain is also obtained over the temperature range under study. In this study, it is prognosticated that the transparency carrier concentration of the $In_{0.02}Ga_{0.98}As$ QW is increased by approximately 26.8% as temperature increases from 25 to 95 ºC. For InAlGaAs QWs, the transparency carrier concentrations are increased by 26.3% (Al=4%), 25.2% (Al=8%), 23.8% (Al=12%), and 21.7% (Al=16%) as temperature increases from 25 to 95 ºC, which are smaller than those of the $In_{0.02}Ga_{0.98}As$ QWs because more compressive strain in QW can reduce the transparency carrier concentration and the relatively large conduction band offset, which is increased with the increase of In and Al compositions in InAlGaAs QW, can prevent carriers from escaping from the QW. In addition, the increase of transparency carrier concentration with increased temperature is attributed to the increment of nonradiative recombination and the poor electron confinement; namely, large amount of electrons can pile up from the QW and overflow without attributing to the radiative recombination, when the temperature is high.

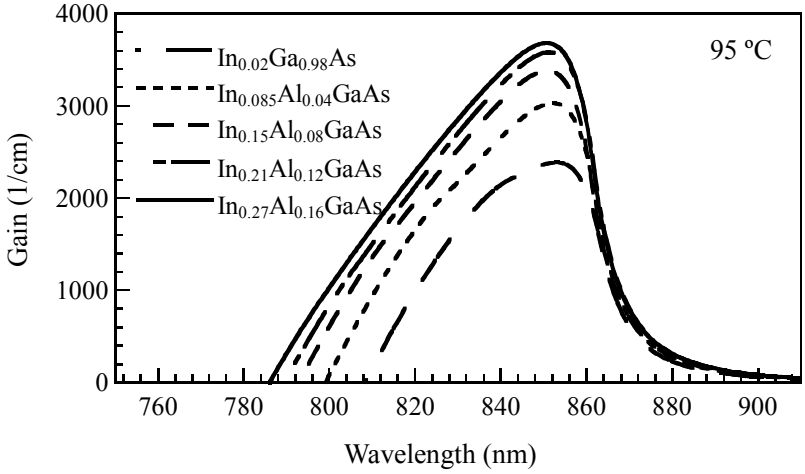

Figure 5.4 Calculated spectra of material gains of the $In_{0.02}Ga_{0.98}As$ and InAlGaAs QWs with $Al_{0.3}Ga_{0.7}As$ barrier at 95 ºC when the input carrier concentration is 6×10^{18} cm^{-3}.

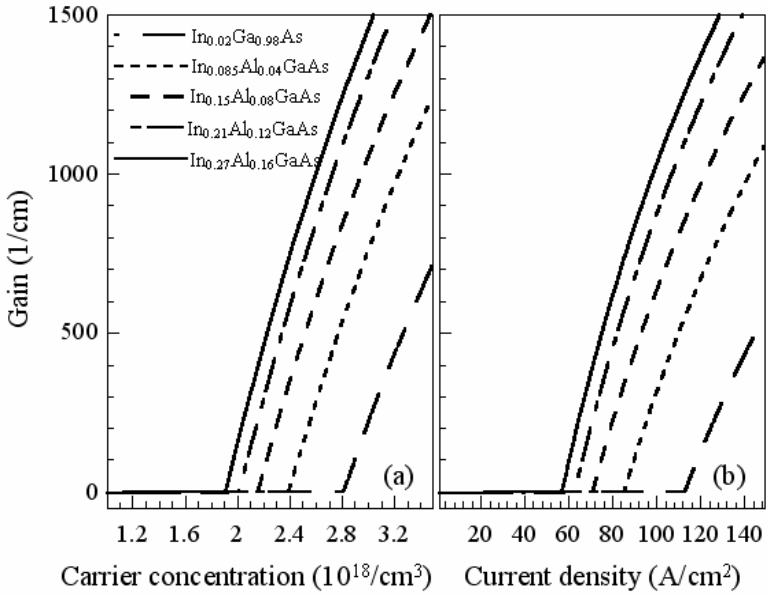

Figure 5.5 Peak material gain as a function of (a) carrier concentration and (b) radiative current density of the $In_{0.02}Ga_{0.98}As$ and InAlGaAs QWs with $Al_{0.3}Ga_{0.7}As$ barrier at 95 ºC.

5-2 Optical properties of fabricated QWs and device fabrication

After investigating the numerical gain-carrier characteristics of the $In_{0.02}Ga_{0.98}As$ and InAlGaAs QWs, the next step is to fabricate the 850-nm VCSELs. The numerical results suggest that the InAlGaAs QWs with Al composition higher than 8% can provide better gain-carrier characteristics. However, although crystal quality concerns cannot be taken into account in numerical calculations, it is noteworthy that increase of In and Al concentrations will result in a larger amount of strain in InAlGaAs QW and a higher strain level in QW may have crystal quality concerns. Thus, the In and Al concentrations in InAlGaAs QWs cannot be too high. In fact, degradation in higher Al content QW PL has been experimentally observed. Therefore, the $In_{0.15}Al_{0.08}Ga_{0.77}As/Al_{0.3}Ga_{0.7}As$ with a compressive strain of 1.053% is chosen and grown to form the QW active region of the 850-nm VCSEL. The temperature dependent PL of the $In_{0.15}Al_{0.08}Ga_{0.77}As$ triple-QW structure is shown in Figure 5.6. The QW was grown by low pressure MOCVD on GaAs (100) substrate with group-V precursors of arsine (AsH_3). Trimethyl (TM–) sources of aluminum (Al), gallium (Ga), and indium

(In) were used for group-III precursors. The thickness of QW is 7 nm, which is identical to that used in numerical calculation. The thickness and Al composition of barriers are 8 nm and 0.3, respectively. The growth rate is about 0.75 nm/s and the growth temperature is 720 ºC. The composition in QW is characterized by the rocking curve of high-resolution x-ray diffraction. Temperature dependent PL measurement is performed by a 325-nm He-Cd laser with 20 mW output over a temperature range of 17–300 K. The laser power is 20 mW and the spot size is about 100 μm in diameter. Luminescence is analyzed by a 320-mm grating monochromator and detected by a charge couple detector.

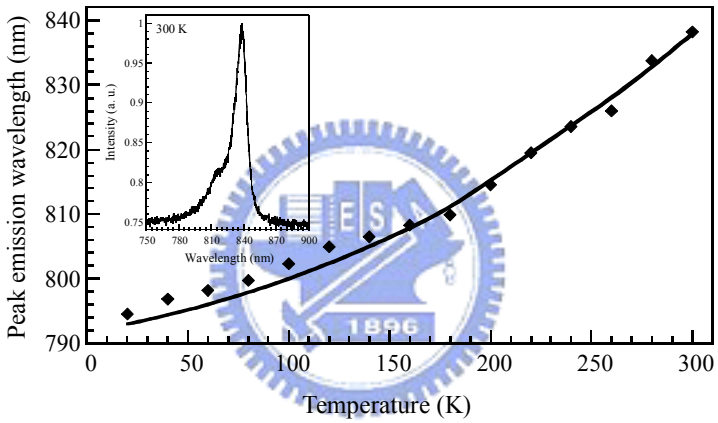

Figure 5.6 Temperature dependent PL peak emission wavelength of the $In_{0.15}Al_{0.08}Ga_{0.77}As$ triple-QW structure. The inset is the optical spectrum obtained at 300 K.

In Figure 5.6, the dots represent the peak emission wavelength obtained from PL measurement, and the curve represents the numerical spontaneous emission rate of the $In_{0.15}Al_{0.08}Ga_{0.77}As/Al_{0.3}Ga_{0.7}As$ QW that is obtained when the input carrier concentration is 5×10^{15} cm^{-3}, which is calculated based on the excited power density and laser spot size. The peak emission wavelength at 300 K is 838 nm, and the FWHM is 13.5 nm, which is comparable to the (In)GaAs/AlGaAs material systems. When the temperature decreases to 20 K, the peak emission wavelength shifts to 793 nm with a FWHM of 6.6 nm. Figure 5.7 shows the normalized integrated PL intensity plotted as a

function of reciprocal temperature for the $In_{0.15}Al_{0.08}Ga_{0.77}As$ triple-QW structure. Fitting our data to the classical *Arrhenius* law, $I=I_0/\{1+c\exp(-E_a/KT)\}$, according to the thermal carrier transfer mechanism, the activation energy (E_a) of the $In_{0.15}Al_{0.08}Ga_{0.77}As$ QW is determined to be 39.8 meV.

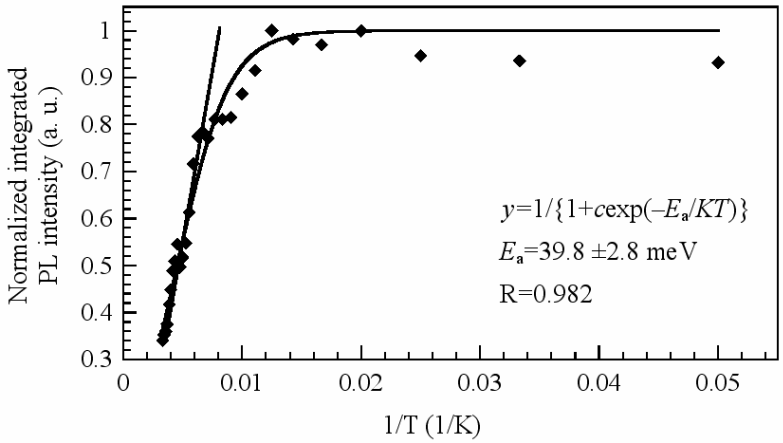

Figure 5.7 Normalized integrated PL intensity plotted as a function of reciprocal temperature for the $In_{0.15}Al_{0.08}Ga_{0.77}As$ triple-QW structure.

As investigated in the numerical discussion, it is observed that the InAlGaAs QWs can provide a lower transparency carrier concentration and a higher differential gain. The transparency carrier concentration of the InAlGaAs QWs increased with elevated temperature up to 95 ºC is also less sensitive than the $In_{0.02}Ga_{0.98}As$ QW. However, more than 20% increment of the transparency carrier concentration is too high to be ignored for the InAlGaAs QWs. Therefore, methods for reduction of temperature sensitivity need to be sought. To reduce the electronic leakage current and the temperature sensitivity of semiconductor lasers, a high bandgap layer is regularly embedded into the active region before the growth of p-type layers [27]–[29]. In this paper, we propose to employ an AlGaAs electronic blocking layer to improve the high temperature performance for the 850-nm VCSELs under study.

A schematic plot of the VCSEL devices with and without a high bandgap electron blocking layer is shown in Figure 5.8. The devices were assumed to be on the GaAs

substrate with a 0.5-μm-thick GaAs buffer layer having an n-doping level of 1×10^{18} cm^{-3}. The bottom and top DBRs were consisted of 39 pairs and 21 pairs $Al_{0.15}Ga_{0.85}As/Al_{0.9}Ga_{0.1}As$, which had 99.93% and 99.73% reflectivity, respectively. The active region, which was surrounded by one-wavelength-cavity $Al_{0.6}Ga_{0.4}As$ claddings, was formed by three 7-nm-thick $In_{0.15}Al_{0.08}Ga_{0.77}As$ QWs and four 8-nm-thick $Al_{0.3}Ga_{0.7}As$ barriers. A 30-nm-thick $Al_{0.97}Ga_{0.03}As$ was introduced on the upper cavity spacer layer to form an oxide confinement. A one-wavelength-thick $Al_{0.15}Ga_{0.85}As$ current-spreading layer ($p=5\times10^{18}$ cm^{-3}) and a heavily doped GaAs ($p=2\times10^{19}$ cm^{-3}) contact layer were ultimately put to complete the structure. Three VCSEL devices A, B, and C were presented and compared in this study, in which device A was in a conventional design, without containing a high bandgap electron blocking layer on the p-side of QW active region. Both devices B and C were designed to have an electron blocking layer, in which the material was chosen as AlGaAs with higher Al content because of its natural lattice match to GaAs. The electron blocking layers in devices B and C were 10-nm-thick $Al_{0.75}Ga_{0.25}As$ and 13-nm-thick $Al_{0.9}Ga_{0.1}As$. For all three devices, the detuning between the QW spontaneous emission and the cavity was 12 nm, where the dip of Fabry-Pérot was 850 nm. The oxide aperture for the three devices was 7 μm in diameter.

The fabrication process began from depositing a 1.3-μm-thick SiN_x layer, which acted as a hard mask in the following process, onto the wafer by plasma enhanced chemical vapor deposition (PECVD) at 300 ºC. Standard photolithography and reactive ion etching (RIE) using SF_6 with a flow rate of 20 sccm as etching gas were then performed to define etching pattern on the hard mask. Trench mesa etching by Cl_2 with a flow rate of 2 sccm and Ar plasma were performed to transfer the mask pattern onto the wafer. The etching depth was cautiously controlled to penetrate the active region, and the 30-nm-thick $Al_{0.97}Ga_{0.03}As$ aperture layer was exposed for selective oxidation in

400 ºC stream environment. The mesa diameter was 22 μm and the oxide aperture was 7 μm. After oxidation, the residual dielectric was removed, and a second 150-nm-thick SiO_2 by PECVD was deposited for passivation, followed by a partially etched process for contact window. Ti (30 nm)/Pt (50 nm)/Au (200 nm) were deposited onto the heavily p-doped GaAs contact layer for p-contact, and AuGe (50 nm)/Ni (20 nm)/Au (350 nm) were deposited for n-contact.

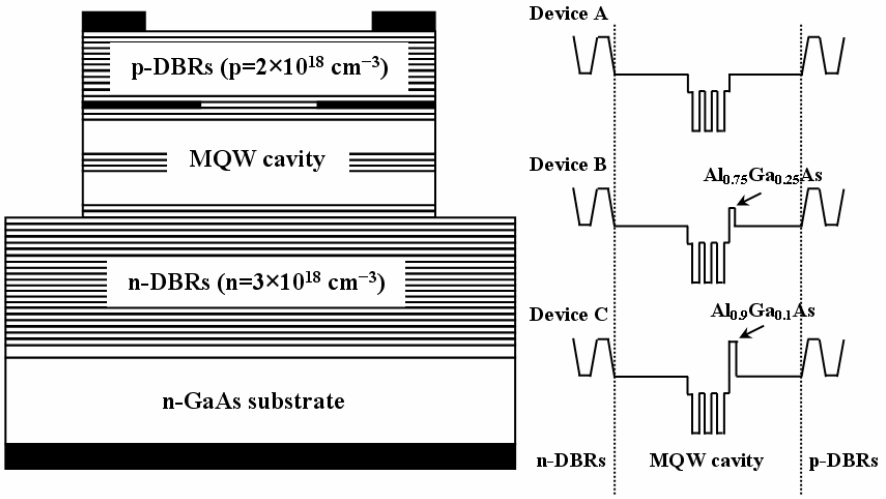

Figure 5.8 A schematic plot of the VCSEL devices with and with a high bandgap electron blocking layer.

5-3 Fabricated device characteristics

For each design of the fabricated VCSELs, nine devices were randomly selected to measure the output characteristics, and the discrepancy of the nine devices for each design was negligibly small. Figure 5.9 shows the RT L-I-V characteristic of the fabricated VCSELs for devices A, B, and C. The oxide aperture for all the three devices was 7 μm in diameter, and was determined from a series of calibration samples having similar structure design. In device A, a threshold current of 1.47 mA with a slope efficiency of 0.37 mW/mA, and a threshold voltage of 1.85 V were obtained. The L-I curve started to roll over at about 2.8 mW as a result of internal heating effect. In device B, the laser output performance was found to be improved by inserting a 10-nm-thick

high bandgap $Al_{0.75}Ga_{0.25}As$ electron blocking layer, as indicated in the simulations. The threshold current of device B was reduced to 1.33 mA with a slope efficiency of 0.53 mW/mA, while a maximum power of 4.7 mW was achieved. However, it was found in device C that the threshold current increased to 1.87 mA and the slope efficiency became 0.26 mW/mA when a 13-nm-thick $Al_{0.9}Ga_{0.1}As$ layer was substituted as the high bandgap electron blocking layer. The decreased output performance might be attributed to the higher resistance during the device process and the small distance between the $Al_{0.9}Ga_{0.1}As$ electron blocking layer and QWs that degraded the crystal quality during oxidation process. The increase of threshold current in device C might also be partially due to the difficulty of hole injection into QWs from numerical simulation analysis. The discrepancy of the slope efficiencies between theory and experiment may be attributed to the fact that the thermal behavior of a VCSEL is difficult to characterize in theoretical calculation.

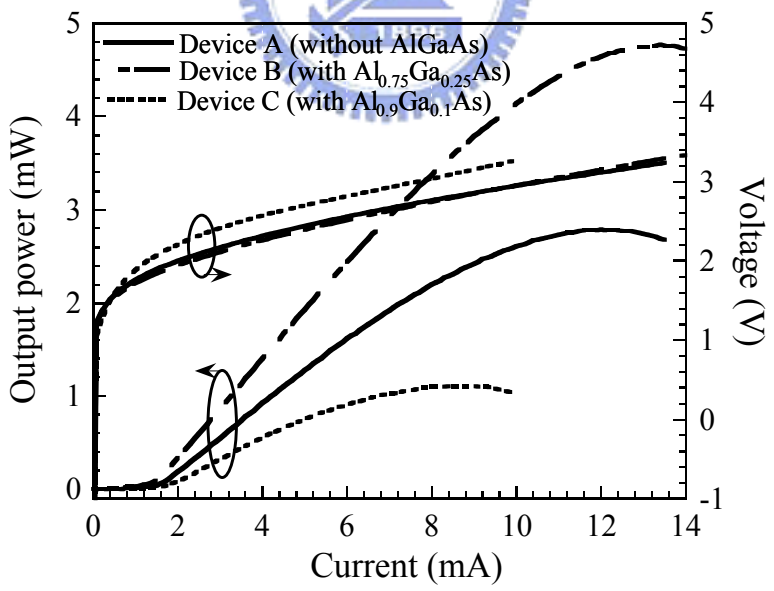

Figure 5.9 RT L-I-V characteristic of the fabricated VCSELs for devices A, B, and C with an oxide aperture of 7 μm.

Figure 5.10 shows the experimental temperature dependent variation of threshold current and slope efficiency of devices A, B, and C. As compared with the standard

design of device A, device B showed a less temperature sensitive output performance, where the amount of increase in threshold current at an elevated temperature of 95 °C was only 0.27 mA and the slope efficiency dropped by only 24.5%. The threshold current of device A increased to 2.17 mA with a slope efficiency reduction of 32% when the substrate temperature was 95 °C. For device C, the increase of threshold current was from 1.85 to 2.01 mA with a slope efficiency reduction of 43% when the substrate temperature increased from 25 to 95 °C.

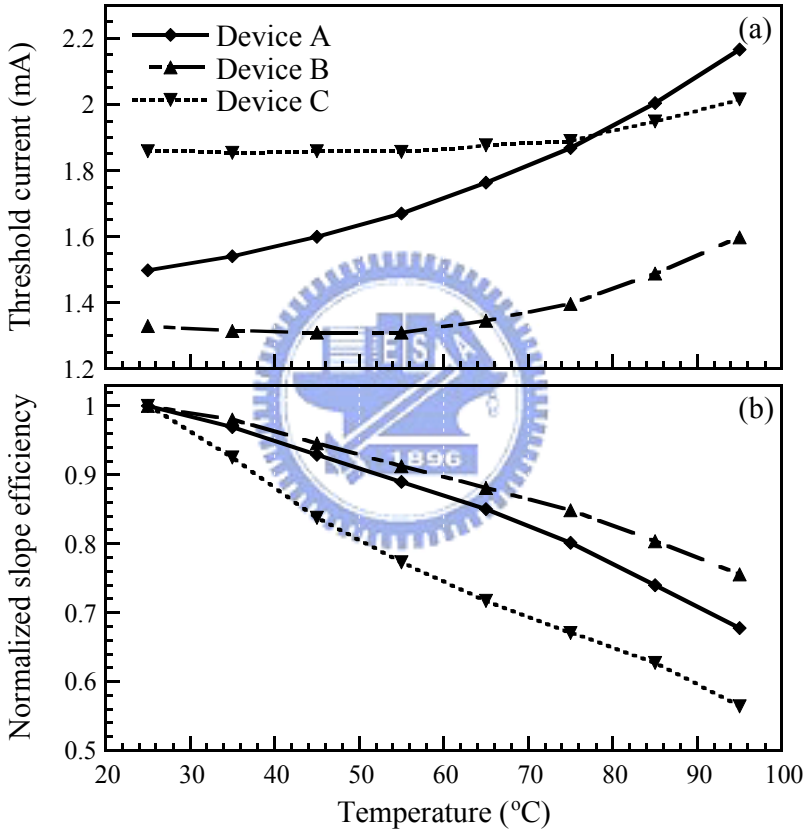

Figure 5.10 Experimental temperature dependent variation of threshold current and slope efficiency of devices A, B, and C.

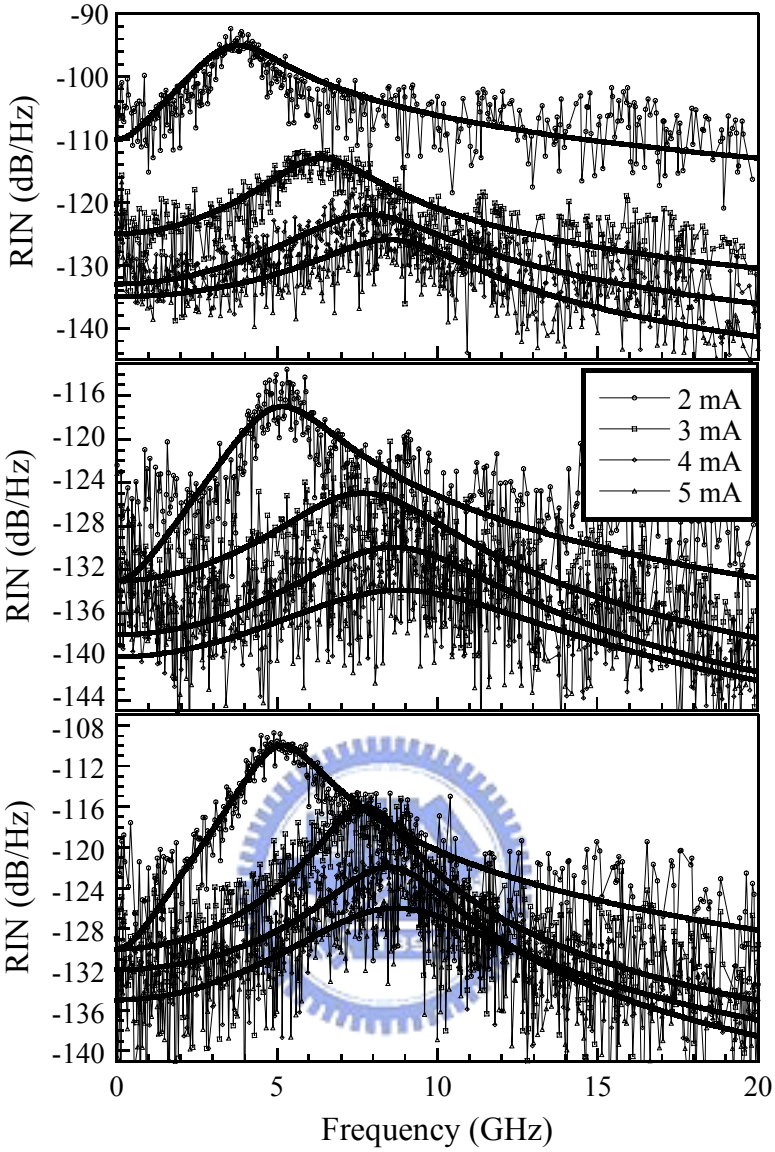

Figure 5.11 RT relative intensity noise (RIN) value of the three devices in a bias current range of 2–5 mA.

The measured RIN value of the devices was shown in Figure 5.11, where the solid lines are the fitting curves in accordance with the RIN transfer function:

$$RIN = \frac{4}{\pi}\delta f_{st}\frac{f^2 + (\gamma/2\pi)^2}{(f_r{}^2 - f^2)^2 + f^2(\gamma/2\pi)^2}, \tag{5.9}$$

where f_r represents the resonant frequency, and r is the damping rate. The RIN illustrated the maximum available amplitude range for signal modulation and served as a quality indicator of a laser. The value of RIN could be thought as a type of inverse

carrier-to-noise-ratio measurement, and could be defined as the ratio of the mean-square optical intensity noise to the square of the average optical power. The RIN values of the three devices were obtained in a bias current range of 2–5 mA. As the bias current increased, the peak RIN frequency responses of the three devices increased respectively, and a frequency response of 8.5 GHz for device A, 8.9 GHz for device B, and 8.7 GHz for device C was obtained when the bias current was 5 mA. The results also suggest that the insertion of an electron blocking layer to reduce the electronic leakage current and improve the light output performance does not deteriorate the frequency response.

5-4 Theoretical analysis on devices' characteristics

The room temperature light output and voltage versus current (L-I-V) characteristics of the devices A, B, and C studied in simulation are shown in Figure 5.12. It was found theoretically that the threshold current was slightly reduced and the laser output power at high current injection region was enhanced by inserting a 10-nm-thick $Al_{0.75}Ga_{0.25}As$ electron blocking layer in device B. However, when the electron blocking layer was substituted to be a thicker (13 nm) and higher Al content $Al_{0.9}Ga_{0.1}As$ layer, the threshold current in device C was increased in the opposite way. Nevertheless, the slope efficiency and the maximum output power at roll over point in device C were improved. The decreased threshold current in device B should be attributed to the increase of optical confinement factor value, and hence enhancing the radiative and stimulated recombination in the QWs. The values of optical confinement factor for devices A, B, and C were 2.812%, 2.853%, and 2.869%, respectively. For device C, even the value of optical confinement factor was the highest among the three devices, the holes in the valence band would meet a higher and thicker barrier when injecting into QWs because of the higher Al content and thicker electron blocking layer.

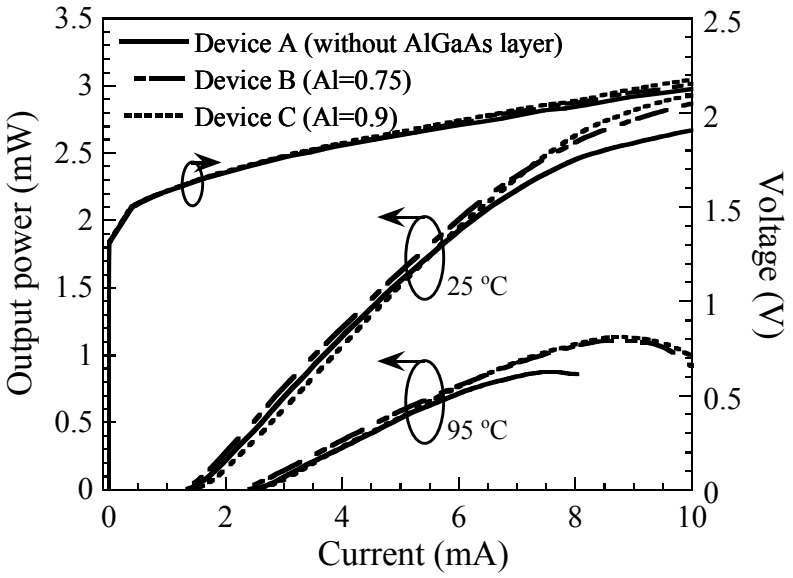

Figure 5.12 Simulation results of the RT light output and voltage versus current characteristics of devices A, B, and C. The electron blocking layers for devices B and C are 10-nm-thick $Al_{0.75}Ga_{0.25}As$ and 13-nm-thick $Al_{0.9}Ga_{0.1}As$, respectively.

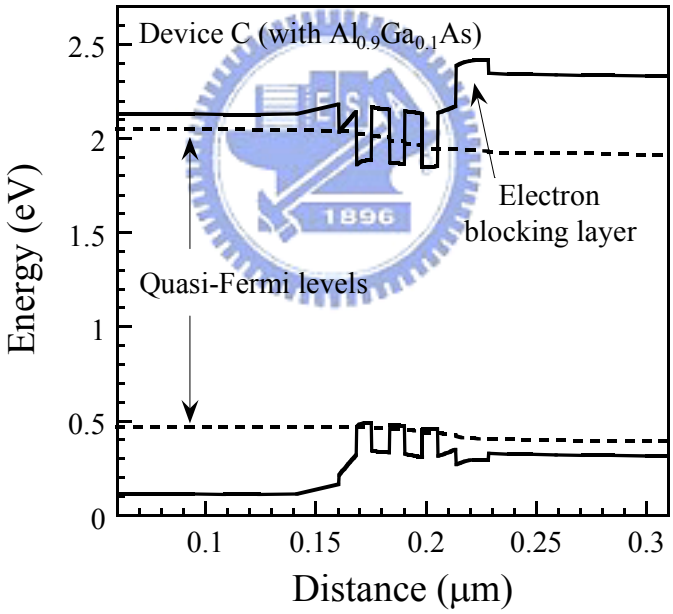

Figure 5.13 Expanded energy band diagram near the QW active region of device C. The diagram was obtained at RT with an applied voltage of 2.1 V.

To further explain the difficulty of holes injection into QWs when using a 13-nm-thick $Al_{0.9}Ga_{0.1}As$ as electron blocking layer in device C, the expanded energy band diagram near the QW active region is shown in Figure 5.13. The diagram was obtained at RT with an applied voltage of 2.1 V (10 mA). The left-hand side of the diagram was the n-side of the VCSEL device, and the dashed lines represented the

quasi-Fermi levels. It was shown that the high bandgap $Al_{0.9}Ga_{0.1}As$ layer was on the p-side of the QW active region. And, because the electrons have higher mobility than the holes, the $Al_{0.9}Ga_{0.1}As$ layer can act as an electron blocking layer to prevent electron leakage and hence improve the laser performance at high current injection. However, the increased barrier height in the valence band would result in the difficulty of hole injection into QWs when the device was at lower current injection and therefore increasing the threshold current.

Next, the electron leakage current as functions of input current and device temperature was discussed. In this study, the percentage of electron leakage current was defined as the ratio of the current overflowed to the p-type layer to that injected into the devices. As an example of device A, the percentage of electron leakage current as a function of input current when the device temperature was in a range of 25–95 ºC is indicated in Figure 5.14. More percentage of electron leakage current was found when the input current was increased, and the percentage of electron leakage current increased rapidly when the device temperature increased. It is reasonable because the electrons will have higher kinetic energy and the probability of electrons overflowing away from the QWs is increased when the device temperature increases. The percentage of electron leakage current as a function of device temperature for devices A, B, and C is shown in Figure 5.15. The total input current for all three devices was 10 mA and the device temperature under discussion was in a range of 25–95 ºC. We found that the percentage of electron leakage current could be apparently reduced using a high bandgap AlGaAs layer. Therefore, as depicted from the simulation results, the laser output performance of 850-nm VCSEL can be improved by inserting a high bandgap electron blocking layer to reduce electron leakage current. Especially, a 10-nm-thick $Al_{0.75}Ga_{0.25}As$ may be appropriate because of the reduced threshold current and better laser output performance under high temperature operation.

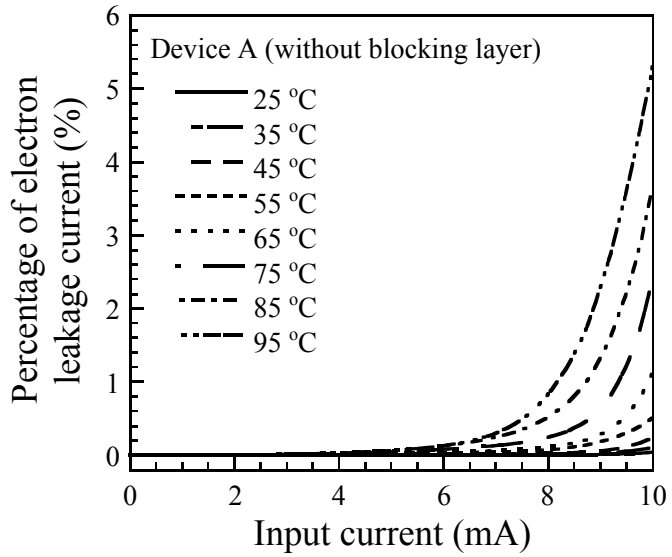

Figure 5.14 Percentage of electron leakage current as a function of input current in device A when the device temperature was in a range of 25–95 ºC.

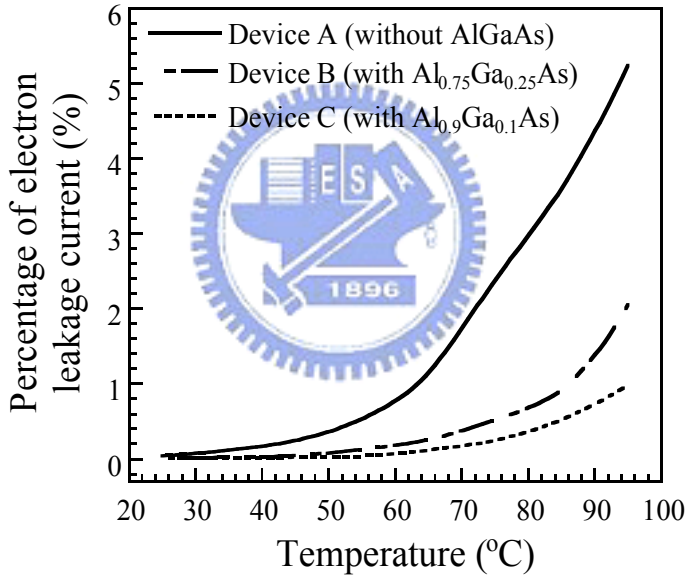

Figure 5.15 Percentage of electron leakage current as a function of device temperature for devices A, B, and C. The curves were obtained when the devices were biased at 10 mA.

5-5 Summary

In summary, the gain-carrier characteristics of the $In_{0.02}Ga_{0.98}As$ and InAlGaAs QWs with 838 nm emission are theoretically investigated. The numerical results suggest that the incorporation of Al into InGaAs QW is found to provide higher material gain, lower transparency carrier concentration and radiative current density due to the

increment of the amount of strain and the reduced density of states. The optical properties of $In_{0.15}Al_{0.08}Ga_{0.77}As$ QW are also investigated by temperature dependent PL. The carrier blocking effect on the output performance of 850-nm InAlGaAs/AlGaAs VCSELs are also experimentally and theoretically investigated. With the use of a high-bandgap 10-nm-thick $Al_{0.75}Ga_{0.25}As$ layer in the $In_{0.15}Al_{0.08}Ga_{0.77}As/Al_{0.3}Ga_{0.7}As$ QW active region, the high temperature characteristics and the output performance are found experimentally improved. The results obtained theoretically also approved that the improvement in output performance is due to the reduction of the electron leakage current. Small-signal frequency response shows that these VCSELs can provide a modulation bandwidth of approximately 9.2 GHz.

References

[1] J. Gilor, I. Samid, and D. Fekete, "Threshold current density reduction of strained AlInGaAs quantum-well laser," *IEEE J. Quantum Electron.*, vol. 40, pp. 1355–1364, 2004.

[2] J. A. Lehman, R. A. Morgan, M. K. Hibbs-Brenner, and D. Carlson, "High-frequency modulation characteristics of hybrid dielectric/AlGaAs mirror singlemode VCSELs," *Electron. Lett.*, vol. 31, pp. 1251–1252, 1995.

[3] K. L. Lear, A. Mar, K. D. Choquette, S. P. Kilcoyne, R. P. Schneider, Jr., and K. M. Geib, "High-frequency modulation of oxide confined vertical cavity surface emitting lasers," *Electron. Lett.*, vol. 32, pp. 457–458, 1996.

[4] F. H. Peters and M. H. MacDougal, "High-speed high-temperature operation of vertical-cavity surface-emitting lasers" *IEEE Photon. Technol. Lett.*, vol. 13, pp. 645–647, 2001.

[5] T. E. Sale, C. Amano, Y. Ohiso, and T. Kurokawa, "Using strained $(Al_xGa_{1-x})_yIn_{1-y}As_zP_{1-z}$ system materials to improve the performance of 850 nm surface- and edge-emitting lasers," *Appl. Phys. lett.*, vol. 71, pp. 1002–1004, 1997.

[6] H. C. Kuo, Y. H. Chang, F. Y. Lai, T. H. Hseuh, L. T. Chu, and S. C. Wang, "High speed performance of 850 nm silicon-implanted AlGaAs/GaAs vertical cavity emitting laser," *Solid State Electron.*, vol. 48, pp. 483–485, 2004.

[7] J. Ko, E. R. Hegblom, Y. Akulova, B. J. Thibeault, and L. A. Coldren, "Low-threshold 840-nm laterally oxidized vertical-cavity lasers using AlInGaAs–AlGaAs strained active layers," *IEEE Photon. Technol. Lett.*, vol. 9, pp. 863–865, 1997.

[8] O. Tadanaga, K. Tateno, H. Uenohara, T. Kagawa, and C. Amano, "An 850-nm InAlGaAs strained quantum-well vertical-cavity surface-emitting laser grown on GaAs (311)B substrate with high-polarization stability," *IEEE Photon. Technol. Lett.*, vol. 12, pp. 942–944, 2000.

[9] S. L. Yellen, R. G. Waters, A. H. Shepard, J. A. Baumann, and R. J. Dalby, "Relaibility of InAlGaAs strained-quantum-well lasers operating at 0.81μm," *IEEE Photon. Technol. Lett.*, vol. 4, pp. 829–831, 1992.

[10] N. Tansu, D. Zhou, and L. J. Mawst, "Low-temperature-sensitivity, compressively strained InGaAsPactive (λ=0.78–0.85 μm) region diode lasers," *IEEE Photon. Technol. Lett.*, vol. 12, pp. 603–605, 2000.

[11] L. J. Mawst, S. Rulsi, A. Al-Muhanna, and j. K. Wade, "Short-wavelength (0.7 μm $< \lambda <$ 0.78 μm) high-power InGaAsP-active diode lasers," *IEEE J. Select. Topics Quantum Electron.*, vol. 5, pp. 785–791, 1999.

[12] H. K. Choi and C. A. Wang, "InGaAs/AlGaAs strained single quantum well diode

lasers with extremely low threshold current density and high efficiency," *Appl. Phys. Lett.*, vol. 57, pp. 321–323, 1990.

[13] T. R. Chen, B. Zhao, L. Eng, Y. H. Zhoung, J. O'Brien, and A. Yariv, "Very high modulation efficiency of ultralow threshold current single quantum well InGaAs lasers," *Electron. Lett.*, vol. 29, pp. 1525–1526, 1993.

[14] N. Tansu and L. J. Mawst, "Compressively-strained InGaAsP-active (λ=0.85 μm) VCSELs," *IEEE Lasers and Electro-Optics Society 2000 Annual Meeting. LEOS 2000.* vol. 2, pp. 724–725, 2000.

[15] H. C. Kuo, Y. S. Chang, F. I. Lai, and T. H. Hsueh, "High speed modulation of 850-nm InGaAsP/InGaP strain-compensated VCSELs," *Electron. Lett.*, vol. 39, pp. 1051–1052, 2003.

[16] Y. S. Chang, H. C. Kuo, F. I. Lai, Y. A. Chang, C. Y. Lu, L. W. Laih, and S. C. Wang, "Fabrication and characteristics of high-speed oxide-confined VCSELs using InGaAsP–InGaP strain-compensated MQWs," *IEEE J. Lightwave Technol.*, vol. 22, pp. 2828–2833, 2004.

[17] H. K. Choi, C. A. Wang, D. F. Kolesar, R. L. Aggrawal, and J. N. Walpole, "High-power, high-temperature operation of AlInGaAs–AlGaAs strained single-quantum-well diode lasers," *IEEE Photon. Technol. Lett.*, vol. 3, pp. 857–859, 1991.

[18] N. A. Hughes, J. C. Connolly, D. B. gilbert, and K. B. Murphy, "AlInGaAs/AlGaAs strained quantum-well ridge waveguide lasers grown by metalorganic chemical vapor deposition," *IEEE Photon. Technol. Lett.*, vol. 4, pp. 113–115, 1992.

[19] I. Vurgaftman, J. R. Meyer, and L. R. Ram-Mohan, "Band parameters for III-V compound semiconductors and their alloys," *J. Appl. Phys.*, vol. 89, pp. 5815–5875, 2001.

[20] S. Adachi, "Band gaps and refractive indices of AlGaAsSb, GaInAsSb, and InPAsSb: key properties for a variety of the 2–4 μm optoelectronic device applications," *J. Appl. Phys.*, vol. 61, pp. 4869–4876, 1987.

[21] J. R. Jensen, J. M. Hvam, and W. Langbein, "Optical properties of InAlGaAs quantum wells: Influence of segregation and band bowing," *J. Appl. Phys.*, vol. 86, pp. 2584–2589, 1999.

[22] J. C. L. Yong, J. M. Rorison, and I. H. White, "1.3-μm quantum-well InGaAsP, AlGaInAs, and InGaAsN laser material gain: a theoretical study," *IEEE J. Quantum Electron.*, vol. 38, pp. 1553–1564, 2002.

[23] K. M. Lau, "Ultralow threshold quantum well lasers," in *Quantum Well Laser*, P. Zory, Ed. San Diego, CA: Academic, 1993.

[24] D. Ahn, S. L. Chuang, and Y. C. Chang, "Valence-band mixing effects on the gain

and the refractive index change of quantum-well lasers," *J. Appl. Phys.*, vol. 64, pp. 4056–4064, 1988.

[25] S. Seki, H. Oohashi, H. Sugiura, T. Hirono, and K. Yokoyama, "Study on the dominant mechanisms for the temperature sensitivity of threshold current in 1.3 μm InP-based strained-layer quantum-well lasers," *IEEE J. Quantum Electron.*, vol. 32, pp. 1478–1486, 1996.

[26] J. W. Pan and J. I. Chyi, "Theoretical study of the temperature dependence of 1.3 μm AlGaInAs-InP multiple-quantum-well lasers," *IEEE J. Quantum Electron.*, vol. 32, pp. 2133–2138, 1996.

[27] G.B. Stringfellow and M.G. Craford, in *High Brightness Light Emitting Diodes*, Academic Press, San Diego, 1997.

[28] S. Nakamura, M. Senoh, S. Nagahama, N. Iwasa, T. Matsushita, and T. Mukai, "Blue InGaN-based laser diodes with an emission wavelength of 450 nm," *Appl. Phys. Lett.*, vol. 76, pp. 22–24, 2000.

[29] Y. K. Kuo and Y. A. Chang, "Effect of electronic current overflow and inhomogeneous carrier distribution on InGaN quantum well laser performance," *IEEE J. Quantum Electron.*, vol. 40, pp. 437–444, 2004.

Chapter 6 1.3-μm InGaAsN/GaAsN EEL

Recent progress of the semiconductor lasers with emission wavelength of 1.3 μm for optical communication system has focused on using InGaAsN/GaAsN materials as quantum well active region. Laser performances of InGaAsN/GaAsN EELs have been found comparable to or superior to some of the best published results based on the conventional InP technology [1]–[11]. High-temperature operation has been anticipated in these material systems due to better electron and hole confinement by increased band offsets and a more favorable band-offset ratio. Previous research showed that for pulse operation of InGaAsN lasers, the characteristic temperature coefficient T_0 value of exceeding 200 K was demonstrated [12]–[14]; while for continue-wave operation, the T_0 of 70–110 K was also achieved [15]–[19]. Unfortunately, based on the predicted theoretical calculation of the maximal T_0 value in InGaAsN laser structures, these high performance InGaAsN lasers showed only a slight improvement in T_0 values over those achievable by the conventional InP technology. Fehse *et al*. found that the unexpected low T_0 value of InGaAsN lasers was attributed to the existence of large Auger recombination [20]. The difficulty of nitrogen atoms incorporating into InGaAs alloys, which lead to poor crystal quality, and the hole leakage problem [21] might be the key issues that resulted in the unexpected low T_0 value of InGaAsN lasers.

To achieve a more favorable T_0 value and a better output performance of InGaAsN lasers, there had been several works investigating the InGaAsN lasers with strain-compensated GaAsN as direct barriers. Even GaAsN is a smaller band gap material system, using GaAsN barrier instead of GaAs barrier could reduce nitrogen outdiffusion from the well and balancing the highly compressive strain in InGaAsN QW [22]. The same phenomenon had also numerically obtained by Fan *et al* [12]. However, adding more nitrogen atoms into barrier may decrease barrier potential and the carrier

leakage problem follows at high device temperature, even though longer wavelength emission can be obtained. This problem was solved by Tansu *et al.*, who utilized tensile-strain $GaAs_{0.85}P_{0.15}$ layers on both sides of the InGaAsN/GaAs active region to reduce the strain in QWs for achieving better crystal quality that in turn improved the laser performances [15], [16], [21]. Nevertheless, it could be though in the physical band alignment that the high bandgap $GaAs_{0.85}P_{0.15}$ layer on the n-side InGaAsN/GaAs active region may obstruct electrons pouring into the active region, while the $GaAs_{0.85}P_{0.15}$ layer on the p-side active region can blocking electrons overflowing to the p-side layers.

To obtain a more favorable characteristic temperature coefficient T_0 in 1.3-μm InGaAsN/GaAsN lasers, in this chapter, we first investigate the material gain properties of InGaAsN/$GaAs_{1-x}N_x$ QW lasers with various $GaAs_{1-x}N_x$ strain compensated barriers (x=0%, 0.5%, 1%, and 2%). It is shown that, in addition to the crystal quality concern of InGaAsN QWs during crystal growth, the nitrogen composition of $GaAs_{1-x}N_x$ strain compensated barrier also plays an important role in the confinement of carriers. Next, to better confine carriers in the InGaAsN/GaAsN active region, a high bandgap 15-nm-thick $GaAs_{0.9}P_{0.1}$ is proposed to be inserted into the active region before the growth of p-type layers of the conventional structure. The demonstrated laser characteristics and a theoretical analysis are given in the mean time. Specifically, the phenomenon of electronic leakage current is investigated.

6-1 Method and numerical parameters

Based on the $k \cdot p$ theory with valence band mixing effect, a 6×6 Hamiltonian of the Luttinger-Kohn type matrix and an envelope function approximation were used to solve the InGaAsN/GaAsN QW subband structures. Detail illustrations could be found in Chapter 2. For this specific simulation, the ratio of conduction band to valence band

offset in InGaAsN/GaAsN band alignment was estimated to 0.7/0.3 [23]. The bandgap energy of InGaAsN material at room temperature was governed by the following bilinear terms with two bowing terms:

$$E_g(term1) = x \cdot y \cdot E_{g,GaAs} + x \cdot (1-y) \cdot E_{g,GaN} \tag{6.1}$$

$$E_g(term2) = (1-x) \cdot y \cdot E_{g,InAs} + (1-x) \cdot (1-y) \cdot E_{g,InN} \tag{6.2}$$

$$E_g(bowing) = x \cdot b\_GaAsN \cdot y \cdot (1-y) + y \cdot b\_InGaAs \cdot x \cdot (1-x) \tag{6.3}$$

where x and y denoted the gallium and arsenide compositions in InGaAsN alloy, and the bandgap energies of GaAs, InAs, GaN and InN were 1.424, 0.355, 3.42 and 0.77 [24] eV. The bowing parameters for GaAsN and InGaAs ternary alloys were -18 [25] and -0.6 eV. The temperature dependent bandgap energy was as follows:

$$E_g(T) = -5.5 \times 10^{-4} \cdot [\frac{T^2}{T+225} - \frac{300^2}{300+225}], \tag{6.4}$$

where $E_g(T)$ was the bandgap energy of InGaAsN alloy at temperature T. Therefore, the temperature dependent bandgap energy of InGaAsN alloy was:

$$E_g(InGaAsN) = E_g(term1) + E_g(term2) + E_g(bowing) + E_g(T) \tag{6.5}$$

The effective mass of electrons used in simulation was as follow:

$$m_e(term1) = x \cdot y \cdot m_{e,GaAs} + x \cdot (1-y) \cdot m_{e,GaN} \tag{6.6}$$

$$m_e(term2) = (1-x) \cdot y \cdot m_{e,InAs} + (1-x) \cdot (1-y) \cdot m_{e,InN} \tag{6.7}$$

$$m_e(InGaAsN) = m_e(term1) + m_e(term2) \tag{6.8}$$

where the effective mass of electrons in GaAs, InAs, GaN and InN were $0.064 \times m_0$, $0.023 \times m_0$, $0.2 \times m_0$ and $0.11 \times m_0$ respectively. The effective masses of light holes (LH) and heavy-holes (HH) were governed by the same form in Eq. (6), and the effective masses of light holes and heavy holes for GaAs were $0.09 \times m_0$ and $0.377 \times m_0$, $0.027 \times m_0$ and $0.263 \times m_0$ for InAs, $0.9767 \times m_0$ and 1.3758 for GaN, and $0.5133 \times m_0$ and $1.5948 \times m_0$ for InN respectively. The Auger coefficients for InGaAsP and InGaAsN were 3.5×10^{-42}

and 1.5×10^{-41} m^2/s. Other material-dependent parameters were taken from the default database values given in the material macro file [26].

6-2 Optical gain properties of InGaAsN QW with GaAsN barriers

Temperature effects on the optical gain properties of $In_{0.4}Ga_{0.6}As_{0.986}N_{0.014}$ and $In_{0.8}Ga_{0.2}As_{0.69}P_{0.31}$ QW materials were studied in the first instance. For the purpose of obtaining an emission wavelength of 1.3 μm, the nitrogen composition in InGaAsN QW was assumed 1.4% with an indium composition in InGaAsN QW of 40%. The calculated material gain of room-temperature $In_{0.4}Ga_{0.6}As_{0.986}N_{0.014}$ and $In_{0.8}Ga_{0.2}As_{0.69}P_{0.31}$ QW materials at an input carrier concentration of 2×10^{18} cm^{-3} was shown Figure 6.1. The barrier materials used under this study for $In_{0.4}Ga_{0.6}As_{0.986}N_{0.014}$ and $In_{0.8}Ga_{0.2}As_{0.69}P_{0.31}$ QWs were $GaAs_{1-x}N_x$ with x=0%, 0.5%, 1%, 2% and $In_{0.9}Ga_{0.1}As_{0.24}P_{0.76}$ [27]. It was found that $In_{0.4}Ga_{0.6}As_{0.986}N_{0.014}/GaAs_{1-x}N_x$ (x=0%, 0.5%, 1%, 2%) materials have higher maximum material gain than that of InGaAsP material. The highest maximum material gain was obtained when x=0%, i.e. GaAs barrier, and the maximum material gain was found to be red shift from 1.3 to 1.34 μm by increasing x value from 0% to 2% in $GaAs_{1-x}N_x$ barrier. In addition, the maximum material gain decreased rapidly with increasing x value in $GaAs_{1-x}N_x$ barrier, which was suggested as a result of the decreased conduction band carrier confinement potential. Nevertheless, the maximum material gain of $In_{0.4}Ga_{0.6}As_{0.986}N_{0.014}/GaAs_{1-x}N_x$ was twice approximately higher than that of $In_{0.8}Ga_{0.2}As_{0.69}P_{0.31}/In_{0.9}Ga_{0.1}As_{0.24}P_{0.76}$ when the input carrier concentration was 2×10^{18} cm^{-3}.

The maximum material gain of using $GaAs_{1-x}N_x$ barriers with x=0%, 0.5%, 1% and 2% as a function of temperature were shown in Figure 6.2. With increasing temperature, an almost linearly drop of maximum material gain was found. A red shift of the maximum material gain with x=0% from 1.3 to 1.35 μm and the decrease of the

maximum material gain value from 2443 to 1575 cm^{-1}, which was due to the wider spreading of the Fermi distribution of carriers and stronger Auger recombination losses, were numerically obtained when the temperature increased from 300 to 370 K. Manifestly, the severe decrease of the maximum material gain value caused by the linear increase of x value indicated that increasing nitrogen composition in GaAsN barrier might procure the poor laser performance as a result of the relatively low material gain.

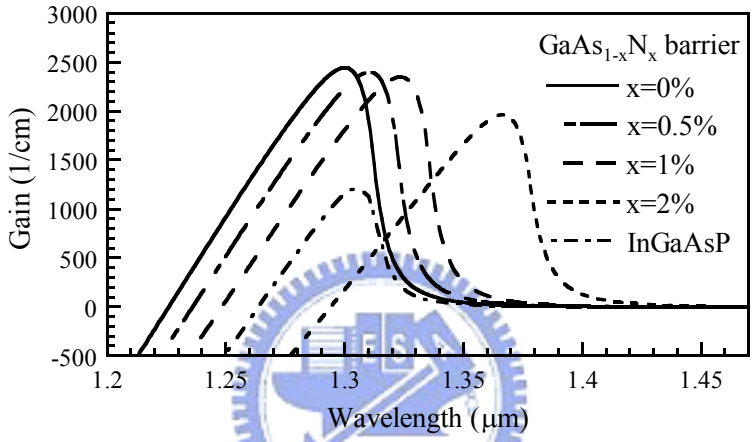

Figure 6.1 Calculated material gain of room-temperature $In_{0.4}Ga_{0.6}As_{0.986}N_{0.014}$ and $In_{0.8}Ga_{0.2}As_{0.69}P_{0.31}$ QWs when the input carrier concentration is 2×10^{18} cm^{-3}.

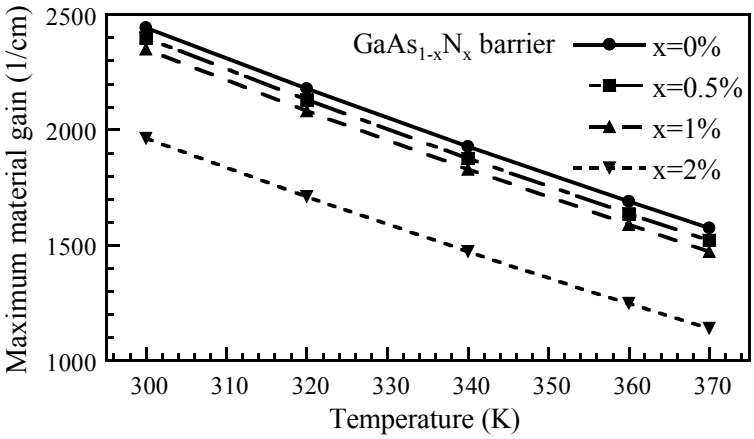

Figure 6.2 Maximum material gain of using $GaAs_{1-x}N_x$ barriers with x=0%, 0.5%, 1% and 2% as a function of temperature.

Figure 6.3 showed the transparency carrier concentration as a function of temperature when using $GaAs_{1-x}N_x$ barriers with x=0%, 0.5%, 1% and 2%. A trend of the increased material gain with increased input carrier concentration was found. As

well, the room-temperature transparency carrier concentrations of $In_{0.4}Ga_{0.6}As_{0.986}N_{0.014}/GaAs_{1-x}N_x$ materials were lower than that of $In_{0.8}Ga_{0.2}As_{0.69}P_{0.31}/In_{0.9}Ga_{0.1}As_{0.24}P_{0.76}$ material, 1.35×10^{18} cm^{-3}. The differential gains of $In_{0.4}Ga_{0.6}As_{0.986}N_{0.014}/GaAs_{1-x}N_x$ materials were also higher than that of $In_{0.8}Ga_{0.2}As_{0.69}P_{0.31}/In_{0.9}Ga_{0.1}As_{0.24}P_{0.76}$ material due to the fact that $In_{0.4}Ga_{0.6}As_{0.986}N_{0.014}/GaAs_{1-x}N_x$ based material had relatively high conduction band offset and more electrons could be confined in the active region effectively. The transparency carrier concentrations at room temperature of using $GaAs_{1-x}N_x$ barriers with x=0% and x=2% are 9.8×10^{17} and 1.06×10^{18} cm^{-3} respectively. For x=0%, the transparency carrier concentration increased almost linearly to 1.25×10^{18} cm^{-3} when the temperature was 370 K. The transparency carrier concentrations of using $GaAs_{1-x}N_x$ barriers with x=0.5% and 1% were slightly higher than that of GaAs barrier in a temperature range of 300-370 K. However, the transparency carrier concentration increased apparently when the x value was 2% and it increased rapidly when the temperature was higher than 350 K.

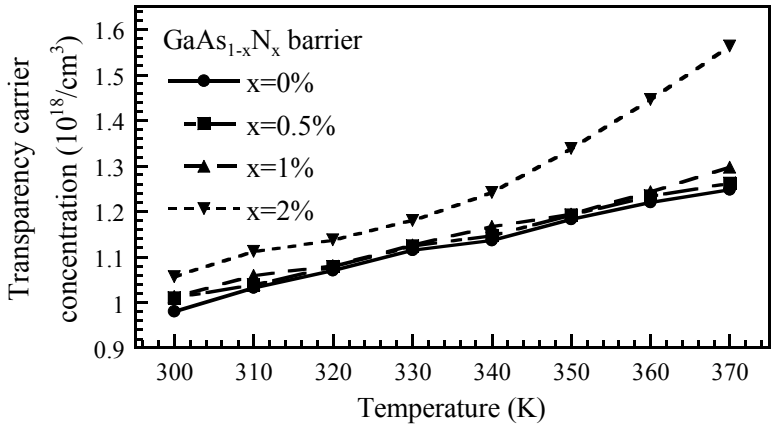

Figure 6.3 Transparency carrier concentration as a function of temperature when using $GaAs_{1-x}N_x$ barriers with x=0%, 0.5%, 1% and 2%.

From the analysis of the optical gain properties of $In_{0.4}Ga_{0.6}As_{0.986}N_{0.014}$ QW sandwiched between $GaAs_{1-x}N_x$ barriers with variant x values, we find that using

$GaAs_{1-x}N_x$ barriers with x value ranging from zero to 1% can have better temperature dependent optical gain properties. When the x value increases to 2%, the maximum material gain and the transparency carrier concentration abate remarkably. It indicates that $In_{0.4}Ga_{0.6}As_{0.986}N_{0.014}$ QW sandwiched between $GaAs_{1-x}N_x$ barriers may have better laser performance, i.e. lower threshold current density and higher slope efficiency, when the x value is zero or less than 2%. Especially, using high potential GaAs barrier provides better electron confinement and results in obtaining highest material gain and lowest transparency carrier concentration. A highest T_0 value may also be obtained as a result of reducing the probability of electronic leakage current if the LD structure is under high temperature operation. Besides, after the consideration of using GaAsN barrier instead of GaAs barrier has several advantages in experiment and longer wavelength can easier be obtained, we find in this study that using $GaAs_{1-x}N_x$ barriers with x=0.5% and 1% can also provide high material gain and low transparency carrier concentration.

6-3 Fabricated device characteristics

After numerically investigated the material gain as a function of nitrogen composition in GaAsN barrier of InGaAsN/GaAaN active region, we further tried to fabricate the 1.3-μm InGaAsN/GaAsN edge emitting lasers in this subsection. Based on the numerical results in prior subsection, a GaAsN material with 0.5% nitrogen composition was chosen as barrier for InGaAsN QW active region because of the comparable material gain properties when compared to GaAs and the help of preventing nitrogen outdiffusion from InGaAsN QW during crystal growth. As schematically plotted in Figure 6.4, the InGaAsN/GaAsN laser structure was grown on the n-type Si-GaAs substrate with (001) orientation. The laser structure under study was grown by low pressure MOCVD with group-V precursors of arsine (AsH_3), phosphine (PH_3), and

U-dimethylhydrazine (U–DMHy) for N-precursor. Trimethyl (TM–) sources of aluminum (Al), gallium (Ga), and indium (In) were used for group-III precursors. The dopant sources were SiH_4 and CBr_4. On top of the GaAs template was a 1.0-μm-thick n-type $Al_{0.6}Ga_{0.4}As$ layer, followed by a 0.15-μm-thick n-type $Al_{0.4}Ga_{0.6}As$ with growth temperature of 770 ºC. Then, the growth temperature was down to 530 ºC for the growth of active region, which contained two $In_{0.41}Ga_{0.59}As_{0.987}N_{0.013}$ wells. The V/III ratio for the growth of active region was kept to 20. The thickness of $In_{0.41}Ga_{0.59}As_{0.987}N_{0.013}$ well and $GaAs_{0.995}N_{0.005}$ barrier, which were determined by X-ray diffraction and growth condition, were 6 nm and 10 nm, respectively. The strains of well and barrier were 2.08% in compressive and 0.2% in tensile, respectively. After the growth of active region, a 10-nm-thick undoped GaAs layer was grown to cap the active region for maintaining better QW quality and a 15-nm-thick undoped high bandgap $GaAs_{0.9}P_{0.1}$ layer was then grown with a purpose of blocking electrons from overflowing to the p-type layers. The guiding region was formed by 0.72-μm-thick updoped GaAs with growth temperature of 530 ºC, followed by a 0.4-μm-thick p-type $Al_{0.4}Ga_{0.6}As$ layer with a doping concentration of 5×10^{18} cm^{-3} and a 1.0-μm-thick p-type $Al_{0.6}Ga_{0.4}As$ layer with a doping concentration of 5×10^{18} cm^{-3}. Finally, a p-type 100-nm-thick GaAs with a doping concentration of 2×10^{19} cm^{-3} was grown to complete the structure. The device was proposed by photolithograthy and reactive ion-etching into narrow stripe ridge waveguide lasers with 4 μm in width and 1000 μm in length. The end facets of the laser chips were uncoated and the laser chip was mounted p-side-down onto copper heat sinks with indium.

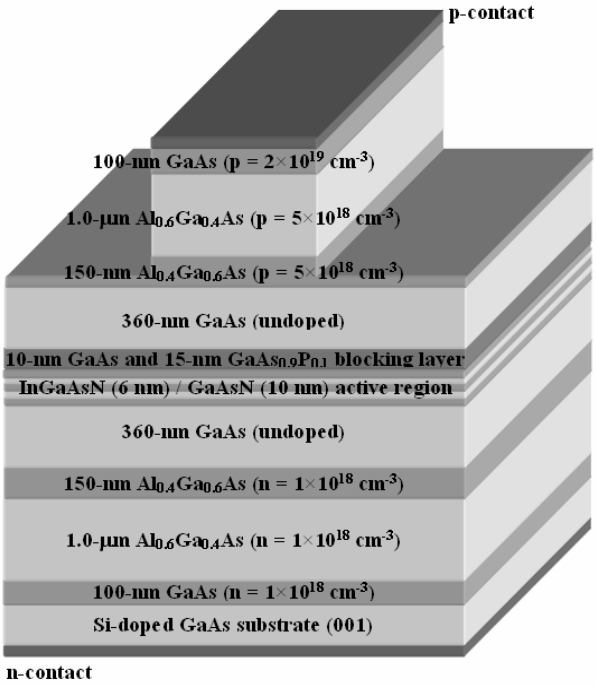

Figure 6.4 A schematic diagram of the double-quantum-well InGaAsN/GaAsN laser structure.

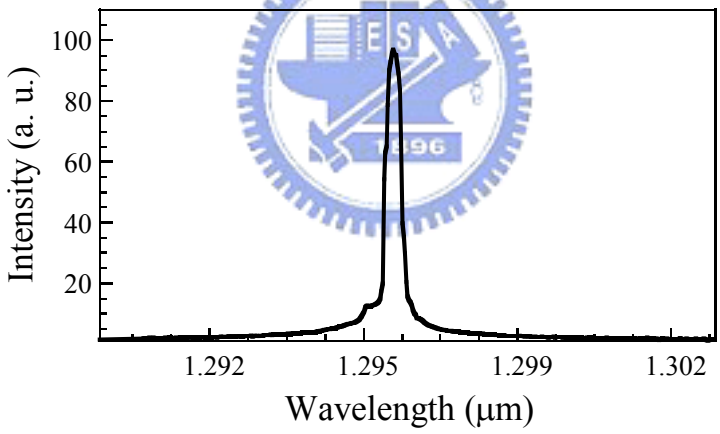

Figure 6.5 Electroluminescence spectrum when the laser device was at an input current of laser threshold.

To better confine carriers in the active region, two structures that were without and with inserting an undoped high-bandgap $GaAs_{0.9}P_{0.1}$ layer into the active region before the growth of p-type layers were prepared. The double-quantum-well structure for type A was the conventional structure that was without capping the high bandgap $GaAs_{0.9}P_{0.1}$ layer on top of the QW active region. Type B was the structure with the high bandgap $GaAs_{0.9}P_{0.1}$ layer. The fabricated laser devices were tested under CW mode operation.

Figure 6.5 showed the electroluminescence spectrum when the laser device was at an input current of laser threshold. A peak emission wavelength of 1.295 μm was obtained for both type A and type B lasers.

The temperature dependent L-I characteristic of type A laser under CW mode operation in a temperature range of 25–105 ºC was shown in Figure 6.6. The threshold current and the threshold current density per QW were 84 mA and 1.05 kA/cm^2 at 25 ºC. Figure 6.7 showed the temperature dependent L–I characteristic of type B laser under CW mode operation in a temperature range of 25–105 ºC. The threshold current was 99 mA and the threshold current density per QW 1.23 kA/cm^2 at 25 ºC. The room temperature slope efficiencies of type A and type B lasers were 0.09 and 0.11 W/A.

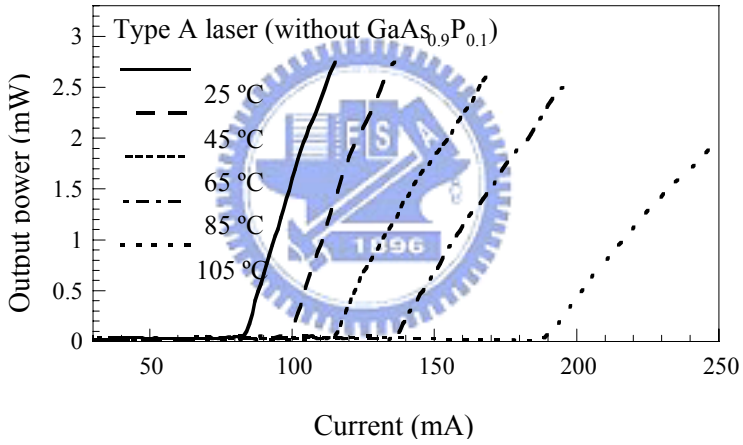

Figure 6.6 Temperature dependent L–I characteristic of type A laser under CW mode operation in a temperature range of 25–105 ºC.

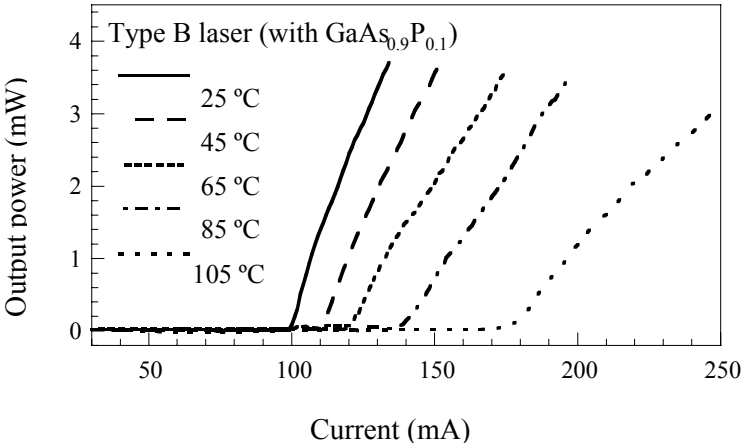

Figure 6.7 Temperature dependent L–I characteristic of type B laser under CW mode operation in a temperature range of 25–105 ºC.

Despite of the high threshold current density at 25 ºC, which was caused by the high strain in the QWs and the nonradiative recombination centers, it was found that the slope efficiency was increased in device B, and the threshold current increased from 99 to 172 mA with a T_0 value of 155 K under CW mode operation when the device temperature was in a range of 25–95 ºC. The T_0 value could achieve to 179 K when the device temperature was in a range of 25–85 ºC. In conventional structure of type A laser, the T_0 value under CW mode operation was 118 K in a temperature range of 25–95 ºC. As the device temperature was higher than 105 ºC, the threshold current of type B laser was found lower than that of type A laser. We suggested that the reduced threshold current was due to the reduction of electronic leakage current and the improvement of hole injection into the active region at higher temperature when the high bandgap $GaAs_{0.9}P_{0.1}$ was inserted into the active region before the growth of p-type layers. The obtained high T_0 value might be partially due to the decreased electronic leakage current and the slight increased threshold current at 25 ºC and monomolecular defect recombination [12].

6-4 Numerical analysis of InGaAsN/GaAsN laser characteristics

Founding on the experimental results that the high temperature performance was improved by inserting a high bandgap $GaAs_{0.9}P_{0.1}$ into the active region before the growth of p-type layers, we further theoretically investigated the effect of the high bandgap $GaAs_{0.9}P_{0.1}$ layer on the laser performance of the 4×1000 μm^2 $In_{0.41}Ga_{0.59}As_{0.987}N_{0.013}/GaAs_{0.995}N_{0.005}$ double-quantum-well laser. The threshold current and slope efficiency of type A and type B lasers obtained experimentally and numerically were depicted in Figure 6.8. For the specific study, the conduction/valence band offset ratio of GaAsP to GaAs was assumed 0.58/0.42 [28].

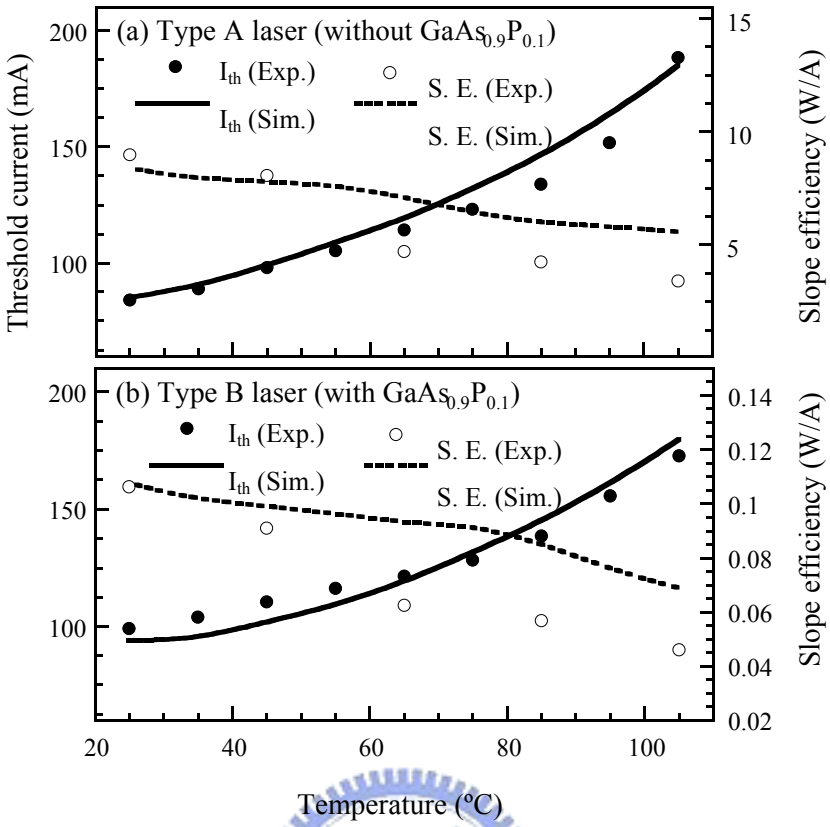

Figure 6.8 Threshold currents and slope efficiencies of type A and type B lasers obtained experimentally and numerically.

It was found that the simulation results could approximately fit in with the experiments. Results of numerical simulation also indicated that the use of $GaAs_{0.9}P_{0.1}$ could beneficially improve the high temperature performance, and an increased T_0 value from 107 to 130 K in a temperature range of 25–95 ºC was anticipated. Even though the T_0 value was not much consistent with the experiments. The discrepancy of the slope efficiencies obtained from the simulations comparing to the experiments was due to the fact that we assumed the laser device was isothermal in simulation and the thermal effects were arduous to be completely considered.

The room-temperature energy band diagrams of type A and type B lasers were shown in Figure 6.9. The diagrams were obtained when the input current was 250 mA and the applied voltage was 1.63 V. The left-hand side of the diagrams was the n side of the laser structure and the dashed lines were quasi-Fermi levels. It was shown that the high-bandgap $GaAs_{0.9}P_{0.1}$ was in the p-side of the active region and acted as an

electronic blocking layer to prevent the electronic current overflow. However, a barrier height in the valence band of inserting the high-bandgap $GaAs_{0.9}P_{0.1}$, shown in figure 6.9(b), was found and this might result in the difficulty of hole injection and the increased threshold current. The increased threshold current caused by inserting $GaAs_{0.9}P_{0.1}$ might also be attributed to the slight decrease of optical confinement factor from 7.4% to 7.2% and the blemished interface between $GaAs_{0.9}P_{0.1}$ and GaAs in crystal growth.

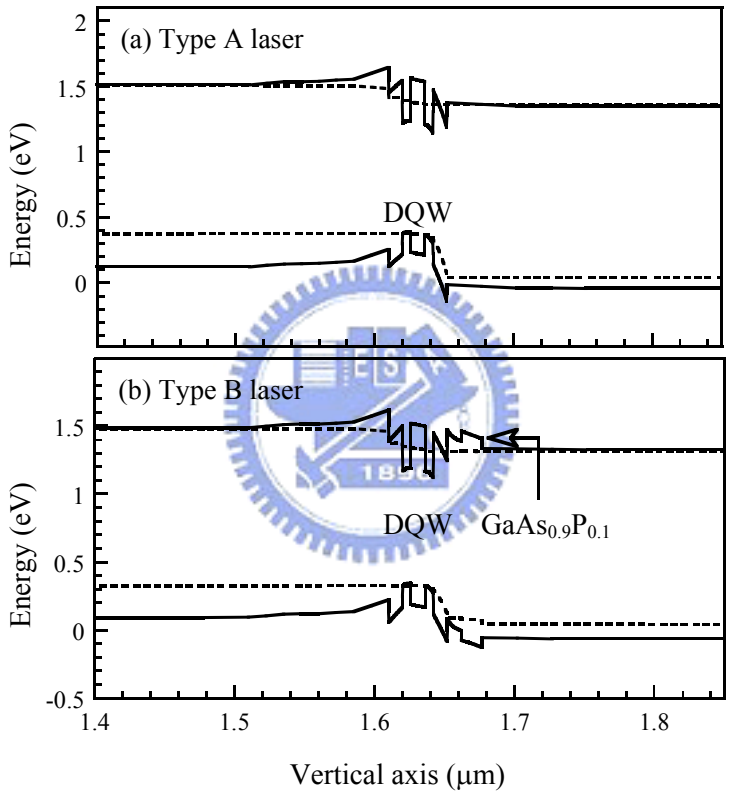

Figure 6.9 Room-temperature energy band diagrams of type A and type B laser structures near the QW active region.

Figure 6.10 illustrated the percentage of electronic leakage current obtained numerically as a function of device temperature for type A and type B lasers. The results were obtained when the devices were at an input current of 250 mA and the percentage of the electronic leakage current was defined as the ratio of the current overflowed to the p-type layer to that injected into the active region. Note that the percentage of electronic leakage current increased with device temperature for both

laser structures. With the help of the increased conduction band offset caused by inserting $GaAs_{0.9}P_{0.1}$, the percentage of electronic leakage current was apparently reduced and in turn decreasing the threshold current at higher temperature. When the device temperature was 95 ºC, there were 8.2% and 4.7% current overflow for type A and type B lasers, respectively, and the percentage of electronic leakage current increased more rapidly for the laser structure without the $GaAs_{0.9}P_{0.1}$.

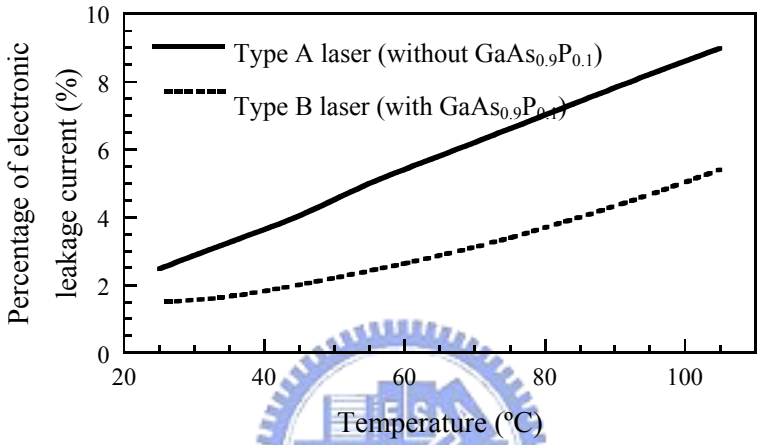

Figure 6.10 Percentage of electronic leakage current obtained numerically as a function of device temperature for type A and type B laser structures.

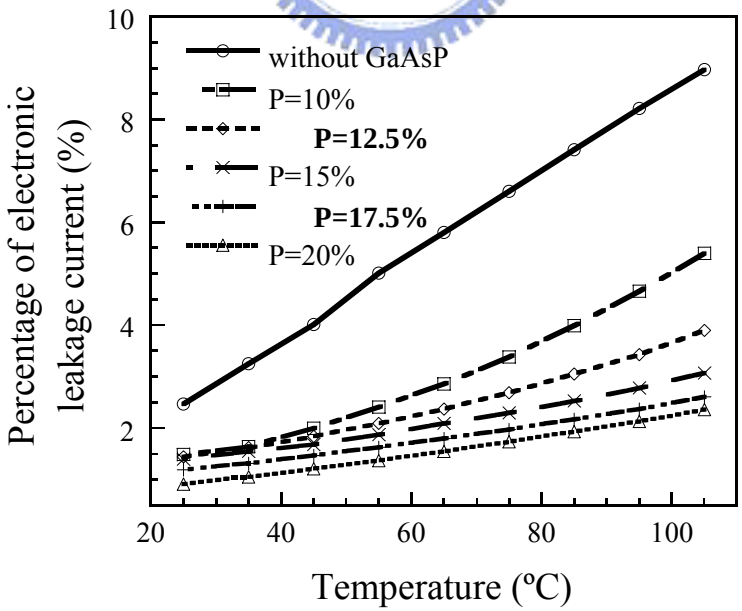

Figure 6.11 Percentage of electronic leakage current of the laser structure without GaAsP and with GaAsP current blocking layer of P=10%–20% as a function of device temperature.

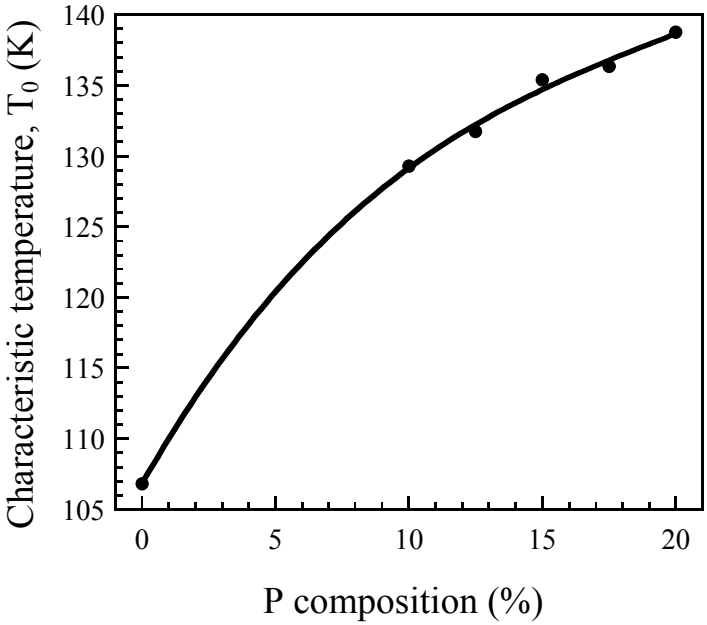

Figure 6.12 Numerical T_0 value of the laser structure without GaAsP and with GaAsP current blocking layer of P=10%–20%. The T_0 value was obtained in a temperature range of 25–95 °C.

To obtain a more favorable T_0 value of the $In_{0.41}Ga_{0.59}As_{0.987}N_{0.013}/GaAs_{0.995}N_{0.005}$ laser, we further theoretically discussed the effect of the high bandgap GaAsP layer with the P composition of 10%–20% on the laser performance. The T_0 value might be improved if the electrons could be efficiently confined in the active region by the higher GaAsP bandgap. The percentage of electronic leakage current of the laser structure without GaAsP and with GaAsP current blocking layer of P=10%–20% as a function of the temperature was indicated in Figure 6.11. More electronic leakage current overflowing to the p-type layers with increased temperature for the laser structures with and without the high bandgap GaAsP was found, and the electronic leakage current was significantly reduced with increased P composition in GaAsP. As illustrated in Figures 6.6 and 6.7, the slope efficiency and the high temperature performance were improved by inserting a high bandgap $GaAs_{0.9}P_{0.1}$ into the active region. It was find theoretically that the improved characteristics might be due to the reduced electronic leakage current. Figure 6.12 depicted the numerical T_0 value of the laser structure without GaAsP and

with GaAsP current blocking layer of P=10%–20% in a temperature range of 25–95 °C. A better T_0 value could be obtained when the P composition in the GaAsP increased. However, we wished to underscore that the better T_0 value was obtained from the decreased threshold current at 95 °C due to the reduced electronic leakage current and a part of slightly increased threshold current at 25 °C.

6-5 Summary

The temperature dependent material gain properties of InGaAsN QW with $GaAs_{1-x}N_x$ barrier of x=0–2% were numerically investigated, while the simulation results suggested that using $GaAs_{1-x}N_x$ strain-compensated barriers with x value less than 0.5% might provide better optical gain properties. To obtain a temperature insensitive output performance of InGaAsN/GaAsN laser, a high-badgap 15-nm-thick $GaAs_{0.9}P_{0.1}$ electronic blocking layer was utilized. Experimental results showed that high temperature performance of the $In_{0.41}Ga_{0.59}As_{0.987}N_{0.013}/GaAs_{0.995}N_{0.005}$ lasers could be improved by inserting a high-badgap 15-nm-thick $GaAs_{0.9}P_{0.1}$ electronic blocking layer before the growth of p-type layers. While the T_0 values of 155 K in a temperature range of 25–95 ºC and 179 K in a temperature range of 25–85 ºC for CW mode operation were obtained. Numerical simulation also suggested that the percentage of electronic leakage current was reduced with the appearance of high-bandgap $GaAs_{0.9}P_{0.1}$ layer. The results obtained numerically also suggested that a more favorable T_0 value could be obtained when the P composition in the GaAsP electronic blocking layer was in a range of 15%–20%.

References

[1] S. F. Yu, in: Analysis and Design of Vertical cavity Surface Emitting Lasers, John Wiley & Sons, Inc, Hoboken, New Jersey, 2003.

[2] S. Sato and S. Satoh, "Metalorganic chemical vapor deposition of GaInNAs lattice matched to GaAs for long-wavelength laser diodes," *J. Cryst. Growth*, vol. 192, pp. 381–385, 1998.

[3] D. Gollub, S. Moses, M. Fischer, and A. Forchel, "GaInNAs for GaAs based lasers for the 1.3 to 1.5 μm range," *J. Cryst. Growth* vol. 251, pp. 353–359, 2003.

[4] S. Mazzucato, N. Balkan, A. Teke, A. Erol, R. J. Potter, M. C. Arikan, X. Marie, C. Fontaine, H. Carrere, E. Bedel, and G. Lacoste, "In-plane photovoltage and photoluminescence study in sequentially grown GaInNAs and GaInAs quantum wells," *J. Appl. Phys*., vol. 93, pp. 2440–2448, 2003.

[5] H. D. Sun, M. D. Dawson, M. Othman, J. C. L. Yong, J. M. Rorison, P. Gilet, L. Grenouillet, and A. Million, "Optical transitions in GaInNAs/GaAs multi-quantum wells with varying N content investigated by photoluminescence excitation spectroscopy," *Appl. Phys. Lett*., vol. 82, pp. 376–378, 2003.

[6] H. Riechert, A. Ramakrishnan, and G. Steinle, "Development of InGaAsN-based 1.3 μm VCSELs," *Semicond. Sci. Technol*., vol. 17, pp. 892–897, 2002.

[7] W. Li, M. Pessa, T. Ahlgren, and J. Decker, " Origin of improved luminescence efficiency after annealing of Ga(In)NAs materials grown by molecular-beam epitaxy," *Appl. Phys. Lett*., vol. 79, pp. 1094–1096, 2001.

[8] N. Tansu, Luke J. Mawst, "Temperature sensitivity of 1300-nm InGaAsN quantum-well lasers," *IEEE Photonics Technol. Lett*., vol. 14, pp. 1052–1054, 2002.

[9] J. C. L. Yong, J. M. Rorison, M. Othman, H. D. Sun, M. D. Dawson, and K. A. Willaims, "Simulation of gain and modulation bandwidths of 1300 nm RWG InGaAsN lasers," *IEE Proc.-Optoelectron*., vol. 150, pp. 80–82, 2003.

[10] J. C. L. Yong, Judy. M. Rorison, and Ian H. White, "1.3-μm quantum-well InGaAsP, AlGaInAs, and InGaAsN laser material gain: A theoretical study," *IEEE J. Quantum Electron*., vol. 38, pp. 1553–1564, 2002.

[11] D. Alexandropoulos and M. J. Adams, "Assessment of GaInNAs as a potential laser material," *IEE Proc.-Optoelectron*., vol. 150, pp. 40–44, 2003.

[12] W. J. Fan, S. T. Ng, S. F. Yoon, M. F. Li, and T. C. Chong, "Effect of tensile strain in barrier on optical gain spectra of GaInNAs/GaAsN quantum wells," *J. Appl. Phys*., vol. 93, pp. 5836–5838, 2003.

[13] S. Sato, "Low threshold and high characteristic temperature 1.3 μm range GaInNAs lasers grown by metalorganic chemical vapor deposition," *Jpn. J. Appl.*

Phys., vol. 39, pp. 3403–3405, 2000.

[14] T. Kitatani, K. Nakahara, M. Kondow, K. Uomi, and T. Tanaka, "A 1.3-μm GaInNAs/GaAs single-quantum-well laser diode with a high characteristic temperature over 200 K," *Jpn. J. Appl. Phys*., vol. 39, pp. L86–L87, 2000.

[15] N. Tansu and L. J. Mawst, "Low-threshold strain-compensated InGaAs(N) (λ=1.19–1.31 μm) quantum-well lasers," *IEEE Photonics Technol. Lett.*, vol. 14, pp. 444–446, 2002.

[16] N. Tansu, N. J. Kirsch, and L. J. Mawst, "Low-threshold-current-density 1300-nm dilute nitride quantum well lasers," *Appl. Phys. Lett*. vol. 81, pp. 2523–2525, 2002.

[17] C. S. Peng, T. Jouhti, P. Laukkanen, E.-M. Pavelescu, J. Konttinen, W. Li, and M. Pessa, " 1.32-μm GaInNAs-GaAs laser with a low threshold current density," *IEEE Photonics Technol. Lett.*, vol. 14, pp. 275–277, 2002.

[18] D. A. Livshits, A. Yu. Egorov, and H. Riechert, "8 W continuous wave operation of InGaAsN laser at 1.32 μm," *Electron. Lett*., vol. 36, pp. 1381–1382, 2000.

[19] J. Wei, F. Xia, C. Li, and S. R. Forrest, "High T_0 long-wavelength InGaAsN quantum well lasers grown by GSMBE using a solid arsenide source," *IEEE Photonics Technol. Lett*., vol. 14, pp. 597–599, 2002.

[20] R. Fehse, S. Tomic, A. R. Adams, S. J. Sweeney, E. P. O'Reilly, A. Andreev, and H. Riechert, "A qualitative study of radiative, auger, and defect related recombination processes in 1.3-μm GaInNAs-based quantum-well lasers," *IEEE J. Sel. Top. Quantum Electron*., vol. 8, pp. 801–810, 2002.

[21] N. Tansu and L. J. Mawst, "The role of hole leakage in 1300-nm InGaAsN quantum-well lasers," *Appl. Phys. Lett.*, vol. 82, pp. 1500–1502, 2003.

[22] W. Li, T. Jouhti, S. Peng. Chang, J. Konttinen, P. Laukkanen, E.-M. Pavelescu, M. Dumitrescu, and M. Pessa, "Low-threshold-current 1.32-μm GaInNAs/GaAs single-quantum-well lasers grown by molecular-beam epitaxy," *Appl. Phys. Lett*., vol. 79, pp. 3386–3388, 2001.

[23] L. Bellaiche, S.-H. Wei, and A. Zunger, "Localization and percolation in semiconductor alloys: GaAsN vs GaAsP," *Phys. Rev. B*, vol. 54, pp. 17568–17576, 1996.

[24] J. Wu, W. Walukiewicz, K. M. Yu, J. W. Ager III, E. E. Haller, H. Lu, and W. J. Schaff, "Small bandgap bowing in $In_{1-x}Ga_xN$ alloys," *Appl. Phys. Lett*., vol. 80, pp. 4741–4743, 2002.

[25] M. Kondow, K. Uomi, A. Niwa, T. Kitatani, S. Watahiki, and Y. Tazawa, "GaInNAs: A novel material for long-wavelength-range laser diodes with excellent high-temperature performance," *Jpn. J. Appl. Phys*., vol. 35, pp. 1273–1275, 1996.

[26] LASTIP User's Manual Version 2003.12 Crosslight Inc Software, Canada. Available online at web page http://www.crosslight.ca.

[27] A. F. Phillips, S. J. Sweeney, A. R. Adams, and P. J. A. Thijs, “The temperature dependence of 1.3- and 1.5-μm compressively strained InGaAs(P) MQW semiconductor lasers,” *IEEE J. Sel. Top. Quantum Electron*., vol. 5, pp.401–412, 1999.

[28] H. Q. Hou, C. W. Tu, W. Shan, S. J. Hwang, J. J. Song, and S. N. G. Chu, “Characterization of GaAs/GaAsP strained multiple quantum well grown by gas-source molecular beam epitaxy,” *J. Vac. Sci. Technol. B*, vol. 11, pp. 854–856, 1993.

Chapter 7 Conclusion and future work

In this dissertation, the improvement in operation performance of III-V optoelectronic semiconductor light emitting devices, including ultraviolet AlGaInN/GaN LEDs, 650-nm red resonant-cavity LEDs, 850-nm VCSELs, and 1.3-μm EELs were experimentally demonstrated and theoretically analyzed. Specifically, by optimizing the configuration of quantum well active regions in the four light-emitting devices, the respectively fabricated operation performances are expectedly improved. The results obtained numerically show that the improvement is mainly attributed to the better confinement of carriers in the quantum well active region. It is hoped that the works in this dissertation can stimulate the researchers having more inspiration and a better understanding in designing the structure of light-emitting devices.

Future work

(a) GaN-based RCLEDs and VCSELs

Based on the well trainings in the MOCVD growth techniques, the semiconductor physics background, and the capability in modeling and designing the semiconductor device structures during my past engaging Ph.D. degree period, I will turn my research field into the design and fabrication of GaN-based RCLEDs and VCSELs. It is quite important to develop high-performance green–blue RCLEDs and VCSELs. For green RCLED, it can be used in the POFs, in which a minimum attenuation loss is observed at 510 nm, and the device is much temperature insensitive. For blue RCLED and VCSEL, the high-direction and elliptic beam shape properties help the device to be used in the applications of optical fiber communication and data storage systems. However, recent development in the green–blue RCLEDs and VCSELs shows that there still has room to improve the device performance. The structure design and growth condition

optimization seem the most important.

(b) Compound solar cells

III-V compounds are the basic materials for modern optoelectronic devices. Apart from this, they often show superior properties compared to Si in the field of microelectronics, for example high-speed transistors. In the field of solar cells, GaAs has higher theoretical and practical efficiencies than Si. For multi-junction solar cells including InGaP, (In)GaAs, and Ge, they are known as super-high efficiency and are now of great significance for space applications and light concentrations. A concentrator photovoltaic (PV) system using high-efficiency solar cells is one of the important issues for the development of an advanced PV system. The production cost of multi-junction solar cells composed of III–V materials is higher than that of Si solar cells. However, the necessary cell size decreases with increasing concentration ratio, and the total cost of concentrator systems decreases.

To date, I have made the conversion efficiencies of single p-n junction GaAs and InGaP solar cells up to 23% and 16.2%, respectively. The two-junction InGaP/GaAs tandem solar cell will have higher conversion efficiency if epitaxially combined by a tunnel junction. So, it is quite urgent to optimize the tunnel junction, while the constitution of tunnel junction can be p^+-GaAs/n^+-GaAs and p^+-$Al_{0.4}Ga_{0.6}As$/n^+-$In_{0.5}Ga_{0.5}P$. Hopefully, I can improve the efficiency of the two-junction InGaP/GaAs up to 27%. In the mean time, the single-junction GaAs and InGaP shall be optimized to have higher short-circuit current density (J_{sc}), open-circuit voltage (V_{oc}), and fill-factor (FF) value.

List of Publications (Yi-An Chang)

SCI, EI 論文

1. **Yi-An Chang**, Jun-Rong Chen, Tsung-Shine Ko, Hao-Chung Kuo, Yen-Kuang Kuo, Tien-Chang Lu, Jui-Yen Tsai, Li-Wen Laih, and Shing-Chung Wang, "Fabrication and characterization of temperature insensitive 660-nm resonant-cavity LEDs," submitted to ***IEEE Journal of Quantum Electronics***, 2007.

2. **Yi-An Chang**, Jui-Yen Tsai, Hao-Chung Kuo, Tien-Chang Lu, Li-Wen Laih, and Shing-Chung Wang, "InGaP solar cells with variant p-emitter configurations," submitted to ***Japanese Journal of Applied Physics***, 2007.

3. **Yi-An Chang**, Hao-Chung Kuo, Ya-Hsien Chang, and Shing-Chung Wang, "Improved photoluminescence of 1.26-μm InGaAs/GaAs quantum well assisted by Sb and indium graded intermediate layers," ***Applied Physics Letter***, vol. 87, pp. 061908, 2005.

4. **Yi-An Chang**, Chun-Lung Yu, I-Tsung Wu, Hao-Chung Kuo, Fang-I Lai, Li-Wen Laih, Li-Horng Laih, Tin-Chang Lu, and Shing-Chung Wang, "Design and fabrication of temperature insensitive 650-nm resonant-cavity light-emitting diodes," ***IEEE Photonics Technology Letter***, vol. 18, no. 16, pp. 1690–1692, 2006.

5. **Yi-An Chang**, Tsung-Hsine Ko, Fang-I Lai, Jun-Rong Chen, Chun-Lung Yu, I-Tsung Wu, Hao-Chung Kuo, Yen-Kuang Kuo, Li-Wen Laih, Li-Horng Laih, Tin-Chang Lu, and Shing-Chung Wang, "Carrier blocking effect on 850-nm InAlGaAs/AlGaAs vertical-cavity surface-emitting lasers," ***Semiconductor Science & Technology***, vol. 21, pp. 1488–1494, 2006.

6. **Yi-An Chang**, Sheng-Horng Yen, Te-Chung Wang, Hao-Chung Kuo, Yen-Kuang Kuo, and Shing-Chung Wang, "Experimental and theoretical analysis on ultraviolet 370-nm AlGaInN light-emitting diode," ***Semiconductor Science & Technology***, vol. 21, pp. 598–603, 2006.

7. **Yi-An Chang**, Jun-Rong Chen, Hao-Chung Kuo, Yen-Kuang Kuo, and Shing-Chung Wang, "Theoretical and experimental analysis on InAlGaAs/AlGaAs active region of 850-nm vertical-cavity surface-emitting lasers," ***IEEE/OSA Journal of Lightwave Technology***, vol. 24, no.1, pp. 536–543, 2006.

8. **Yi-An Chang**, Fang-I Lai, Hsin-Chun Yu, Hao-Chung Kuo, Li-Wen Laih, Chun-Lung Yu, and Shing-Chung Wang, "High-temperature stability 850-nm $In_{0.15}Al_{0.08}Ga_{0.77}As/Al_{0.3}Ga_{0.7}As$ VCSEL with single $Al_{0.75}Ga_{0.25}As$ current blocking layer," ***Japanese Journal of Applied Physics***, vol. 44, no. 28, pp. L901–L902, 2005.

9. **Yi-An Chang**, Chuan-Yu Luo, Hao-Chung Kuo, Yen-Kuang Kuo, Chia-Feng Lin, and Shing-Chung Wang, "Simulation of InGaN quantum well laser performance using quaternary InAlGaN alloy as electronic blocking layer," ***Japanese Journal of Applied Physics***, vol. 44, no. 11, pp. 7916–7918, 2005.

10. **Yi-An Chang**, Jung-Tang Chu, C. -T. Ko, Hao-Chung Kuo, and Shing-Chung Wang, "MOCVD growth of highly strained 1.3-μm InGaAs:Sb/GaAs Vertical Cavity Surface Emitting Laser," ***Journal of Crystal Growth***, vol. 287, pp. 550–553, 2005.

11. **Yi-An Chang**, Hao-Chung Kuo, Chun-Yi Lu, and Shing-Chung Wang, "Improving high

temperature performance in continuous-wave mode InGaAsN/GaAsN ridge waveguide lasers," ***Semiconductor Science & Technology***, vol. 20, pp. 601–605, 2005.

12. **Yi-An Chang**, Hao-Chung Kuo, Ya-Hsien Chang, and Shing-Chung Wang, "Simulation of 1300-nm $In_{0.4}Ga_{0.6}As_{0.986}N_{0.014}/GaAs_{1-x}N_x$ quantum-well lasers with various $GaAs_{1-x}N_x$ strain compensated barriers," ***Optics Communication***, vol. 241, pp. 195, 2004.

13. Tsung-Shine Ko, Chia-Pu Chu, Jun-Rong Chen, **Yi-An Chang**, Tien-Chang Lu, Hao-Chung Kuo, and Shing-Chung Wang, "Synthesis of In2O3 nanocrystal chains and annealing effect on their optical properties," ***J. Vac. Sci. Technol. A***, vol. 25, no. 4, pp. 1038–1041, 2007.

14. Yen-Kuang Kuo and **Yi-An Chang**, "Effect of electronic current overflow and inhomogeneous carrier distribution on InGaN qauntum-well laser performance," ***IEEE Journal of Quantum Electronics***, vol. 40, pp. 437, 2004.

15. Hao-Chung Kuo, Hsin-Horng Yao, Ya-Hsien Chang, **Yi-An Chang**, Ming-Ying Tsai, J. Hsieh, Edward-Yi Chang, and Shing-Chung Wang, "MOCVD growth of highly strained InGaAs:Sb-GaAs-GaAsP vertical cavity surface-emitting lasers with 1.27-μm emission," ***Journal of Crystal Growth***, vol. 272, pp. 538, 2004.

16. Hao-Chung Kuo, Ya-Hsien Chang, **Yi-An Chang**, Fang-I Laih, Jung-Tang Chu, Ming-Ying Tsai, and Shing-Chung Wang, "Single-mode 1.27-μm InGaAs:Sb-GaAs-GaAsP quantum well vertical cavity surface emitting lasers," ***IEEE Journal Selected Topics in Quantum Electronics***, vol. 11, pp. 121, 2005.

17. Ya-Hsien Chang, Hao-Chung Kuo, Fan-I Lai, **Yi-An Chang**, Chun-Yi Lu, Li-Hong Laih, and Shing-Chung Wang, "Fabrication and characteristics of high-speed oxide-confined VCSELs using InGaAsP-InGaP strain-compensated MWQs," ***IEEE Journal Lightwave Technology***, vol. 22, pp. 2828, 2004.

18. Yen-Kuang Kuo and **Yi-An Chang**, "Numerical study of passive Q switching of a Tm:YAG laser with a Ho:YLF solid-state saturable absorber," ***Applied Optics***, vol. 42, pp. 1685, 2003.

19. Ya-Hsien Chang, Hao-Chung Kuo, **Yi-An Chang**, Jung-Tang Chu, Ming-Ying Tsai, and Shing-Chung Wang, "10 Gbps InGaAs:Sb-GaAs-GaAsP quantum well vertical cavity surface emitting lasers with 1.27 μm emission wavelengths," ***Japanese Journal of Applied Physics***, vol. 44, pp. 2556–2559, 2005.

20. Yen-Kuang Kuo, Hsiu-Fen Chen, and **Yi-An Chang**, "Simulation of Ho:CaF_2 Q-switched Tm:$Y_3Al_5O_{12}$ Laser," ***Japanese Journal of Applied Physics***, vol. 43, pp. 3448, 2004.

21. **Yi-An Chang**, Hao-Chung Kuo, Ya-Hsien Chang, Shing-Chung Wang, and Li-Hong Laih, "Simulation and analysis of 1300-nm $In_{0.4}Ga_{0.6}As_{0.986}N_{0.014}/GaAs_{1-x}N_x$ quantum-well lasers with various $GaAs_{1-x}N_x$ strain compensated barriers," ***SPIE-Proceedings***, vol. 5628, pp. 40-48, 2005. (Invited)

22. **Yi-An Chang** and Yen-Kuang Kuo, "Optical performance of Ho:YLF Q-switched Tm:YAG laser system," ***SPIE-Proceedings***, vol. 4914, pp. 122, 2002. (High-Power Lasers and Applications), October 2002.

23. Sheng-Horng Yen, Bo-Jean Chen, Mei-Ling Chen, Yen-Kuang Kuo, **Yi-An Chang**, and Hao-Chung Kuo, "Fabrication and simulation of ultraviolet AlGaInN light-emitting diodes", ***SPIE-Proceedings*** (Light-Emitting Diodes: Research, Manufacturing, and Applications X), paper 6134-21, 2006.

Conference，中文期刊

1. **Y. A. Chang**, C. C. Kao, T. K. Kao, W. K. Tsai, C. L. Yu, Y. T. Wu, F. I. Lai, L. W. Laih, L. W. Laih, H. C. Kuo, T. C. Lu, S. C. Wang, "MOCVD growth and characterization of temperature insensitive 650-nm resonant-cavity light-emitting diodes," **13th MOVPE conference**, no. #A125, 2006.

2. **Y. A. Chang**, C. C. Kao, H. C. Kuo, J. T. Chu, J. R. Chen, S. H. Yen, C. L. Yu, I. T. Wu, F. I. Lai, T. C. Lu, Y. K. Kuo, and S. C. Wang, "Growth and fabrication of p-side-down InGaAs:Sb/GaAs vertical-cavity surface-emitting lasers," **13th MOVPE conference**, no. #A126, 2006.

3. **Yi-An Chang**, Sheng-Horng Yen, Tsung-Hsine Ko, Te-Chung Wang, Chun-Yi Lu, Hao-Chung Kuo, Yen-Kuang Kuo, Tien-Chang Lu, Shing-Chung Wang, "Experimental and Theoretical Analysis on Ultraviolet 370-nm AlGaInN Light-Emitting Diodes," **CLEO/QELS 2006**, JWB77, no. 1811.

4. Sheng-Horng Yen, Bo-Jean Chen, Mei-Ling Chen, Yen-Kuang Kuo, **Yi-An Chang**, and Hao-Chung Kuo, "Fabrication and simulation of ultraviolet AlGaInN light-emitting diodes," **Photonics West**, 2006.

5. **Y. A. Chang**, J. T. Chu, C. T. Ko, H. C. Kuo, C. F. lin, S. C. Wang, "MOCVD growth og highly strained InGaAs:Sb/GaAs quantum wells vertical-cavity surface-emitting lasers toward 1.3 μm emission," **12th MOCVD conference**, #112, 2005.

6. **張詒安**、郭艷光、郭浩中、王興宗, "紫藍光氮化銦鎵量子井雷射之模擬與分析," *光學工程季刊,* vol. 85, pp. 47, 2004. **(註：本論文榮獲 2003 年「中華民國光學工程學會碩士班學生論文獎」)**

7. **張詒安**、羅傳煜、郭浩中、王興宗, "長波長 1.3-μm InGaAsN/GaAsN 量子井雷射之結構設計與分析," 2004 年台灣光電科技研討會, paper A-SU-I 5-5.

8. 羅傳煜、**張詒安**、郭浩中、郭艷光、王興宗, "InGaN 量子井雷射使用四元材料 AlInGaN 為阻擋層的特性分析," 2004 年台灣光電科技研討會, paper A-SU-I 9-2.

9. Yen-Kuang Kuo, Kuo-Kai Horng, Hsu-Ching Huang, Ya-Lien Huang, Jih-Yuan Chang, Yuni Chang, Wen-Wei Lin, **Yi-An Chang**, and Chih-Kang Chang, 2000, "Numerical study on III-N and III-P semiconductor materials with LASTIP, PICS3D, and CASTEP," in the 2nd International Photonics Conference (IPC2000, National Chiao Tung University, Hsinchu, Taiwan), paper W-S1-A003, pp. 17-19, Proc. IPC 2000.

10. **Yi-An Chang**, Jih-Yuan Chang, Yen-Kuang Kuo, Jiann Lin, and Chung-I Chiang, 2001, "Optical properties of InGaN multi-quantum well structures - experimental measurement and numerical simulation," paper PE14, 2001 年中華民國物理年會.

11. **張詒安**、黃雅蓮、郭艷光, 2001, "黃綠光磷化鋁鎵銦面射型半導體雷射之模擬分析," paper FA2-8, pp. 398-400, 2001 年台灣光電科技研討會.

12. 張志康、**張詒安**、郭艷光, 2001, "光纖通訊用 1.3-μm 面射型半導體雷射之模擬分析," paper P29, pp. 959-961, 2001 年台灣光電科技研討會.

13. **Yi-An Chang** and Yen-Kuang Kuo, 2002, "Design and Characterization of a 1.55-μm $In_{0.76}Ga_{0.24}As_{0.82}P_{0.18}/In_{0.48}Ga_{0.52}As_{0.82}P_{0.18}$ Vertical-Cavity Surface-Emitting Laser," paper E-069, 2002 年中華民國物理年會.

14. **張詒安**、陳秀芬、謝尚衛、吳佩璇、蔡孟倫、張誌原、郭艷光、劉柏挺, "415 nm 紫光氮化銦鎵量子井雷射電子溢流特性之探討," paper TAl-3, pp. 7-9, 2002 年台灣光電科技研討會.

15. **張詒安**、吳佩璇、吳育驊、屠嫚琳、郭艷光、劉柏挺, 2002, "使用 Dy:CaF_2 被動 Q 開關於紅寶石雷射之模擬分析," paper TG2-6, pp. 337-339, 2002 年台灣光電科技研討會.

16. 楊勝州、**張詒安**、顏勝宏、黃詩瑋、蔡孟倫、劉冠良、陳俊榮、林漢威、何依萍、郭艷光, 2002, "紫光氮化銦鎵面射型半導體雷射之設計與分析," paper PA-33, pp. 97-99, 2002 年台灣光電科技研討會.

17. **張詒安**、張志康、郭艷光, 2002, "使用可飽和吸收體 Ho:YVO_4 於 2-μm Tm:$Y_3Al_5O_{12}$ 雷射系統的性能分析," paper TG2-8, pp. 343-345, 2002 年台灣光電科技研討會.

18. Pei-Hsuan Wu、**Yi-An Chang**、Yen-Kuang Kuo, 2003, "Optical performance of Cr:YSO and Dy:CaF_2 Q-switched ruby laser systems," paper PE63, 2003 年中華民國物理年會.

19. Hsiu-Fen Chen、Shang-Wei Hsieh、**Yi-An Chang**、Yen-Kuang Kuo、Man-Fang Huang、Hwei-Heng Wang、Pin-Hwei Liu, "Experimental and numerical investigation of 590-nm AlGaInP light emitting diodes and vertical-cavity surface-emitting lasers," 2003 年中華民國物理年會.

20. Meng-Lun Tsai、Sheng-Joue Young、**Yi-An Chang**、Sheng-Horng Yen、Shih-Wei Huang、Yen-Kuang Kuo, "Numerical study of violet InGaN vertical-cavity surface-emitting laser," paper PD36, 2003 年中華民國物理年會.

21. Shang-Wei Hsieh、Hsiu-Fen Chen、**Yi-An Chang**、Yen-Kuang Kuo, "Numerical study of Cr:LiSAF passive Q-switching with a Cr:YSO solid-state saturable absorber," paper PE62, 2003 年中華民國物理年會.